

Report N00014-86-K-509

TAILORED MICROSTRUCTURES FOR BROADBAND
OR SELECTIVE DETECTION OF RADIATION FROM
THE VISIBLE TO THE INFRARED

Clayton W. Bates, Jr.
Department of Materials Science and Engineering
Stanford University
Stanford, CA 94305

25 August 1994

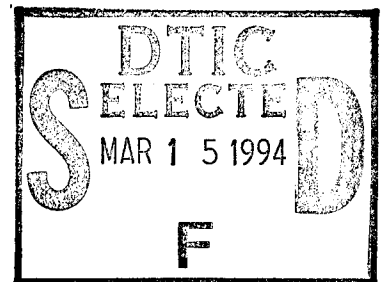
Final Technical Report for Period

1 January 1986 - 31 December 1992

Prepared for

Department of the Navy
Office of Naval Research Detachment, Boston
495 Summer Street
Boston, MA 02210
Attention: Dr. Fred Quelle

This document has been approved
for public release and sale; its
distribution is unlimited.



19950314 031

19950216 0069

Publications Produced During Support Period

1. Q. Y. Chen and C. W. Bates, Jr., *Mats. Res. Soc. Symp.* **90**, 171 (1987).
2. B. Haba and C. W. Bates, Jr., *Thin Solid Films* **158**, 133 (1988).
3. Q. Y. Chen and C. W. Bates, Jr., *Phys. Rev.* **B37** (16), 9148 (1988).
4. C. W. Bates, Jr., Q. Y. Chen and N. V. Alexander, *Adv. EEP* **74**, 339 (1988).
5. C. W. Bates, Jr., *Technet '88 Symp. Proc.* **1** (1988).
6. B. Haba, C. W. Bates, Jr., B. Brown, Z. Ndlela and G. Smestad, *Thin Solid Films* **159**, L53 (1988).
7. B. Brown, B. Haba and C. W. Bates, Jr., *J. Electrochem. Soc.* **135**(6), 1559 (1988).
8. Z. Ndlela and C. W. Bates, Jr., *Rev. Sci. Instrum.* **60**(11), 3482 (1989).
9. B. Haba, C. W. Bates, Jr., B. Brown and Z. Ndlela, *Solar Cells* **28**, 177 (1990).
10. B. Brown and C. W. Bates, Jr., *Thin Solid Films* **188**, 301 (1990).
11. B. Brown and C. W. Bates, Jr., *J. Appl. Phys.* **68**(5), 2517 (1990).
12. Z. Ndlela and C. W. Bates, Jr., *Mats. Lett.* **10**, 465 (1991).
13. W. A. Strifler and C. W. Bates, Jr., *J. Mater. Res.* **6**(3), 548 (1991).
14. C. W. Bates, Jr., *IOP Conf. Series* **121**, 319 (1992).
15. C. W. Bates, Jr., *IOP Conf. Series* **121**, 363 (1992).
16. W. A. Strifler, *J. Appl. Phys.* **71**(9), 4358 (1992).

Accession For	
NTIS CR-Ref	<input checked="" type="checkbox"/>
DTIC TAB	<input type="checkbox"/>
Unannounced	<input type="checkbox"/>
Justification	
By	
Distribution /	
Availability Codes	
Dist	Avail and/or Special
A-1	

SUMMARY OF COMPLETED PROJECT

The primary objectives of this project were to prepare and measure the optical and electrical transport properties of metal-semiconductor inhomogeneous composite systems for possible optoelectronic applications. The systems investigated were Ag-O-Cs, Ag-Si and Ag, Au-CuInSe₂, where the metal particles were dispersed throughout the semiconductor matrices in sizes ranging from about 5nm to 100nm. The approach was to relate the microstructure, i.e., the metal size distribution, volume fraction and optical properties of metal and matrix to the optical and electrical transport properties of the composite system. For this purpose a complete, self-consistent electromagnetic theory was developed which accounted very accurately for experimentally measured composite optical properties. It was found that the optical absorption of these systems could be varied in a known fashion suggested by the developed theory and that transport properties such as the mobility of carriers was not compromised by the large volume fraction of metal in these systems. The high absorption at wavelengths determined by their microstructures makes them attractive as ultrathin elements in a variety of optoelectronic schemes.

Chapter One	Introduction-----	1
Chapter Two	Interactions of Electromagnetic Radiations with Small Metal Particles – The Optical Constants of Composites –	
	I. Introduction to Small Metal Particles-----	10
	II. Electromagnetic Interactions with Small Particles-----	13
	II.1 Forward Scattering and Optical Theorem-----	14
	II.2 Quasi-Static Effective Medium Approximations-----	17
	II.3 Dynamic Effective Medium Approximations-----	22
	III. Particle Aggregations and Electromagnetic Properties-----	25
Chapter Three	Photoemission from Small Particles	
	I. Introduction-----	28
	II. Theoretical Fundation-----	29
	III. Numerical Results and Discussions-----	34
Chapter Four	Relationships between Microstructures and Optoelectronic Properties of S-1 Photoemitting Surfaces	
	I. Introduction-----	38
	II. Multiple-Step Model of Photoemission-----	40
	III. Optical Properties of the S-1 photocathode-----	45
	IV. Numerical Results and the Photoelectric Quantum Yields-----	54
	V. Conclusions and Material Designing Rules-----	58
Chapter Five	Silver Particles in Semiconductors	
	I. Introduction-----	83
	II. Experimental Set-Up of Material Preparations	
	II.1 Sputtering Apparatus-----	86
	II.2 Electron Beam Deposition-----	90
	II.3 Spray Pyrolysis of CuInSe ₂ -----	90
	III. Experimental Results on Microstructure Engineering	
	III.1 Co-deposition of Random Composites-----	91
	III.2 Tandem Deposition of Random Composites-----	93
	IV. Conclusions and Further Discussions-----	95
Chapter Six	Physical Properties and Applications of Random Composites	
	I. Introduction-----	105
	II. Experimental Results and Discussions-----	106
References	-----	141

Chapter One

Introduction

The term *microstructure* covers structural features in the size ranging from the interatomic distance at several angstroms up to the external shape of the specimen at millimeters or meters. Traditional metallurgists often used it to describe peculiar atomic arrangements in materials such as dislocations, grain boundaries, second chemical phases etc. These microstructures are characteristic of either chemical compositional or crystallographic inhomogeneities that can be observed directly or indirectly by using electromagnetic wave or particle wave scattering methods. By controlling these microstructures, they can obtain desired mechanical properties of materials.

In modern electronic and optical technologies, *microstructure* has been more extensively employed to delineate the arrangements of individual material building blocks in complex devices. The layouts of spatial regions distinctly doped with impurities or those of thin layers of materials deposited for either electrical conductions or insulations in a semiconductor device are, for instances, the common applications of microstructures to obtain certain electrical properties. Physical properties and material processing technologies of submicron microstructures, or even nanostructures for constituents on the order of 10 to 100 Å in size, have been of much interest to the digital IC industry for years as the need for high speed and high circuit density chips becomes more urgent to modern electronic and optoelectronic applications. For examples, multilayered one dimensional quantum well structures such as $\text{Ga}_x\text{In}_{1-x}\text{As}$ for optical and high speed electron devices, also called superlattices, take advantage of the special material arrays to achieve distinguished physical properties.[1-3] In a modulation doped superlattice where the neighboring layers are differentially doped, the heavily doped layers provide high concentration of free carriers which transfer across the junctions into the lightly doped layers where the transport mobility is high due to less impurity scattering.[2]

There are other types of multilayered structures using alternating layers of a variety of dielectric materials, or sometimes called the Layered Synthetic Microstructures (LSM), widely used for Fabry-Perot etlons in X-ray and UV-VIS-IR optics.[4] Recently, a research group in General Electric R&D Center has made use of the multilayered coating on light bulbs to reduce power dissipation. In these coatings, the multilayers selectively keep infrared radiation (heat) inside the bulb, letting go of visible light for illumination. Besides these examples, there are numerous other material properties that can be achieved by microstructure engineering.

This work deals with the relationship between the microstructure and physical properties of inhomogeneous materials consisting of small metal particles dispersed in semiconductors or dielectrics. While the term *heterostructure* has been widely accepted for multilayered one dimensional quantum well structure or 1-D superlattice, it can also be used here to describe a *random composite* of small metal particles randomly distributed in a semiconductor since this is simply a *disordered three dimensional quantum well structure*, or a "*random heterostructure*", whose heterojunctions form between the metal particles and the semiconductor. The microstructure of a random composite is defined by the geometric configuration of the small metal particles embedded in the semiconductor. A geometric configuration is determined by (1) the metal particle volume fraction, (2) particle size, (3) aggregation of metal particles, (4) particle shapes and (5) the environment (i.e. the semiconductor) in which those particles are embedded.

The goals of this research have been to seek novel material or device microstructures for high efficiency room temperature photodetector applications mainly in the visible and infrared regimes. Since a high efficiency photodetector requires, first of all, high rate of photoexcitation, we take advantage of the high density of free electrons ($6 \times 10^{22} \text{ cm}^{-3}$ for Ag[5]) in metals as a good resource of photoelectrons. The free carriers in a bulk metal, however, do not absorb light in the visible and infrared radiations because, due to no restoring force, these electrons oscillate in accordance with the incident wave, resulting in the re-emission (reflection) of electromagnetic waves from the accelerated charged particles(i.e., oscillating electrons). But they can be rendered

E.M. wave absorbing by imposing geometric boundaries on them, that is, by enclosing these free electrons in metal particles. In the presence of particle boundaries and for sufficiently small particles, the build-up of surface charges, at the incidence of the electromagnetic wave, gives rise to a restoring force that leads to the resonant density of conduction (free) electrons at a suitable (resonant) frequency. This is one kind of surface-enhanced photoabsorption. After being photoexcited, the electrons may photoemit externally into the vacuum or internally into the neighboring medium and be collected. Metals in particulate form also give rise to enhanced photoemission, compared to the bulk metals in planar form, because of the elastic and diffuse scattering of these photoexcited electrons at the particle boundaries, as will be discussed in Chapter IV.

The idea of using small metal particles dispersed in semiconductors originated from the previous studies on the S-1 photocathode which consists of small silver particles embedded in semiconducting cesium oxide.[6-16] Although the S-1 photocathode has been with us for almost six decades, there are still a number of issues concerning its mechanism of photoemission and the interpretation of its spectral response curves. The reasons for this long-time controversy are due partly to the complex microstructure of the S-1. I shall thus devote a fair portion of this research to theoretically investigate the optical and photoemissive properties of the S-1 photocathode. Based upon these theoretical results, we will then be able to understand the physics behind this unique photocathode which, among those so far commercially available, shows the longest cut-off wavelength in the near infrared. With this photocathode as a model system of our investigation, we can summarize the material design-rules and thereby further tailor other material systems for high photoabsorption in the infrared with similar microstructures using silver particles dispersed in semiconductors such as silicon.

Photoemissive devices are ideally suited to the detection of faint signals, high speed pulses of radiation and for uses requiring high spatial resolution such as imaging. In the modern optical communication technology, $1.3\mu\text{m}$ or even $1.55\mu\text{m}$ semiconductor lasers which show the least

optical loss and dispersion in the glass fiber certainly require novel photodetectors that are fast and have low noise amplification.[17] For these reasons, a photoemissive device has an advantage over other types of photodetectors, namely, photoconductive and photovoltaic devices. By properly incorporating the cathode and scanning electron beam read-out components in a photomultiplier, one can routinely fabricate a large area detector for low noise, fast and high spatial resolution imaging applications.

One may still query the advantage of using small metal particles in photocathode applications, knowing that the cesiated III-V quaternary or ternary alloy semiconductor quantum well structures, such as InGaAsP, InAsP and $\text{In}_{0.18}\text{Ga}_{0.82}\text{As}$, have shown cut-off wavelengths close to $1.1\mu\text{m}$, comparable with the S-1, and their reported quantum efficiencies of 5-9% are approximately one to two orders of magnitude greater than that obtained from classical photoemitters. Fig. 1.1 shows the spectral response for a number of commercially available photocathodes.[18,19] The S-1 photocathode has been the only photocathode commercially available that operates in the near infrared and shows the longest threshold wavelength. It has been reported to be sensitive both at 1.468 and $2.94\mu\text{m}$ radiations from an actively mode-locked Yttrium-Erbium-Aluminum Garnet laser with picosecond pulses.[20] While the quantum efficiency (photoelectrons per incident photon) of the III-V Negative Electron Affinity (NEA) device is higher than the S-1 and both of their thresholds are comparable, the threshold of GaAs:Cs device is largely limited by the junction barrier height between cesium or cesium oxide and GaAs which depends upon the energy gap and doping level of the semiconductor.[21] The electronic energy band diagram is given in Fig. 1.2 where a spike of around 1.1eV is shown at the heterojunction between GaAs and Cs(CsO_x). The cut-off wavelength is thus restricted to around $1.1\mu\text{m}$ for the III-V materials. The band diagram for the S-1 is given in Fig.4.1b of Chapter Four. Both devices are limited by the heterojunction barrier height, although field-enhanced photoemission may be employed to narrow the barrier width and extend the spectral response more into the infrared. Among the surface activated NEA photoemissive materials, silicon was

once thought of as advantageous due to its narrow band gap of 1.1eV ($1.1\mu\text{m}$). It produces a higher photoyield than InGaAs, owing to its long lifetime and hence long carrier escape depth ($10\mu\text{m}$), regardless of the small optical absorption constant due to its indirect band gap.

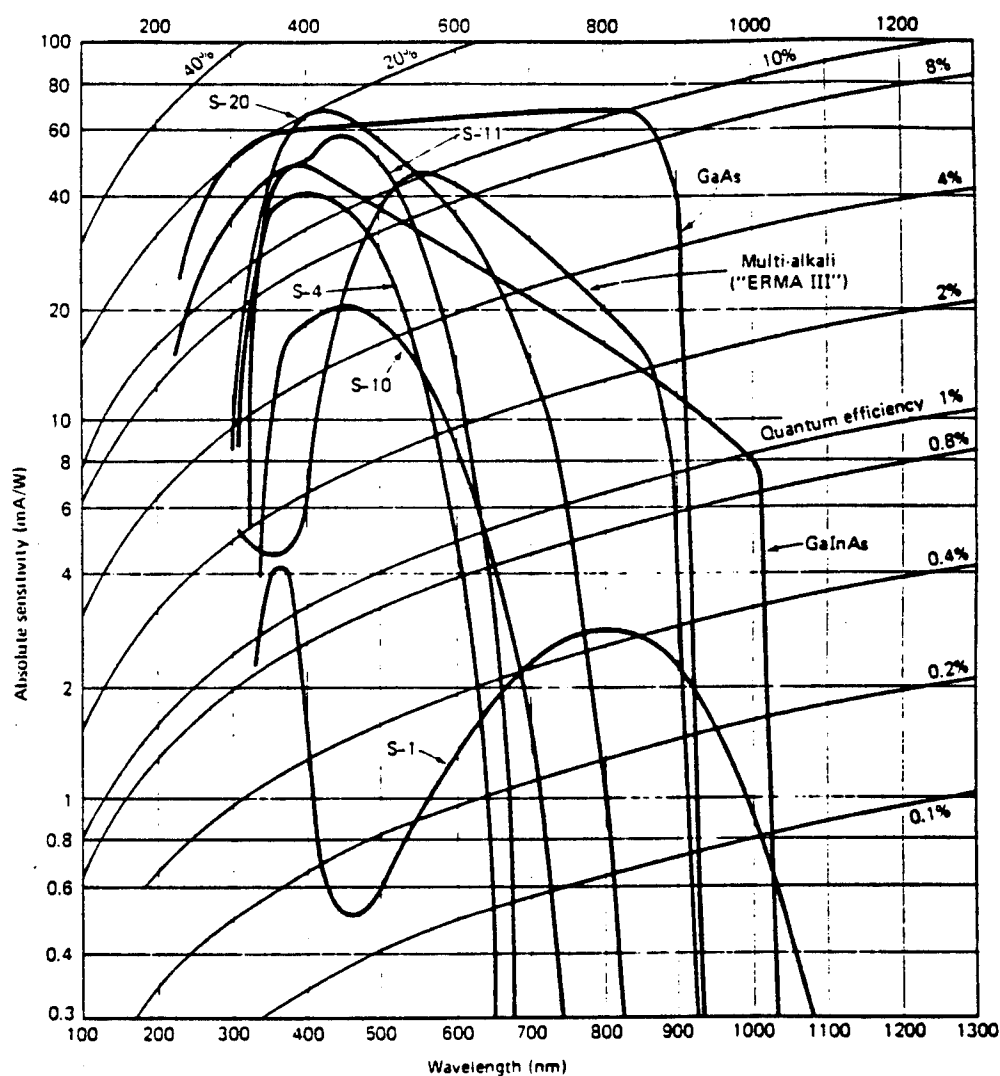


Fig.1.1 The quantum yield curves of commercial photocathodes.[18]
The designation for various cathodes is given in ref. 19.

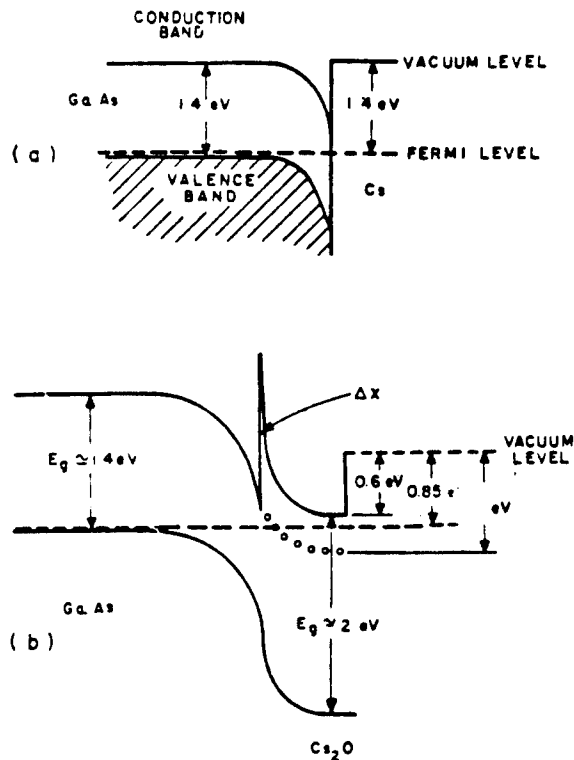


Fig. 1.2 The Band diagrams of GaAs:Cs NEA devices

Unfortunately, it also has quite high thermionic emission (dark) current, about 1 nA/cm^2 at room temperature, which is many orders greater than those of other III-V NEA cathodes.[17] Besides, the cesiation of silicon turned out to be critical and only the (100) surface can be made NEA. These have limited the use of silicon per se for photoemissive device applications. To suppress the dark current, or, from another point of view, to increase the signal to noise ratio, we were led to believe that the high electron density of metal incorporating the enhanced photoeffects from small metal particles would contribute to a great amount of photoelectrons.

As we have argued, photoemissive devices seem impossible to operate beyond the limit of

1.1 μm . For longer wavelength we thus have to resort to other modes of operation such as photoconductive, photovoltaic and photothermal modes. Since many metal-semiconductor junctions show barrier heights lower than the value of 1.1 eV, potential material systems other than Cs_2O , such as Ag-Si, became targets of research for longer wavelength purposes.

As mentioned earlier, an efficient photodetector should exhibit high rate of photoexcitation, high mobility of electron transport, high speed of response, low noise and long lifetime of free carriers. Current efforts have been to seek new materials and devices suitable for various wavelength regions and meeting the above-mentioned requirements. Up to now, the fastest devices regarding the rise time are of the photoconductive type, where values below 1ps have been reported.[22] Schottky junction diodes show fast rise times in the picosecond range, while they don't have the disadvantage of slow decay as most photoconductive detectors do.[23] Meanwhile, dark currents which may be substantial in extrinsic semiconductors can be alleviated by introducing Schottky junctions.

The major difficulties in the fabrication of the Schottky diodes, however, are the insufficient transparency of contacts and parasitic capacitances. These difficulties can be overcome by making these junction contacts in the form of small metal particles dispersed in the semiconductor which are supported by insulating substrates. The total Schottky junction area is greatly increased under such circumstances. The optical absorptions and the rate of internal photoemission are also tremendously enhanced due to the confinement of conduction electrons in the metal particles. On account of the high electron densities in metals, the photosensitivities of such structures will thus be much higher than those of extrinsic semiconductors while thermal noises can be significantly reduced due to the presence of Schottky barriers.

The Schottky barrier height of Ag-Si interface is believed to be around 0.5 - 0.7eV ($\sim 2.5 - 1.8 \mu\text{m}$) which is the threshold for a detector based on this heterogeneous material. This makes the Ag-Si system a good candidate for 1.55 μm optical detection operating in the photoconductive or photovoltaic mode. In the mean time, the facts that Ag and Si do not form compound and are

immiscible in one another make it possible to process Ag particles dispersed in silicon. Naturally, for electrons to transport through the composite, surface or interface recombinations at the metal particle - semiconductor boundaries and contact resistance have to be considered. The electrical transport of the random heterostructure is itself an independent research subject and will not be attacked in this work. The theme of this dissertation is to first obtain the material design rules of a random heterostructural system for optical detector applications, and then go about synthesizing materials according to these rules.

For a composite with microstructures as complex as a random dispersion of small metal particles in the semiconductor, it is not easy to create an exact theory to precisely account for its physical properties. Nevertheless we found that, when aggregations of particles are taken into account, the effective medium approximation (EMA) is a good approach to physically describe the optical properties of heterostructures of small metal particle systems. In Chapter II, I will discuss various approximation methods and their adequacy to physically picture the composite systems. Having their own respective advantages and limitations, all these approximations can be thought of as an effective medium theory of some sort which serve as the means to obtain the effective dielectric constant of a collection of small metal particles. I shall start with developing the Optical Theorem which brings up an important physical term, the forward scattering amplitude, $S(0)$, to be encountered frequently in this chapter.

Chapter III then develops a theory of photoemission from small particles which can account for the enhanced photoemission as compared with a planar surface. This theory gives an excellent explanation of small particle photoemission phenomenon by considering the scattering of photoelectrons inside small particles as elastic and diffuse. The confinement of these electrons within the particle boundaries thus increases the probability of photoemission due to more frequent encounters of photoelectrons at the boundaries. This phenomenon can simply be described as due to increased interface/junction per unit volume. With this theory and the effective medium theory discussed in Chapter II, Chapter IV are then devoted to the theoretical investigation of a model

system - small Ag particles, the S-1 photocathode. Optical properties of this system will be investigated in detail to establish the relationship between the microstructures and optical properties. Numerical results of quantum yield (photoelectrons per incident photon) of the S-1 photocathode, in comparison with experimental results for different cathodes prepared under different procedures, will be given in this chapter whence we can properly interpret the varieties of measured spectral response (quantum yield) curves as due to their difference in microstructures.

I then proceed to go into the experimental part of this work. Chapter V bears on the material synthesis aspects of the heterostructural systems based mainly on the Ag-Si and Ag-CuInSe₂ systems. The material syntheses and structural analyses of Ag-Si and Ag-CuInSe₂ systems using co-sputtering and tandem deposition methods to produce small particle dispersions will be presented. X-ray diffraction, electron microscopic and photoelectron spectroscopic techniques are used to characterize the microstructures of the prepared films.

In Chapter VI, the optical properties of these materials and their relations to microstructures are then investigated. Although in principle one can invert the measured reflectance and transmittance to obtain the optical functions of the film, it is an formidable task when the film is strongly absorbing since a nonlinearity in extinction coefficient comes in and the solution for complex refraction index $n=n+ik$ requires a tremendous amount of computer time. Therefore, we take the following alternative approach. From the electron microscopic studies, we obtain the microstructural parameters for small particles which are used to calculate the optical properties of the composite film. The experimental data can thus be fitted using a set of parameters representing the microstructure of the composite film. By doing so, experimental results can be properly interpreted from the dielectric functions of the film. This approach also gives more insight into the significance of various parameters.

Finally, proposals for the future studies using solid phase epitaxy (SPE) techniques and several device structures will be projected for small silver particles dispersed in single crystal silicon film.

Chapter Two

Interactions of Electromagnetic Radiation with Small Metal Particles – The Optical Constants of Composites –

I. Introduction to Small Metal Particles

Because of the random arrangements, size distributions and shapes of small particles, we have to look at their statistical physical properties based upon the knowledge of the properties of individual particles. When the particle volume fraction is high and therefore the inter-particle distance is small, these particles would interact with one another in a complex manner which makes it very difficult to perform an exact calculation with all interactions included in order to obtain accurate physical properties of these particles. Through adequate approximations on the full electromagnetic scattering theory, however, it may, in the first place, be easier to gain some insight into the physics of these interactions and, secondly, the properties of these particles might be calculated more easily with satisfactory accuracy. The consideration of interactions between particles is contained in the so-called effective medium approximation (EMA) for small particle systems or, equivalently, the coherent potential approximation (CPA) widely used in electronic structure calculations of semiconductor alloys and disordered systems.[1] Although it's found that the dynamic effective medium approximation (DEMA)[2-5] has been able to nicely account for the experimental results of this work, I shall make comments in the forthcoming sections on the physical significance of various approximations, in addition to DEMA, as well as their applicabilities and limitations. The objective of the theoretical calculation pursued in this chapter is simply to obtain the effective dielectric constant of a small metal particle system, from which the optical and photoemissive properties can be calculated(see Chapter Four). Looking into the match and mismatch between these approximations and measured properties allow us to understand the importance of various physical parameters and how small metal particles respond to the incident

electromagnetic radiations.

Some typical questions one might at first ask is "what is a small metal particle?" and "when is it considered small and when is it large?" Or alternatively, "when and how does metallic behavior recede with decreasing particle size until down to the atomic state?" Answers to these questions depend on which physical properties are under examination and what kind of probing means are employed. For example, optical and magnetic measurements may both show size effects, although of different origins. While magnetic properties may depend on the parity of electron number in a particle, the optical properties may be quite sensitive to the surface plasmon modes which are functions of particle sizes and collective interactions among particles.[6]

Now that the purpose of this chapter is to look into the electromagnetic properties of the small particles, the sizes of the "small" metal particles are assumed to be much smaller than the wavelength of the probing wave so that the wave can not resolve individual particles. This assumption is not necessary in the general sense since for all problems in optics, in principle, one should be able to solve the Maxwell Equations with particular boundary conditions for distinct particle systems. Nevertheless, both the mathematics and physics simplify to a great extent if the randomly distributed many-particle system can be regarded as homogeneous as a whole when the individual particles cannot be resolved by the probing wave. The upper bound of the particle size in this calculation can thus be set to be, for example, a few tenths of the wavelength of the probing wave. The lower bound, on the other hand, has to be so as to maintain the continuous electronic energy level in a metal particle and, therefore, the macroscopic dielectric constant can properly describe the particle except for the modification of scattering time. It is technically impractical to isolate a single particle a few hundred angstroms in size and determine its properties. The dielectric constants of a single particle do not seem directly measurable. To obtain the dielectric constants of a single particle, usually one has to measure those of the bulk material which are then modified for size effects, as will be discussed later. In order for this approach to be valid, the quantization of energy level should not come into play, or put it another way, the electromagnetic

interaction with small particles should fall within classical limit. Generally speaking, the particle size will be smaller than a few thousand angstroms in diameter and larger than a few tens angstroms, corresponding to about a thousand to many millions of atoms. Energy level spacings of about 0.086 meV (1°K) can be found for particles of 100\AA in size.[6] At room temperature (300°K), the electron gas in such particles can therefore be considered classical, i.e., with continuous electronic energy levels. This argument can be justified using the free electron model of solids in which the discrete energy level spacing is inversely proportional to the particle volume V_0 (or $1/6 \pi d^3$, d being the diameter).[6-10] For the approximations we will be investigating in this chapter, it is assumed that the sizes of particles are much smaller than the wavelength of the probing wave while large enough so that macroscopic dielectric constants are proper physical quantity for these particles.

For good free electron metals such as aluminum, silver, gold and copper, the free electron part of the dielectric constants of a small particle can be obtained by adding to the electron scattering rate a term due to the scattering at particle boundaries in addition to the electron-electron, electron-phonon scatterings etc. The total dielectric constant can be separated into the free electron and bound electron parts, i.e., $\epsilon_j = \epsilon_j^f + \epsilon_j^b$, where j indicates either bulk or particulate metal. Using the Drude model for metals,[9-11] one can write

$$\epsilon_{\text{bulk}}^f = 1 - \omega_p^2 / [\omega (\omega + i / \tau_{\text{bulk}})], \quad \text{and} \quad (2.1)$$

$$\epsilon_{\text{particle}}^f = 1 - \omega_p^2 / [\omega (\omega + i / \tau_{\text{particle}})] \quad (i^2 = -1), \quad (2.2)$$

where $\omega_p = 4\pi N e^2 / m_0$ ($\approx 9.2\text{eV}$ for Ag) is the free electron plasma frequency, N is the density of the conduction electrons and m_0 is their effective mass in the metal. Assuming that the bound electron part remains the same for both cases, the dielectric constant for a spherical metal particle can be written as the following:

$$\epsilon_{\text{particle}} = \epsilon_{\text{bulk}} - \epsilon_{\text{bulk}}^f + \epsilon_{\text{particle}}^f. \quad (2.3)$$

The dielectric constants of bulk continuous Ag for $h\nu > 0.6\text{eV}$ (or $\lambda < 2\mu\text{m}$) are given by Johnson and Christy,[12] while for $\lambda > 2\mu\text{m}$ they are obtained from Eqn.(2.2 and 2.4) directly where silver metal is free-electron like. The scattering rate in the particle, $1 / \tau_{\text{particle}}$, is the sum of the scattering rates at the boundary and inside the particle. The bulk silver scattering time is $\tau_{\text{bulk}} = 3.1 \times 10^{-14}$ sec given also by Johnson and Christy. This value is not too far away from 1.44×10^{-14} sec given by Hodgson.[13] The total scattering time in τ_{particle} in the silver particle is hence given by

$$1 / \tau_{\text{particle}} = 1 / \tau_{\text{bulk}} + V_F / d, \quad (2.4)$$

where V_F is the Fermi velocity of electrons in the silver metal taken as 1.38×10^8 cm / sec [9] and d is the diameter of the spherical particle.

Having obtained the dielectric constant for a single spherical particle, we are ready to use various approximation methods to calculate the effective dielectric constants of a collection of small metal particles. To sum up, this chapter concerns the theories of the wavevector independent but frequency dependent dielectric constants of small metal particle systems in the classical electrodynamic limit. I will present various theories which are to be adopted in the following chapters to calculate and physically interpret realistic material properties.

II. Electromagnetic Interactions with Small Particles

The problem of electromagnetic scattering by small metal particles can be solved, in general, by considering the particles as independent electric and magnetic current sources \mathbf{J} and \mathbf{M} , respectively, in a medium.[16-18] The electromagnetic fields caused by such sources at any point in the medium satisfy the Maxwell's equation with associated boundary conditions depending on the nature of the scatterers and the surrounding medium. This has been done in many classic works among them the most often cited is that formulated by Gustave Mie for particle diameters not too much smaller than the probing wavelength, although it has been pointed out that some of

the most eminent 19th and early 20th century mathematical physicist also worked on the problem.[14-17]

While Mie scattering theory is a conceptually simple boundary value problem, the full solution is a formidable algebraic task. Besides, it is good only for low particle volume fractions where particles act as independent scattering centers and multiple scattering is not important. In reality, however, these conditions may not hold true. Yet, a great deal of later work has been built upon or derived from Mie theory as will become clearer as this chapter develops.[15] In what follows, I will make comments on these efforts, while leaving detailed derivations to the cited original articles or books, and finally go into the why's and how's of the so called dynamic effective medium approximation to be employed in this research to calculate the optical properties of the small metal particles and their relationships to the microstructures.

II.1 Forward Scattering and Optical Theorem

As mentioned above, the scattering of radiation by small particles can be treated as a boundary value problem. One common approach is to use dyadic Green's functional method which gives the scattered field far away from the particle as: [15-18]

$$E_s(r) = S(\theta, \phi) \{ \exp(ikr) / (-ikr) \}, \quad (2.5)$$

where $S(\theta, \phi)$ is called the vector scattering amplitude, k is the wavevector in the medium and θ, ϕ are, as shown in Fig. 2.1, the azimuthal and polar angles respectively. For far field approximation where $kr \rightarrow \infty$, the scattered wave has the form of outgoing transverse spherical wave. The rate at which the electromagnetic energy is extinguished can be shown to be, with I_i being the incident irradiance,

$$W_{\text{ext}} = I_i (4\pi/k^2) \cdot \text{Re} \{ [S(\theta, \phi) \cdot x] \}_{\theta=0}, \quad (2.6)$$

where \mathbf{x} is the polarization vector of the incoming wave. Note that $W_{\text{ext}} = -\int \mathbf{S}_{\text{ext}} \cdot d\mathbf{A}$ and $\mathbf{S}_{\text{ext}} = c/8\pi \text{Re}\{\mathbf{E}_i \times \mathbf{H}_s^* + \mathbf{E}_s \times \mathbf{H}_i^*\}$ corresponding to the interference of the incoming and scattered fields. The extinction cross section $C_{\text{ext}} = W_{\text{ext}} / I_i$ and hence

$$C_{\text{ext}} = 4\pi/k^2 \cdot \text{Re}\{S(0)\}, \quad (2.7)$$

where $S(0) = [S(\theta, \phi) \cdot \mathbf{x}]_{\theta=0}$ is called the forward scattering amplitude and ϕ disappears due to circular symmetry in the incident direction.

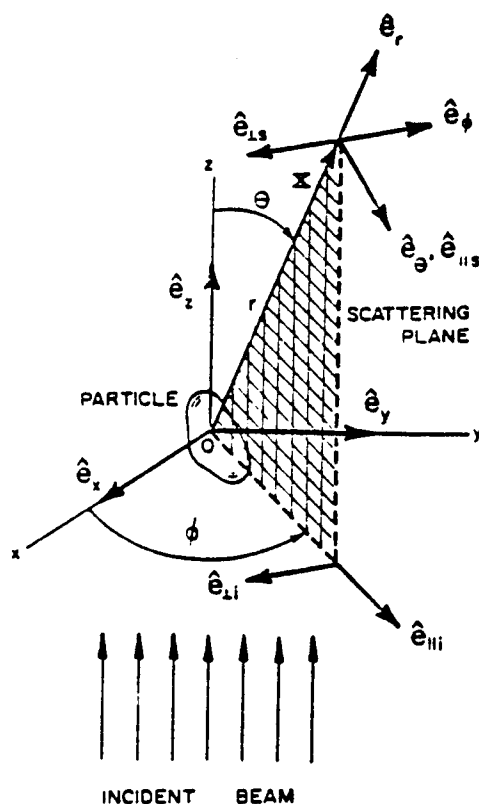


Fig. 2.1 Scattering by an arbitrary particles.[from 15]

Equation (2.7) is a special form of the optical theorem which expresses a fact: the extinction cross section simply depends on the scattering amplitude in the forward direction $S(0)$, yet the extinction is the combined effect of optical absorption in the particle and scattering in all directions by the particle, or $C_{\text{ext}} = C_{\text{abs}} + C_{\text{sca}}$, C_{sca} being the scattering cross section and [15,16]

$$C_{\text{sca}} = 4\pi/k^2 \sum_n (2n+1) \{ |a_n|^2 + |b_n|^2 \}. \quad (2.8)$$

$$C_{\text{ext}} = 4\pi/k^2 \sum_n (2n+1) \text{Re}\{ a_n + b_n \}. \quad (2.9)$$

Combining Equations (2.7) and (2.9), we have

$$S(0) = 1/2 \sum (2n+1) \{ a_n + b_n \}, \quad (2.10)$$

where a_n and b_n , respectively, are the electric and magnetic multipole contributions to the scattered fields due to the small particle scattering, equivalent to the partial-wave scattering amplitudes [4,16,17] of scattered electromagnetic waves from a coated sphere. The scattered field calculated from the Mie theory can thus be considered as generated by a superposition of the scattered oscillating electric and magnetic multipoles. The functions a_n and b_n determine the magnitude of the corresponding n th multipole moments.

For very small particles, only the first order electric and magnetic terms dominate and the extinction will be mainly due to the photoabsorption. The series expansion of the coefficients is given as the followings:[7]

$$\begin{aligned} a_1 &= (2i/3)n_0^3 x^3 (n^2 - n_0^2) / (n^2 + 2n_0^2) + (2i/5)n_0^5 x^5 (n^2 - n_0^2)(n^2 - 2n_0^2) / (n^2 + 2n_0^2)^2, \\ b_1 &= (i/45) n_0^5 x^5 (n^2 - n_0^2), \\ a_2 &= (i/15) n_0^5 x^5 (n^2 - n_0^2) / (2n^2 + 3n_0^2), \end{aligned} \quad (2.11)$$

where $x = k_0 d/2$, d is the diameter of the particle, $n^2 = \epsilon_1 + i \epsilon_2$, $n_0^2 = \epsilon_m$, $k_0 = 2\pi/\lambda_0$ and λ_0 is the wavelength in vacuum. In the limit $n_0 k_0 d/2 \ll 1$, only the electric dipole term a_1 is significant and the extinction coefficient can be written as

$$\begin{aligned}\alpha_{\text{ext}} &= (N/V) C_{\text{ext}} = \pi/2 (N/V) n_0 k_0 d^3 \text{Im}\{ \epsilon - \epsilon_m / \epsilon + 2 \epsilon_m \} \quad \text{or} \\ \alpha_{\text{ext}} &= 18\pi (N/V) V_0 n_0^3 / \lambda_0 \{ \epsilon_2 / [(\epsilon + 2 \epsilon_m)^2 + \epsilon_2^2] \},\end{aligned}\quad (2.12)$$

where N/V is the particle concentration and V_0 is the volume of each particle. Note that a resonance will occur when $\epsilon + 2 \epsilon_m = 0$. This equation can also be derived using the Maxwell-Garnett approximation to be given in the next section. To understand the nature of this resonance, it is illustrative to look at the polarization field due to the particle using the quasi-static approach as follows. It is well known from electrostatics that the polarization \mathbf{P} in a sphere with dielectric constant ϵ embedded in a medium of dielectric constant ϵ_m is

$$\mathbf{P} = (3/4\pi) (\epsilon - \epsilon_m) / (\epsilon + 2 \epsilon_m) \mathbf{E}_{\text{loc}}, \quad (2.13)$$

which is established by the surface charge density $\sigma_{\text{pol}} = \mathbf{P} \cdot \mathbf{r} / r$, where \mathbf{E}_{loc} is the local field acting on the particle to be given later. At a frequency ω_R where $\epsilon + 2 \epsilon_m = 0$, the polarization is infinite. As this happens, the electrons oscillate collectively (plasma oscillation). This surface plasma resonance at ω_R , as is obvious from the above arguments, corresponds to the lowest order electric dipole contribution to the scattering in the Mie theory.

II.2 Quasi-Static Effective Medium Approximations

In the quasi-static case, frequency dependent effective dielectric constants are derived using the electrostatic theory. The assumption here is that the wavelength of the probing wave is much greater than the particle size so that the heterogeneous composite medium can be regarded as

homogeneous since the wave cannot resolve the individual particles. There are two approximations falling into this category. One is the Maxwell-Garnett approximation (MGA)[19] which is equivalent to the Clausius-Mossotti theory (CMT),[18] the other is Bruggman's effective medium approximation (EMA).[20] Both MGA and EMA consider a particle embedded in an effective medium consisting of the rest of the composite. Since the particle size is very small, we regard the medium void of a sphere as effectively equal to the whole medium. In the presence of these polarizable particles, the induced dipole moments in the medium will add to the original induced field due to the host medium an extra polarization which will also contribute to the effective dielectric constants of the composite. The extra polarization for a spherical particle composite can be written as

$$\Delta P = p (3/4\pi) [(\epsilon - \epsilon_m) / (\epsilon + 2\epsilon_m)] E_{loc} = (1/4\pi) (\epsilon_{eff} - \epsilon_m) E_o \quad (2.14)$$

where $p = NV_o/V$ is the particle volume fraction, E_o is the applied field, E_{loc} is the Lorentz local field acting on the particle and

$$E_{loc} = \epsilon_m E_o + (4\pi/3) \Delta P / \epsilon_o = 1/3 (\epsilon_{eff} + 2 \epsilon_m) E_o. \quad (2.15)$$

Upon substitution of Eqn.(2.14) into Eqn.(2.15), we have the following result:

$$(\epsilon_{eff} - \epsilon_m) / (\epsilon_{eff} + 2 \epsilon_m) = p (\epsilon - \epsilon_m) / (\epsilon + 2 \epsilon_m). \quad (2.16)$$

This result is the so-called Maxwell-Garnett approximation originally derived by Maxwell-Garnett in 1904.[19] From the local field point of view, we may as well interpret the MGA through the modified Clausius-Mossotti relation for spheres surrounded by a medium: the effective polarization is simply the sum of induced polarizations from all the particles. However, it is true only when dipole-dipole interactions and higher multipole terms are not important. The MGA thus

seems to hold true only if the particle concentration p is not too high and the particle size much smaller than the wavelength of probing wave.

In reality, nevertheless, the volume fraction of particles can be high and therefore the embedding host matrix may become surrounded by the metal particles, that is to say, the dielectric or semiconductor matrix has been inverted to isolated particles. Such being the case, the two microstructural components should be treated on an equal footing with both regarded as particles embedded in a medium consisting of the rest of the materials whose dielectric constant is ϵ_{eff} . As to be given below, this is exactly what the EMA does.

In order to be consistent with the condition that the effective medium should appear homogeneous to the probing wave, the average induced dipole moment due to the particles of the two kinds should vanish on the average. This self-consistent condition is the essential part of the EMA first proposed by Landauer in 1952 to calculate the electric resistivity of binary metallic mixtures.[21] Since the dipole moment induced in a particle of the component i with dielectric constant ϵ_i is proportional to $(\epsilon_i - \epsilon_{\text{eff}}) / (\epsilon_i + 2\epsilon_{\text{eff}})$, we thus have, for metal particles with volume fraction p and dielectric constant ϵ ,

$$p(\epsilon - \epsilon_{\text{eff}}) / (\epsilon + 2\epsilon_{\text{eff}}) + (1 - p)(\epsilon_m - \epsilon_{\text{eff}}) / (\epsilon_m + 2\epsilon_{\text{eff}}) = 0. \quad (2.17)$$

While it is well known that the MGA account for the dielectric anomaly but gives no percolation threshold, the EMA gives a threshold at $p \approx 1/3$ but does not predicts the dielectric anomaly.[1,21-25] The dielectric anomaly has been observed for many small particle systems. It is an anomalous optical absorption at certain resonant frequency that occurs in the small particles but does not occur in the continuous material of the same kind. Similar to what ionic molecules do in a vibrational spectrum where there is an anomalous dispersion at resonance frequencies, the conduction electrons confined in the small particles, at the excitation of electromagnetic waves, will also give rise to some kind of anomalous dispersion at particular frequencies.

Now, the question arises as to how accurate these approximations are and what is the underlying physics responsible for the differences. It is assumed in the MGA that the particles of one component are dispersed in the host matrix of the other in an asymmetric fashion. As shown in Fig. 2.2, it has been proven by G. B. Smith[26] that, equivalent to EMA, MGA is also a kind of effective medium approximation which takes each individual spherical particle as surrounded by a eccentric shell of host matrix material with shell thickness determined by the volume fraction of the particles. Dispersed in an effective medium of dielectric constant ϵ_{eff} , these coated particles are considered as if in isolation. The field outside the spheres is determined self-consistently, i.e., the field in the composite should be uniform statistically and equal to that produced by a coated sphere independent of the distance from the sphere. It appears from the original derivation of Eqn.(2.16) that MGA is a theory good only for small p , as just discussed above. However, this restriction is much alleviated according to Smith's approach. In reality, MGA has been widely applied quite successfully for many systems in predicting dielectric anomaly for intermediate volume fraction even at $p \approx 0.4$. [26-29] Since all particles are regarded as isolated, it is not surprising that the percolation threshold doesn't exist in the MGA. When there is a microstructural inversion, that is, the original host matrix become particles isolated by the other component, one has to convert the MGA formula by exchanging p with $1-p$, ϵ with ϵ_m and vice versa. It is thus understandable that the MGA still works for intermediate p value so long as the nature of complete particle isolation of either kind (metal or dielectric particles) is maintained.

On the other hand, the microstructural inversion occurs automatically in the EMA where, as mentioned above, we treat both constituents symmetrically. The solution to Eqn.(2.17) is, with $q=1-p$,

$$\epsilon_{eff} = 1/4 \{ (3q-1) \epsilon_m + (3p-1) \epsilon + [((3q-1) \epsilon_m + (3p-1) \epsilon)^2 + 8 \epsilon \epsilon_m]^{1/2} \}. \quad (2.18)$$

The percolation threshold occurs at $p = 1/3$ beyond which metal particles connect to each other forming semicontinuous (i.e., porous or labyrinthine) structure. For metal particles embedded in an

insulating host matrix, the electrical conductivity drops to zero below percolation threshold due to the complete breakage of conduction path. This can be appreciated by replacing all the dielectric constants in eqn. (2.18) with corresponding conductivities since $\epsilon = \epsilon_1 + i 4 \pi \sigma / \omega$. Note also that the EMA reduces to the MGA at low p where particle isolations of one component prevail.

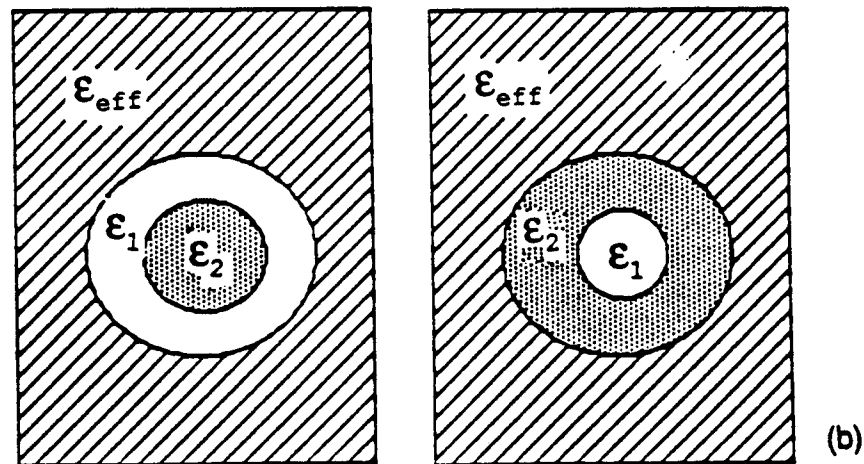
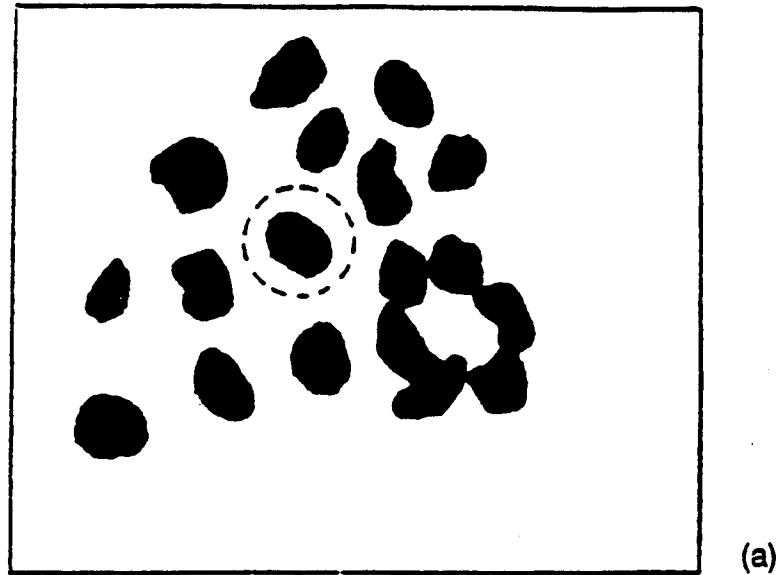


Fig. 2.2 Isolated and clustered particles (a) can be modeled as two microstructural units (b).

Now, the question remains: "Why does the EMA fail to predict the dielectric anomaly?" Is it a matter of the assumption of self-consistency, i.e., the vanishment of average dipole moment in a random composite? Is it because the requirement $n_0 d/2 \ll 1$ does not hold true? Is it associated with higher multipole terms yet to be included in the EMA? Or, are we modeling the microstructure of the random heterostructure properly? Answers to these queries can be obtained by looking at several recent works in this area concerning the relationship between the physical properties and microstructures. Sheng[23] has shown that by incorporating the coating of particles of one component with a shell of the other, the dielectric anomaly of a small particle system can be predicted using the EMA. Since we do not see any inadequacy of the self-consistency condition that the whole collection of particles be regarded as homogeneous since the particle size is much smaller than the wavelength of the probing wave, we believe that accurately modeling the microstructures of composites is crucial to the successful application of EMA. Sheng's formalism applies to spheroids in general, although it considers only the electric dipole term. It is true that this term dominates for very small particles.[2-4] In our experiments, however, we may have particle sizes as large as 1000\AA ($0.1\text{ }\mu\text{m}$) as compared with $0.4\text{ }\mu\text{m}$ to several μm 's for the wavelengths of concern. To properly model these systems with particle sizes of this order of magnitude, we need to take higher order terms, at least the eddy current (magnetic dipole) contribution, into consideration. The self-consistency requirement that the effective medium be regarded homogeneous remains valid still. This is to be accomplished by the so-called DEMA to be given below.

II.3 Dynamic Effective Medium Approximation (DEMA)

Although the higher order terms such as the magnetic dipole contributions may become significant for larger particles, only electric dipole terms are considered in the quasi-static approach treated above. These higher order terms will be included in the dynamical approach. The DEMA, similar to the EMA, requires that the effective medium appears homogeneous to the probing wave.

Consider a plane wave propagating through such a medium with effective wavevector $k_{\text{eff}} = \omega/c[\epsilon_{\text{eff}}]^{1/2}$, and $E_{\text{inc}} = E_0 e^{ik_{\text{eff}}z - i\omega t}$ with $E_0 = (x+iy)E_0/2$, where $x+iy$ is the polarization vector of the wave. As mentioned earlier in Eqn.(2.5), the scattered field in the far (radiation) zone can be written as $E_s(r) = S(\theta, \phi) \{ \exp(ikr) / (-ikr) \}$. Since $\theta \ll 1$, only the forward scattering is important and $S(\theta, \phi) \rightarrow S(0) = S(\theta, \phi)|_{\theta=0}$. The total field in the medium can be written as $E_{\text{tot}} = E_{\text{inc}} + E_s$. For a random distribution of small particles, an average has to be taken over all the particles, i.e. $E_{\text{tot}} = E_{\text{inc}} + \langle E_s \rangle$. Now, the self-consistency condition requires that $E_{\text{tot}} = E_{\text{inc}}$, we therefore have $\langle E_s \rangle = 0$. Equivalently, $\langle S(\theta, \phi) \rangle_{\theta=0} = 0$ or $\langle S(0) \rangle = 0$, where $S(0) = S(\theta, \phi)|_{\theta=0} \cdot (x+iy)$ is the forward scattering amplitude with the average running over all particles composing the composite.

Let there be ρ_j particles of j th type, we have from eqn.(2.10) the followings:

$$S(0) = 1/2 \sum_j \sum_n \rho_j (2n+1) \{ a_n + b_n \}. \quad (2.19)$$

If the particle size varies obeying the distribution function $\rho_j(R)$, we have

$$S(0) = 1/2 \sum_j \sum_n \int dr \rho_j(R) (2n+1) \{ a_n(r, R, \epsilon_j, \epsilon_j, \epsilon_{\text{eff}}) + b_n(r, R, \epsilon_j, \epsilon_j, \epsilon_{\text{eff}}) \}. \quad (2.20)$$

When $d \ll \lambda$, only a_1 and b_1 are significant, therefore for those coated spheres of inner radius r and outer radius R with corresponding dielectric constants ϵ_j and ϵ_j respectively, it has been shown that [4] $a_1 = i x^3 (2/3) T/U$ and $b_1 = i x^5 (1/45) [\epsilon_j - \epsilon_{\text{eff}} + (r/R)^5 (\epsilon_j - \epsilon_j)] / \epsilon_{\text{eff}}$, where $x = 2\pi R/\lambda$ is the size parameter of the coated sphere of outer radius R ; V and W are given as

$$V = (\epsilon_j - \epsilon_{\text{eff}}) (\epsilon_j + 2\epsilon_{\text{eff}}) + (r/R)^3 (\epsilon_j - \epsilon_j) (2\epsilon_j + \epsilon_{\text{eff}}), \quad (2.21)$$

$$W = (\epsilon_j + 2\epsilon_{\text{eff}}) (\epsilon_j + 2\epsilon_j) + 2(r/R)^3 (\epsilon_j - \epsilon_j) (\epsilon_j - \epsilon_{\text{eff}}). \quad (2.22)$$

Note that $(r/R)^3 = p$ is the volume fraction of particles of certain type. The effect of increasing particle size on the magnetic dipole contribution to dielectric constants is thus clear from the equations. To understand the particle size distribution effect, let us assume a particle size distribution function of γ -type which is given as $\rho_j(R) = R^\alpha \exp[-\alpha R/R_m]$, where α is the distribution factor defining the range of the size distribution and R_m is the mode radius, i.e., the radius where $\rho_j(R)$ peaks. Fig. 2.3 gives a qualitative picture of this function for various α . The requirement of vanishing forward scattering amplitude thus lead to the following results.[2] For small α , the variation in size is tremendous and the effect will be prominent as can be seen from the gamma function term. Significant magnetic contribution is closely tied to this wide range of particle size distribution.

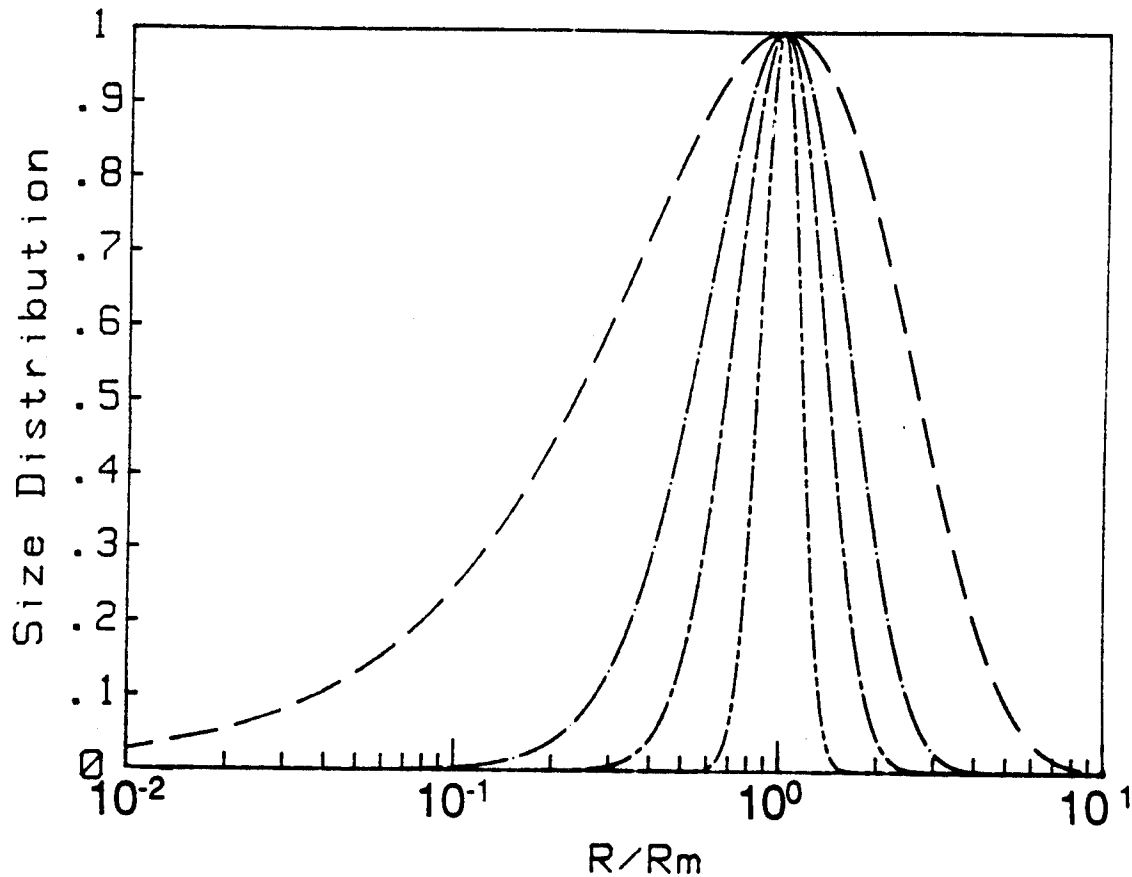


Fig. 2.3 γ -type distribution of particles. It changes from broad ($\alpha=1$) narrow ($\alpha=50$) as α increase. $\alpha=100$ is close to single size. --- $\alpha=1$, -.-.- $\alpha=4$, - - - $\alpha=10$, — $\alpha=50$.

III. Particle Aggregations and Electromagnetic Properties

We have shown that the way particles are arranged is critical to the outcome of the effective dielectric constant. The MGA treated the particles of one type as totally in isolation while the EMA considered the constituents in a symmetric way. Envisaging composites with these two distinct types of particle arrangements gives quite different optical behaviors: the former gives the dielectric anomaly but fails to predict a percolation threshold while the latter the reverse.[22-25] The microstructure is thus crucial to accurately predicting the physical properties of composites. We have already seen that the particle volume fraction, particle size, type of particles and embedding host matrix all come into the formalism of the effective medium approximation. What have been left out still are the clustering effect (i.e., aggregation) and the particle shape effect.

When particles coalesce to form aggregates, they may assume either round shapes which can be modeled as shells of particle materials coating the host matrix, or elongated shape which can be modeled as ellipsoids or spheroids. Even for elongated aggregates, we can still look at them as caps or semispherical shells surrounding the host matrix. The fraction, designated as f_2 , of this type of particles relative to the other (isolated particles) can be determined from electron micrographs of the composite.

For realistic materials, inhomogeneity may occur in such a way that part of the heterostructure consists of particles of one type coated by the host material while some other part of host matrix surrounded by the aggregated particles. The latter can be looked upon as a kind of cavity filled with host materials. Since the forward scattering amplitude due to this type of filled cavities is different from the other type of microstructure, the averaging of the forward scattering amplitude should therefore take another route. That is, one ought to take $\langle S(0) \rangle$ as contributed by both types of coated particles. As shown in Fig.2.2, separated particles can be regarded as those coated with host matrix while clustered ones regarded as host matrix coated by a shell of the other component.

Suppose that there is an ensemble of particles in which the j th spherical particle with

dielectric constant x_j^k is surrounded by a spherical shell of material with dielectric constant y_j^k . Furthermore, this ensemble of particles has two units ($k = 1$ and 2) of coated spheres, one with the metal coated by the semiconductor and the other with the semiconductor coated by metal, which makes up an self-consistent effective medium with dielectric constant ϵ_{eff} . This effective medium consists of the rest of the material in which the particle under consideration is embedded. Since the particle size is much smaller than the wavelength, the electromagnetic wave can not resolve the individual particles, the effective medium can be looked upon as homogeneous and, therefore, ϵ_{eff} should be constant as a function of spatial position. The forward scattering amplitude $S_k(0)$ for the plane electromagnetic wave scattered from such a collection of individual types of coated spheres indexed with k , where $k = 1$ for the first unit and $k = 2$ for the second unit, can be written in the following form:[2-4]

$$S_k(0) = 1/2 \sum_j \sum_n (2n+1) \iint dr dR \rho_k(R) [a_n(r, R, x_j^k, y_j^k, \epsilon_{\text{eff}}) + b_n(r, R, x_j^k, y_j^k, \epsilon_{\text{eff}})], \quad (2.23)$$

where $\rho_k(R)$ is the size distribution of the k th microstructural unit of coated spheres with the inner sphere of radius r and the outer sphere of radius R , with $r = R \cdot p^{1/3}$. The double sums run over all multipoles (n) and all types of particles (j).

For the j th component of particles of the first unit microstructure, $x_j^1 = \epsilon_m$ is the dielectric constant of the metal particle (the inner sphere of radius r) given by Eqn.(2.3) and $y_j^1 = \epsilon_M$ (the spherical shell of outer radius R) is the dielectric constant of the host (semiconductor) matrix assumed constant in the range of frequency concerned. If the j th particle is of the second microstructure, $x_j^2 = \epsilon_M$ (the inner sphere of radius r), $y_j^2 = \epsilon_m$ (the spherical shell of outer radius R). Under the condition that the particle size is much smaller than the wavelength of the incoming electromagnetic radiation and that the dielectric constants of the components are not too large, it was found[16] that only the dipole terms a_1 and b_1 are important. Suppose that the fraction of the first and the second microstructural unit are f_1 and f_2 respectively, where $f_1 + f_2 = 1$, the DEMA

leads to the conclusion that the forward scattering amplitude of the scattered wave from an ensemble of two types of coated small particles, with particle size much smaller than the wavelength, should vanish on the average,[5] namely,

$$f_1 S_1(0) + f_2 S_2(0) = 0. \quad (2.24)$$

This is the condition for the extended DEMA that takes the two types of microstructural units into consideration. The self-consistency condition still states that the averaged forward scattering amplitude vanishes for a random heterostructure with particle size much smaller than the wavelength of probing wave. Knowing the particle size $d = 2r$, the volume fraction of the metal particles $v = (r/R)^3$, the fraction of the second unit f_2 and the dielectric constants of Ag and the semiconductor, we can employ (2.23) & (2.24) to solve for ϵ_{eff} . we can then calculate the optical properties of the effective medium.

This theory will be tested in Chapter Four on the Ag-O-Cs photoemitting surface (S-1 photocathode) which is composed of cesium-suboxide-coated silver particles embedded in cesium oxide with $\epsilon=4.5$ for the base layer and cesium-suboxide-coated silver particles embedded in a matrix of $\epsilon=1$ (vacuum) for the surface layer which is normally obtained by additional silvering on the base layer of Ag-CsxO composite.[29] Based on the success in interpreting the spectral response of the S-1 photocathode by using this effective medium theory and the theory of photoemission from the small particles to be presented in the upcoming chapters, they will be extended to other random heterostructures in order to infer general relationships between the microstructure and physical properties of small particle systems.

Chapter Three

Photoemission from Small Particles

I. Introduction

In the classic experiments of Schmidt-Ott, Schurtenberger and Siegmann (SSS),[1] it was found that the photoelectric quantum yield (PQY) at the threshold of small metal particles of Ag, Au, MoO₃ and WO₃, all assumed spherical, are on the order of 10-100 larger than that from large radii cylinders (which may be regarded as plane surfaces) of the same materials. Efforts to explain this result based on the different geometries showed that at most an enhancement factor of four was possible under the assumption of a homogeneous source strength/volume for photoexcited electrons with $h\nu$ close to the metal work function ϕ_w ; the metal work function [2] and spatially varying photon field near the metal particle surface have been suggested as the cause of enhancement.[3,4]

In our studies of the S-1 (Ag-O-Cs) photoemitting surfaces[5-7] which involve enhanced PQY of 100 from Ag microparticles 50Å in diameter relative to bulk Ag, we found it was possible to obtain a theoretical PQY with no adjustable parameters and in remarkable agreement with experimental results for wavelength in the range 0.2 to 1.0µm, if we assumed that photoexcited electrons in the Ag particles were elastically and diffusively scattered from the boundaries. This approach provides a mechanism for reorienting an electron's motion to the proper direction to contribute to photoemission, an effect particularly important in the threshold region and not treated in previous models. Though this geometric factor is only a part of the complete theoretical treatment of this system involving the dynamic effective medium approximation[8] described earlier in the previous chapter, neglecting it would give a PQY near the threshold about 20 times lower than with it.

However, in this chapter we apply this model to a system in which the volume fraction of

particles p is $\ll 1$, for which the Maxwell-Garnett Approximation[9] is known to give good results in describing optical properties of such composites. This system is the Ag aerosol of SSS mentioned above for which the experimental PQY results are given. The aerosol consists of Ag particles in a N₂-O₂ mixture ($\epsilon \approx 1$) with $p \approx 10^{-8}$. We consider a half space of infinite thickness of such a system, a good approximation to the SSS experimental setup to compare with a plane surface of Ag also infinitely thick.

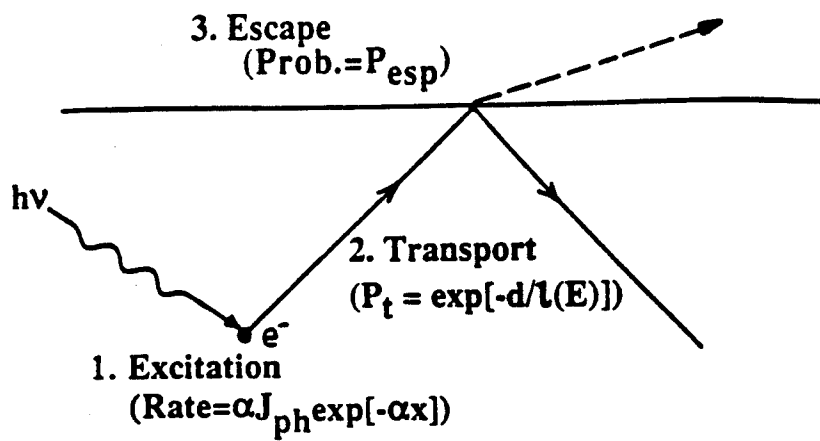
II. Theoretical Foundation

In this study, we shall use the prototype of three-step model of photoemission[10] to calculate the photoelectric quantum yield of small metal particles. The three-step model are widely used and works quite well for planar surfaces of many materials. In this model, as depicted in Fig. 3.1.a, photoemission is treated as a sequence of (1) photoexcitation of an electron, (2) its transport through the solid to the surface, and, finally, (3) the escape through the sample surface into the vacuum. Similar to the case of a planar surface, as sketched in Fig. 3.1.b, photoexcited electrons in small particles are assumed to be scattered elastically from the boundaries and to move within the particles with a probability of reaching the boundaries without inelastic scattering given by $P_t(r, E) = \exp(-z / L(E))$, where z is the distance an electron has to travel to reach the boundary assuming a straight trajectory and $L(E)$ is the escape depth, or roughly, the mean free path of photoexcited electrons in the solids. The photoexcited electrons are otherwise considered to be free. We use the free electron model for Ag whose valence electrons are filling in a potential well of depth $W = E_F + \phi_w$, with the Fermi energy $E_F = 5.51$ eV referring to the bottom of the potential well as zero energy.

Based upon the three-step model of photoemission, the photoyield from a plane surface, Y_p , can be written, with E taken as the energy of electrons in the solid as:[11-13]

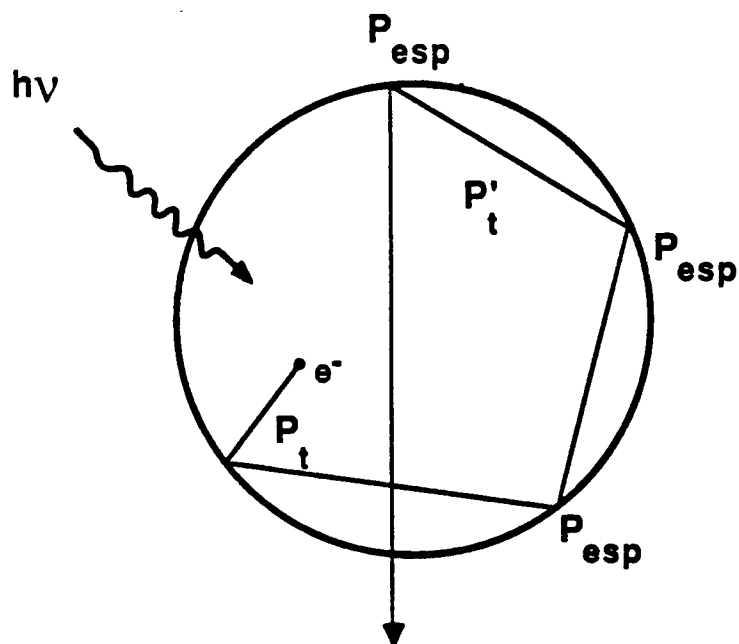
$$Y_p(h\nu) = K^{-1}(h\nu) \int_w^{h\nu + E_F} dE \int_V d^3r \frac{dn(r, h\nu)}{dt} P_{esp}(r, E) P_t(r, E) T(E) [E(E-h\nu)]^{1/2} / \int_A J_{ph}(h\nu) d^2r \quad (3.1)$$

1. Planar Case (Three Step Model)



(a)

2. Particulate Case



(b)

Fig. 3.1 Photoemission from a planar surface (a) and from a sphere (b).

where $K(h\nu) = \int_{X_m}^{h\nu + E_F} dE' [E' (E' - h\nu)]^{1/2}$ is the normalization constant with $X_m = \text{Max}\{E_F, h\nu\}$, the larger of the two quantities; $dn(r, h\nu)/dt = \alpha(h\nu) \exp(-\alpha(h\nu) z) J_{ph}$ is the rate of photo-excitation per unit volume for electrons at a distance z below the plane surface, where J_{ph} is the incident photon flux and α , the absorption coefficient is given by $\alpha = 2\omega/c \text{Im}\{\epsilon^{1/2}\}$; ϵ is the frequency dependent complex dielectric constants taken from the work by Johnson & Christy.[14] $[E(E-h\nu)]^{1/2}$ is associated with the joint density of states[11] for free-electron systems and $T(E)$ the transmission coefficient which, with image field included, is given by[15]

$$T(E) = [1 + W^4 / 16 E_H E^3]^{-1}, \quad (3.2)$$

where E_H is the ionization energy of hydrogen atoms. In the transport function we used the empirical formula for the mean free path of Ag given by $L(\text{\AA}) = 1000/[E(\text{eV}) - E_F(\text{eV})]^2$. [16] The escape function $P_{esp}(E)$ is defined as the probability that an electron, with kinetic energy greater than the depth of potential well ($E \geq W$), hits the surface (or the boundary) at such an angle that the vertical energy $E_{\perp} = \hbar^2 k_{\perp}^2 / 2m$ is still greater than the potential barrier and thus can escape. Let θ be the angle between the k -vector of the electron wave and the normal to the surface. Since $E_{\perp} = E \cos^2(\theta) \geq W$, we have $\theta \leq \cos^{-1}(W/E)^{1/2} = \theta_m$, i.e., for all electron with energy greater than the potential barrier, only those which move in such a direction such that $\theta \leq \theta_m$ can escape. The escape probability is

$$P_{esp}(r, E) = P_{esp}(\theta, E) = (E - W) \Theta(\theta_m - \theta), \quad (3.3)$$

where $\Theta(x)$ is the Heaviside's unit step function. The escape function $P_{esp}(E)$ is simply the volume average of the escape probability, i.e.,

$$P_{esp}(E) = 1/2 \int_0^{\theta_m} P_{esp}(\theta, E) \sin\theta d\theta = 1/2 [1 - (W/E)^{1/2}] \Theta(E - W). \quad (3.4)$$

Upon integration over the whole volume of the half-space, we obtain for Y_p

$$Y_p(h\nu) = K^{-1} \int_w^{h\nu + E_F} dE \{ \alpha(h\nu)L(E)/[1 + \alpha(h\nu)L(E)] \} \{ 1/2[1 - (w/E)^{1/2}] \Theta(E - w) \} T(E)[E(E - h\nu)]^{1/2} \quad (3.5)$$

Next, we consider the corresponding calculation for small particles. Suppose there are a half-space of small particles of volume fraction p suspended in a matrix of dielectric constant ϵ_m . In order to compare the results of this calculation with Schmidt-Ott's work, where Ag particles were suspended in a N_2 - O_2 mixture and $p \ll 1$, we apply the Maxwell-Garnett theory (MGT)[10] to find the effective optical absorption coefficient of the suspension. Since the skin depth of Ag at threshold is around 50\AA , for particles smaller than this the assumption of homogeneous photoexcitation of electrons in Ag particles will be true. As in the case of planar surfaces, we let the small particle suspension fill in a half-space with infinite thickness. The boundary of the half-space is taken as $z = 0$, and the rate of photoexcitation of electrons in a particle at a distance z below the half-space boundary is of the same form as that of the planar surface, except that the absorption coefficient is now the effective value mentioned above. We have assumed a constant excitation rate in small Ag particles although the light intensity gets weaker as it gets farther below the half-space boundary.

For a photoexcited electron at r in a spherical particle centered at $r = 0$, the distance, d , it has to travel to reach the boundary at $r = R$ in order to escape is

$$d(r, \mu) = [r^2 + R^2 - 2rR\mu]^{1/2}, \quad \text{where } \mu = \cos(\mathbf{r} \cdot \mathbf{R}). \quad (3.6)$$

The averaged transport function for the electron to reach the particle boundary is therefore

$$P_t(E) = (4\pi R^3/3)^{-1} 2\pi \int_{-1}^1 d\mu \int_0^R r^2 dr \exp[-d(r, \mu)/L(E)], \quad (3.7)$$

which, upon substitution of d into the integral, gives

$$P_t(E) = 3/2 (L/R)^4 \{2(R/L) - 3 + \exp(-2R/L)[2(R/L)^2 + 4(R/L) + 3]\} \quad (3.8)$$

After a reflection from the boundary, the electron travels a distance $d' = 2R\cos(\beta)$ to reach the boundary again, β being the angle between the radius pointing toward the reflection point and the direction in which the reflected electron is moving. If the electron has $E > W$, but does not move in a favorable direction, i.e., $E_{\perp} < W$, and if the mean free path $L(E)$ of the electron in the particle is long enough, the bouncing back and forth between the particle boundary may, at some point, bring the electron to an orientation more favorable to escape. The chance for the electron to escape is thus increased because of reflections. The probability that the electron can survive any inelastic scattering between two reflections averaged throughout the whole sphere is,

$$P_t'(E) = (L(E)/2R) [1 - \exp(-2R/L(E))]. \quad (3.9)$$

This is the transport function for an electron after the first encounter of the particle boundary.

The probability that an electron will escape after n reflections is

$$P_n(E) = P_t(E) [1 - P_{\text{esp}}(E)]^n P_t'(E)^n P_{\text{esp}}(E) \quad (3.10)$$

where $(1 - P_{\text{esp}})^n$ represents the probability for an electron to reflect n times without escape, $P_t'^n$ is the probability for an electron to reflect n times without inelastic scattering. $P_t P_{\text{esp}}$ gives the probability that the photoexcited electron reaches the boundary without inelastic scattering and escapes. P_n is the probability for an electron to escape at the $n+1$ th encounter at the particle boundary. The total probability for an photoexcited electron to escape is then

$$\sum_n P_n(E) = P_{\text{esp}}(E) P_t(E) / \{1 - [1 - P_{\text{esp}}(E)] P_t'(E)\}. \quad (3.11)$$

With this expression, the photoyield for the suspension of particles of radii R in an semi-infinite half-space can thus be written as

$$Y_R(h\nu) = K^{-1}(h\nu) \int_w^{h\nu + E_F} dE P_{\text{esp}}(E) P_i(E) T(E) [E(E-h\nu)]^{1/2} / \{1 - [1 - P_{\text{esp}}(E)] P_i'(E)\} \quad (3.12)$$

III. Numerical Results and Discussions

We now have an expression for the yield of small spherical particles to compare with the yield of a planar surface. It should be noted that though we consider the reflections of photoexcited electrons at the particle boundary to be elastic, they are also diffuse and not specular, as shown in Fig. 3.1.b, otherwise the angle of incidence would never change in subsequent reflections and the enhancement effects would be lost. Experimental evidence bears this out.[17] Recent studies on the diffuse scattering of electrons at thin film surfaces show that size effects arises from the roughness of thin film surface. For thin film metallic cobalt silicide smooth in atomic scale successfully prepared with modern molecular beam epitaxial growth techniques, the size dependence of electric conductivity is essentially absent.[16] Besides surface roughness, impurities which were present in the original work of SSS[1] – because of their method of small particle productions – could also increase the diffuseness and is discussed later.

The transmission coefficient $T(E)$ and joint density of states $[E(E-h\nu)]^{1/2}$ will not differ substantially between spherical particles and a planar surface unless the lowering of work functions are significantly different from one case to another. In this case the lower work function materials have higher transmission coefficient and also have more photoexcited electrons available to transmit. As a matter of fact, $T(E)$ does not vary significantly for the work function difference in SSS's results. The effects of density of occupied initial state and empty final states will be accounted for in the integration limits to be discussed later.

Let us first consider the situation where $L(E) \gg R$ which holds for the S-1 photocathode near the threshold where photoelectrons have energies $\approx 1\text{eV}$ and $L(E)$ is several hundred to a thousand

angstroms.[20] Here $\alpha = 10^5 \text{ cm}^{-1}$ and $\alpha L/(1+\alpha L)$ and P_t are both ≈ 1 . The factor $\gamma = 1/\{1 - [1 - P_{\text{esp}}(E)] P_t'(E)\}$ then reduces to $1/P_{\text{esp}}(E)$ as $P_t'(E)$ is close to unity. This cancels the $P_{\text{esp}}(E)$ in the numerator of the integrand for Y_R but it remains in the integrand for Y_P . Since at threshold $P_{\text{esp}}(E)$ is about 0.01 to 0.1 the ratio Y_R/Y_P is roughly 10-100. The fact that the lower limit in the integral for Y_R is smaller than the corresponding one for the Y_P , as the measured work function for small metal particles is smaller than that for a plane, will increase this ratio more, so the estimate of the enhancement factor as 10-100 is a conservative one. The lower work function allow more available final states for photoelectrons to scatter to. Meanwhile, the escape probability will also be enhanced. We shall discuss this later.

Now consider the case when $E \approx 5.0 \text{ eV}$, i.e., near the threshold for Ag in vacuum. Here $L(E) \approx 40 \text{ \AA}$ and γ factor is only 2-5 and $P_t \approx 0.5$ for $R=30 \text{ \AA}$. With $\alpha = 7 \times 10^5 \text{ cm}^{-1}$, $\alpha L/(1+\alpha L)$ is now 0.2. P_t and p_t' are both ≈ 1 . The ratio Y_R/Y_P is roughly 5-10 from these considerations alone. Additional factors come from the smaller work functions measured for small metal particles compared with that of a plane surface (the lower integration limit for Y_R is now smaller than that for Y_P). For example, consider $h\nu=4.98 \text{ eV}$ and $R=30 \text{ \AA}$ in the expression for P_{esp} . For a plane $\phi = 4.9 \text{ eV}$, $W = 5.51 + 4.9 = 10.41 \text{ eV}$ and $E_F+h\nu=5.51+4.98=10.49 \text{ eV}$. Hence for the upper limit in the integrand $P_{\text{esp}}(\text{plane}) = 0.002$ and the lower limit is zero. For $R=30 \text{ \AA}$, $\phi=4.55 \text{ eV}$, we have $W=5.51+4.55=10.06 \text{ eV}$. $P_{\text{esp}}(\text{sphere})=0.01$ for the upper limit and zero for the lower limit. As the intervals of integration for both Y_P and Y_R are $E_F+h\nu-W = 0.08$ and 0.43 , respectively, this produces an enhancement for $Y_P/Y_R = 0.01 \times 0.43 / 0.002 \times 0.08 \approx 25$, where we have applied the Mean Value Theorem of calculus for this evaluation. The enhancement factor is therefore on the order of 100.

As a comparison, we plot in Fig. 4.15 of the next chapter the PQY for the S-1 (Ag-O-Cs) photocathode with and without multiple reflections in the silver particles. Here the multiple reflection dominates and the enhancement factor is about 20.

In table I we present the numerical results for Ag aerosols of various radii compared with a

plane surface of Ag. Data are given, respectively, for $h\nu = 4.98$ and 5.11 eV near the threshold. Note that our results agree quite well with experiment at $R=30\text{\AA}$. The deviation by a factor of about 2 for the other two smaller particles may be due to the mean free path considerations.

Table I
Comparison of PQY of theory and experiment for various sizes

$h\nu$ (eV)	$R(\text{\AA})$	Φ_w (eV)	Y(theory)	Y(experiment)
4.98	20	4.65	3.05×10^{-4}	9.69×10^{-4}
	27	4.57	3.81×10^{-4}	6.55×10^{-4}
	30	4.55	3.47×10^{-4}	3.33×10^{-4}
	∞	4.90	2.13×10^{-6}	4.67×10^{-7}
5.11	20	4.65	3.05×10^{-4}	9.69×10^{-4}
	27	4.57	3.81×10^{-4}	6.55×10^{-4}
	30	4.55	3.47×10^{-4}	3.33×10^{-4}
	∞	4.90	1.44×10^{-5}	3.22×10^{-6}

More recently, H. Burtscher, A. Schmidt-Ott and H. C. Siegmann (BSS) measured the PQY of clean and contaminated Ag particles about 100\AA in diameters.[21] Our earlier contention that impurities increase the diffuse scattering and hence the multiple scattering effect is strengthened by the results given in Fig. 3.2 which compares the theory for Ag particles with and without multiple scatterings with the data for contaminated and clean Ag. The PQY taken from BSS was not absolute and are therefore normalized to 5 eV for comparison.

In Fig. 3.2 the results are not plotted beyond 8 eV. The reason for this is that according to BSS a distortion of the S-band density of states at the surface results in some change in the PQY above this energy and we have not included such a distortion in our theory.

The main point of this theory, however, is that the geometric factor alone may well explain the enhanced photoemission from small particles as compared with a planar surface of the same material though a microscopic theory may be necessary to explain all details. We will use this theory to calculate the photoemissive properties of the S-1 photocathode with various types of microstructures in the next chapter.

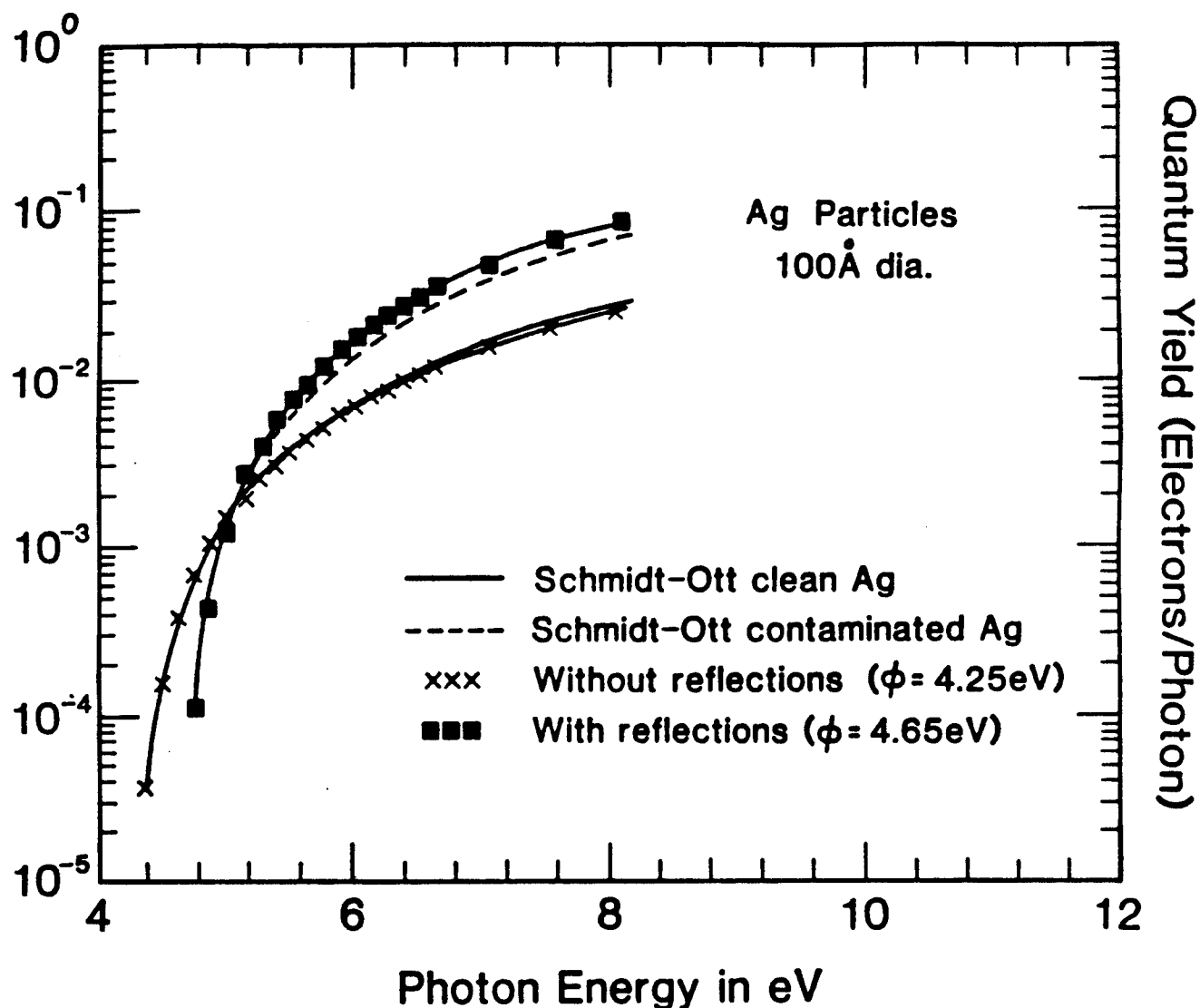


Figure 3.2 Photoelectric quantum yield of clean and contaminated Ag compared with theory for Ag with and without multiple scattering.

Chapter Four

Relationships between Microstructures and Optoelectronic Properties of S-1 Photoemitting Surfaces

I. Introduction

Since the S-1 (Ag-O-Cs) photocathode was discovered as the first non-metallic photoemitting surface in 1929,[1] a tremendous amount of work has been performed in an effort to understand its mechanism of photoemission. The controversy on the photoemission mechanism and its relation to the optical properties of this cathode remains unsettled even after almost six decades of endeavor. Most of the research on this surface up to 1967 are discussed by Sommer in his fine book entitled "Photoemissive Materials".[2] In the latest edition, Sommer prefaced his book in 1980 with a statement noting "recent work has not invalidated any information contained in the book". Without rewriting the book due to no significant breakthrough from 1968 to 1979, he added references of over 250 relevant articles covering this period.

The reason for this sluggish progress in better understanding the S-1 may be due to its sophisticated microstructure. In a recent publication, Bates,Jr. and Alexander[3] proposed a microstructural model of the S-1 photocathode consisting of a photosensitive surface layer with Cs_{11}O_3 -coated Ag particles suspended in vacuum ($\epsilon=1$) which resides on a base layer with Cs_{11}O_3 -coated Ag particles embedded in a matrix of Cs_2O ($\epsilon=4$). The most photoelectronically sensitive Ag particles were determined to be on the order of 50 Å in diameter produced near and on the surface by heating employed in the photocathode processing. Fig. 4.1.a and 4.1.b show respectively the electronic energy band diagram and microstructure proposed for this system. The microstructural model is based on the results of x-ray photoelectron spectroscopy (XPS)[4-6] and Raman spectroscopy.[7] The coating of silver particles with Cs_{11}O_3 are very thin and thus do not affect the polarizability and therefore the dielectric constants of these particles. The microstructure

was considered to consist of two units, Cs_{11}O_3 -coated Ag particles surrounded by the host matrix (first unit) and the matrix surrounded by the Cs_{11}O_3 -coated Ag particles (second unit). The concept of these two types of microstructural units were first used by Sheng to calculate the optical properties Au-SiO₂ granular composites[8]. The response of these two types of microstructures to electromagnetic radiations is discussed in the book by Bohren and Huffman.[9]

To account for the photoelectric quantum yield (PQY) of the S-1 surface in the near infrared, we found it absolutely necessary to include these two basic microstructural units. We allowed 2% (or more) of the photocathode volume to consist of the second microstructural unit and the remaining 98% (or less) the first unit. Furthermore, our calculations (Section II) indicate that the surface layer in the S-1 is the major contributor to the PQY throughout its spectrum. In 1976, Ebbinghaus, Braun and Simon[10] proposed a model of the S-1 indicating for the first time the presence of Cs_{11}O_3 along with Ag. Their UPS measurements did not indicate the presence of Cs_2O presumably because the electron escape depth using the He-I resonance line at 21.2 eV was too shallow to detect it.[3,11] But it is not clear from their work whether they actually produced a S-1 surface, or what structural relationship existed between the Ag and Cs_{11}O_3 as in our model. These considerations aside it is interesting that in their model of the S-1 they attribute the PQY to Ag and Cs_{11}O_3 in vacuum ($\epsilon=1$) whereas in Bates,Jr. and Alexander's model the major contribution to the PQY is due to the Cs_{11}O_3 -coated Ag particles in two types of microstructural configurations in a medium with $\epsilon=1$.

Meanwhile, Wu also observed[12,13] from both electron microscopic and photoyield studies, that small metal particles are responsible for the spectral response of the S-1 photocathodes in which it was found that S-1 surfaces with smaller Ag-particle size showed higher photoyield. Wu constructed an "equivalent diameter particle" theory to explain the PQY of the S-1 only in the near infrared and found the the equivalent diameter particle size that best fitted the experimental data was about 31Å in fair agreement with Bates,Jr. and Alexander's 50Å.

However, Wu's electron transport function, also used in Bates,Jr. and Alexander's

work[3] to calculate the PQY of the S-1, left an adjusting factor to be determined by experimental data-fitting. To get around this adjusting factor, we now construct a multiple-step model of photoemission incorporating the optical absorption obtained from the extended dynamic effective medium approximation described in Chapter Two to calculate the PQY of the S-1 photocathode. We are able to successfully reproduce the PQY curve for the S-1 photoemitting surface without using Wu's transport function. The multiple-step model is an extension of the theory of photoemission from small particles developed in the previous chapter. Included in this model is that photoexcited electrons in small metal particles are scattered elastically from the boundaries and travel inelastically within. The many-body interactions are included in the measured mean free path of the photoexcited electrons.[14] As discussed in the previous chapter our results on the Ag particles in N_2-O_2 aerosols agree very well with experimental results.

In order to understand the relationships between the microstructure and the optoelectronic behavior of the S-1 photocathode at various regimes of photon energy, we have to look further into its optical properties. This is accomplished in section III by analyzing the effective dielectric constant, optical loss function and quality factor of the surface layer. By so doing, we are able to interpret the characteristics of the PQY curves of the S-1 photocathodes as a function of photon energy and microstructure. From this theoretical study, some material design rules can be inferred. According to these rules, one can systematically search for other heterogeneous materials for optical and optoelectronic applications.

II. Multiple-Step Model of Photoemission

The S-1 photocathode is composed of a surface layer (~ 100Å thick) residing on a base layer (~ 300 Å thick) as has been shown in Fig. 4.1.a. Considering the energy band diagram of each layer, respectively, as shown in Fig. 4.1.b, let's first look at the base layer with Ag particles embedded in a matrix of Cs_2O (Fig. 1a). In this layer, the multiple-step model takes into account (1) the excitation of the electrons in the metal particles; (2) the transport of photoexcited electrons

to the interfaces between the metal particles and the Cs_2O ; (3) the transmission and escape (penetration) of the photoexcited electrons through the Schottky barrier (Ag- Cs_2O interface) into the Cs_2O ; (4) the transport of transmitted photoexcited electrons in Cs_2O to the Cs_2O -vacuum interface and (5) the transmission and escape of these electrons into the vacuum which then become the photoelectrons.

As was done in Chapter III, we again employ the free electron model for Ag whose valence electrons fill up a potential well of depth $W = E_F + \phi_b$, with $E_F = 5.51 \text{ eV}$ referring to the bottom of the potential well as zero energy. $\phi_b = 1.06 \text{ eV}$ is the Schottky barrier height. Based upon the multiple-step model of photoemission described above, the PQY of photoemission from the base layer can be written with E being the energy of photoelectrons in the vacuum as

$$Y_B(h\nu) = K^{-1}(h\nu)(1-R) \int_{E_b-E_v}^{h\nu-E_v+E_c} dE \int_V d^3r \frac{dn(r,h\nu)}{dt} P_t^m(r,E) P_{esp}^m(r,E) \cdot T_1(E) \cdot P_t^s(r,E) P_{esp}^s(r,E) T_2(E) [(E+E_v)(E+E_v-h\nu)]^{1/2} / \int_A d^2r J_{ph}(h\nu), \quad (4.1)$$

where R the reflectance at the surface, J_{ph} , dn/dt and the joint density of states[15] for a free electron system are as defined in the previous chapter. The remaining terms in the integral correspond to various steps of photoemission to be explained below. Note that the effective dielectric constants or optical absorption coefficients are calculated using the extended DEMA described in Chapter II. The probability $P_t^m(r, E)$ that the electron will survive any inelastic scattering in the distance d in the silver metal particles is now

$$P_t^m(r, E) = \exp[-d(r)/L_m(E)], \quad (4.2)$$

where $L_m(E) (\text{\AA}) \sim 1000 / (E+E_v-E_F)^2 (\text{eV}^2)$ is the mean free path of the photoexcited electron[14] in the metal particle. The super- and subscript m's stand for metal.

The transport function, $P_t^m(E) = \langle P_t^m(r', E) \rangle_{r'}$, is

$$P_t^m(E) = 3/2 (L_m/R)^4 \{ 2(R/L_m) - 3 + \exp(-2R/L_m) [2(R/L_m)^2 + 4(R/L_m) + 3] \}, \quad (4.3)$$

where the average $\langle \rangle_{r'}$ is carried out through the whole volume of a particle.

The transport function for an electron traveling in between the particle boundaries is

$$P_t^m(E) = L_m(E) / 2R \{ 1 - \exp [-2R / L_m(E)] \}. \quad (4.4)$$

$P_{esp}^m(E) = \langle P_{esp}^m(r, E) \rangle_{r'}$ is the escape function and

$$P_{esp}^m(r, E) = \Theta(E + E_v - W) \Theta(\theta_c - \theta), \quad (4.5)$$

$$P_{esp}^m(E) = 1/2 [1 - (W / E + E_v)^{1/2}] \Theta(E + E_v - W), \quad (4.6)$$

where E_v is the vacuum level at the Cs_2O surface. $E + E_v$ is the energy of the photoexcited electron in the silver particle and $W (= E_b)$ is the potential barrier the electron has to overcome in order to penetrate from a silver particle into the cesium oxide.

The transmission coefficient for electrons crossing the the interface is now[16]

$$T_1(E) = \{ 1 + E_b^4 / [16 E_H (E + E_v)^3] \}^{-1}, \quad (4.7)$$

where E , again, is the energy of the photoelectron vacuum. $E_b (= W)$ and E_v are, respectively, the potential barrier height at the silver-cesium oxide interface and the vacuum level of the Cs_2O as indicated in the Fig.1b. Upon transmitting through the barrier E_b , only those electrons with energy greater than E_b are considered allowed to transmit. In calculating the transmission coefficient at the Schottky barrier, we do not employ WKB method, in which the width of

Schottky barrier has to be involved, in order not to introduce more physical complications.

After penetrating into the Cs_2O , the probability for the electron to survive all inelastic scattering is

$$P_t^s(\mathbf{r}, E) = \exp [- |\mathbf{r} - \mathbf{r}_0| / L_s(E)], \quad (4.8)$$

where \mathbf{r}_0 is the location where the electron was photoexcited and \mathbf{r} gives the locus of the electron and L_s is the mean free path of the electron in the Cs_2O taken to be a few hundred Å's. For electrons in cesium oxide with kinetic energy greater than the electron affinity of the cesium oxide, only those with vertical energy greater than the electron affinity of the cesium oxide will be escaping. The escaping function can be written as [17-19]

$$P_{\text{esp}}^s(E) = 1/2 [1 - (\chi / E)^{1/2}], \quad (4.9)$$

where χ is the electron affinity of the Cs_2O , E is the energy of the photoexcited electron in the cesium oxide and the superscript s stands for the semiconductor which is Cs_2O . Adhering to the convention that E is the photoelectron energy in the vacuum, we may rewrite (4.9) as

$$P_{\text{esp}}^s(E) = 1/2 \{ 1 - [(E_v - E_c)/(E + E_v - E_c)]^{1/2} \}, \quad (4.10)$$

where E_c is the bottom of the conduction band of Cs_2O .

Finally, for those electrons that are ready to escape, a potential step from E_c to E_v will be perceived. This leads to a transmission coefficient $T_2(E)$ which may be written as

$$T_2(E) = \{ 1 + (E_v - E_c)^4 / [16 E_H (E + E_v - E_c)^3] \}^{-1}. \quad (4.11)$$

Using Eqn.(1) through (16), we readily obtain for $Y_B(h\nu)$

$$Y_B(h\nu) = K^{-1}(h\nu)(1-R) \int_{E_b-E_v}^{h\nu-E_v+E_c} dE [(E+E_v)(E+E_v-h\nu)]^{1/2} [\alpha L_s / (1 + \alpha L_s)] \cdot \{1 - \exp[-(\alpha+1/L_s)H_b] \cdot T_1(E) \cdot P_{\text{esp}}^m(E) \cdot P_t^m(E) \cdot T_2(E) \cdot P_{\text{esp}}^s(E) / \{1 - [1 - P_{\text{esp}}^m(E)] P_t^{m'}(E)\} \}. \quad (4.12)$$

Note that the integration limits in (4.12) have been set in such a way that only the electron energy greater than the potential barrier $W=E_b$ are to be counted. This takes care of the condition imposed earlier saying that only those electrons with $E > W=E_b$ are transmitted. This expression is the photoelectric yield for the base layer of the S-1 photocathode.

Next, let's consider the surface layer where silver particles are coated with Cs_{11}O_3 and are suspended in the vacuum with $\epsilon = 1$. The coating of Cs_{11}O_3 works only to lower the work function of the silver particles from 4.9 eV to about 1.1 eV but it does not contribute to the dielectric constants of the particles since it is very thin.[3,12,13] (Fig.4a & b) The photoemission process thus reduces to (1) photoexcitation, (2) transport of electrons to the particle boundaries and (3) elastic multiple scattering or transmission of electrons at boundaries. To obtain the PQY of this layer, we can still use (4.12) in which several parameters require corrections. We can do this by replacing H_b , the thickness of the base layer, with H_s , the thickness of the surface layer. Meanwhile, since the Cs_2O has to be replaced by vacuum, we can put $L_s(E)$ as infinite and $T_2(E) = 1$. The vacuum level E_v also has to be replaced with E_b . Furthermore, the integration limits have to start from zero energy to $h\nu - \phi_w = h\nu - (E_b - E_F)$, i.e., the extreme photoelectron energy. The PQY due to the surface layer can thus be written as

$$Y_S(h\nu) = K^{-1}(h\nu)(1-R) [1 - \exp(-\alpha H_s)] \int_0^{h\nu-E_b+E_F} dE \{[(E+E_b)(E+E_b-h\nu)]^{1/2} \cdot T_1(E) \cdot P_t^m(E) \cdot P_{\text{esp}}^m(E) \} / \{1 - [1 - P_{\text{esp}}^m(E)] P_t^{m'}(E)\}. \quad (4.13)$$

The total PQY is thus

$$Y(h\nu) = Y_S(h\nu) + Y_B(h\nu) \cdot T(h\nu) \cdot [1 - P^{2/3}], \quad (4.14)$$

where $T(h\nu)$ is the transmittance of incident electromagnetic wave at the surface-base layer interface. P is the volume fraction of the silver particles in the surface layer. The factor $1 - P^{2/3}$ gives the effective area for the electrons in the base layer to get into the vacuum without been screened by the silver particles on the top. Eqn.(4.14) is the equation we employed to calculate the quantum yield of the S-1 photocathode. What remain to be determined are the optical absorption coefficients of each layer. As mentioned earlier in the introduction, we will use extended DEMA to calculate the effective dielectric constant of the heterogeneous system whence we can get the absorption coefficients. In what follows, we will present these results.

III. Optical Properties of the S-1 Photocathode

Although the properties of the S-1 have been studied in great detail since its discovery in 1929[1], few studies have looked at the relationship between its microstructure and optoelectronic properties. Notable exceptions include the work by Asao [20] who observed that the absorption peak of the Ag film used in S-1 production move to longer wavelengths with increasing thickness and that by Wu[12,13] whose "equivalent particle size" approximation suggested the importance of the smaller Ag particles in determining the photoemissive properties of the S-1. Sommer[2] also observed that the optical properties of the S-1 was also somewhat insensitive to the silver deposited during the additional silvering process in S-1 production. This silvering process sometimes reduced the long wavelength threshold although it did increase the PQY. Our recent efforts on this surface have emphasized the microstructure-optoelectronic properties relationship. This section gives a general picture of how the microstructure parameters influence the optical properties of the S-1 photocathode and other random heterostructures.

We'll show the calculated optical properties of random heterostructures including the S-1

photocathode using the extended DEMA mentioned previously. In the case of S-1, the multiple reflection of light[21] at the interface between various layers of a multilayer system made up of vacuum ($n=1$) / surface layer / base layer / glass substrate ($n = 1.5$), where n represents the index of refraction, is accounted for in this calculation. Also, without losing insight into the physics of photoemission of the S-1, we have assumed the normal incidence of radiations which, unlike the p-polarized wave at oblique incidence, can not provoke collective motion of electrons (plasma resonance - longitudinal mode) in the films of random heterostructures. The film is transparent to incident wave at the plasma frequency as will be shown later.

The frequency-dependent dielectric constants of bulk silver for the S-1 and bulk gold and copper for other calculations are taken from the work by Johnson and Christy.[22] Because of the scattering of electrons at the metal particle boundaries, the dielectric constant of a single spherical metal particle can be obtained by modifying the scattering time (mean free collision time) of the electrons in the metal as treated in Eqn.(2.1)-(2.4). The bulk silver scattering time is $\tau_{\text{bulk}} = 3.1 \times 10^{-14}$ sec given also by Johnson and Christy. This value is not too far from 1.44×10^{-14} sec given by Hodgson.[23] Meanwhile, the Fermi velocity V_F of electrons in the silver metal is taken as 1.39×10^8 cm/sec.

As mentioned previously, we have to consider two types of microstructural units for the heterostructural systems we are dealing with in this work. From electron microscopic studies of the S-1 photocathode[12,13], it has been shown that silver particles exist both in the forms of isolated islands and aggregated particles. The isolated silver particles can be modeled as metal particles coated with shells of semiconductor (cesium oxide) which are called the first units. While the aggregated silver particles, on the other hand, can be modeled as semiconductor particles coated with metal shells and are called the second units. Again, suppose there is an ensemble of particles in which the j th spherical particle with dielectric constant x_j^k is surrounded by a spherical shell of material with dielectric constant y_j^k . Furthermore, this ensemble of particles has the two units ($k = 1$ and 2) of coated spheres, one with Ag particles coated by

cesium oxides and the other with cesium oxides particles coated by silver metals which form as a result of Ag-particles aggregation.

For the first unit microstructure, $x_j^1 = \epsilon_m$ is the dielectric constant of the silver particle (the inner sphere of radius r) given by Eqn.(2.1-2.4) and $y_j^1 = \epsilon_M$ (the spherical shell of outer radius R) is the dielectric constant of the host matrix (cesium oxide or vacuum) assumed constant in the range of frequency concerned. If the j th particle is of the second microstructure, $x_j^2 = \epsilon_M$ (the inner sphere of radius r), $y_j^2 = \epsilon_m$ (the spherical shell of outer radius R). With all these information, we are now in a position to calculate the optical properties of the S-1 photocathode.

Consider first the optical properties of the surface layer of the S-1 photocathode. As mentioned earlier in Section II, it is an 100Å thick layer of Ag particles suspended in a matrix whose dielectric constant ϵ is 1. The Ag particle size is 50Å and the Ag volume fraction is 50% in which 2% are the aggregated Ag particles. This surface layer resides on a 300Å thick base layer of $Cs_{11}O_3$ -coated Ag particles embedded in cesium oxide ($\epsilon = 4$). In the base layer, the Ag particle volume fraction is again 50% and the particle size ranges from $\approx 100\text{Å}$ to $\approx 1500\text{Å}$. The variation of particle size obeys the γ -type distribution function with mode radius $R_m = 700\text{Å}$. [24] The γ -type size distribution function is $\rho(R) = R^\alpha \exp(-\alpha R / R_m)$. Specifically in this calculation, α is a distribution factor taken as ≈ 4 in the size distribution for the base layer just mentioned. These two layers together on a glass substrate ($n \approx 1.5$) make up the S-1 photocathode.

Figs. 4.2-4 show the optical absorption coefficient and the corresponding transmittance, reflectance, absorptance and optical conductivity of the surface layer. In Fig. 4.2, we see that the absorption coefficient of the bulk silver is fairly constant from the visible into the infrared. The high absorption coefficient corresponds to high reflectivity in this wavelength range, i.e., the free electrons contribute to the scattering rather than the absorption of the E. M. wave. For Ag particles at 3.8 eV ($\approx 0.33 \mu\text{m}$), there is a dip which is due to the plasma oscillations as will become clear later on. Below $0.33 \mu\text{m}$ (or roughly above 4 eV), interband transitions come into play [25] due to the Ag 4d electrons at 4 eV below the Fermi energy. For the particulate Ag

system, the absorption coefficient is lower than that of the bulk Ag. However, as shown in Fig. 4.3, the absorptance of the S-1 surface layer is higher than the bulk Ag beyond $0.33\ \mu\text{m}$. The reflectivity of the S-1 surface is considerably lower both in the visible and infrared than that of the bulk Ag as shown in Fig. 4.4, where we include the T and R of both particulate and bulk (continuous) Ag film of the same mass thickness (100\AA for the former and 50\AA for the latter) for comparison. In Fig. 4.3 at $\approx 0.41\ \mu\text{m}$, there is an enhanced absorption due to the bound nature of the free electrons in the Ag particles. This peak is called the dielectric anomaly or the anomalous dispersion which is due to the isolated Ag particles. The optical conductivity of the Ag particles is also larger than the bulk Ag from the visible up to $1\ \mu\text{m}$. At longer wavelengths, the bulk has high metallic conductivity while the Ag particles tend towards an insulator in the DC limit, as shown in Fig. 4.5.

The anomalous dispersion is a well-known physical phenomenon in many intervals of the entire electromagnetic spectrum of the electromagnetic radiation - solid interactions. At those certain frequency intervals, the index of refraction or the real part of the dielectric constant decreases as the frequency goes up, contrary to the normal dispersion. The ionic lattice vibrations in the infrared is one example of the commonly known anomalous dispersions. When this dispersion occurs, there is a peak in the imaginary part of the dielectric constant accompanied by an oscillatory real part of the dielectric constant. This phenomenon can be understood using the Lorentzian oscillator model which involves a scattering time τ and a natural frequency ω_0 corresponding to a restoring force. The electronic contribution to the anomalous dispersion can also be treated in a similar fashion. Although free electrons do not absorb the visible or infrared radiation due a lack of restoring force on them, a restoring force can be created if they become bounded by particle boundaries on which surface charges are accumulated at the excitation of light. (Note that the Drude model of free electron metals is simply the Lorentzian model with zero restoring force.)

Fig. 4.6 shows the real (ϵ_1) and imaginary (ϵ_2) parts of the dielectric constant and the quality

factor of the surface layer of the S-1 photocathode with no second microstructural unit and hence no absorption peak at $\approx 0.8\mu\text{m}$. The quality factor $Q = \epsilon_1/\epsilon_2 = 1 / \tan \delta$ is proportional to the ratio of energy stored versus the averaged energy loss per period of oscillation and δ is the loss angle. We can readily identify the oscillatory characteristics of ϵ_1 for an anomalous dispersion at $\lambda = 0.41\mu\text{m}$. Note that when photoabsorption occurs at this wavelength, the quality factor drops. This corresponds to a resonance, not occurring in the bulk Ag, due to the bound free electrons in the silver particle. The photon energy is absorbed to excite electrons in the Ag particles. In Fig. 4.7, we put in 2% of the second microstructural unit. We see an additional resonance at $\approx 0.8\mu\text{m}$, corresponding to the near infrared response of the S-1 photocathode. In Fig. 4.6 and 4.7 note the minima in quality factors and the similar oscillatory features of anomalous dispersion at the two distinct resonance wavelength intervals, 0.4 and 0.8 μm . The absorption at $\approx 0.8\mu\text{m}$ is thus a surface mode resonance, a cavity resonance due to the second microstructural unit (aggregated Ag particles). The peak near 0.41 μm is due to isolated silver particles. To make the second unit contribution to the resonance clearer, Fig. 4.8 demonstrates that as the fraction of the second unit increases from 0 to 0.2 the absorption in the infrared also goes up from ≈ 0 to $\approx 10\%$. This absorption peak due to the second unit can be called the second unit dielectric anomaly.

In parallel with the Ag-particle heterostructural system, Au and Cu also show similar behavior due to the aggregation of the small particles. Fig. 4.9 and 4.10 show the second unit effects on the optical absorptions of Au and Cu systems respectively. This calculation predicts a dielectric anomaly at $\approx 2.3\text{ eV}$ (0.53 μm) for the Au-particle system due to the isolated Au particles, close to the value measured by Yamaguchi et al. [26] which is $\approx 2.2\text{ eV}$ (0.56 μm). As for Cu, the dielectric anomaly occurs at $\approx 2.2\text{ eV}$ (0.56 μm). Note that this peak has been somewhat obscured by the interband transition which takes place at about 2eV for Cu. Nonetheless, the enhanced photoabsorptions in the infrared due to the second microstructural units are evident. The absorptions peak at $\approx 0.8\mu\text{m}$ for both Au and Cu whose particle volume fractions are 40%. At the same volume fraction, the second unit peak of Ag occurs at $\approx 0.6\mu\text{m}$ as

shown in Fig. 4.11 for an 100 Å thick layer of the singly sized Ag-particle suspension with diameter 50Å and 2% aggregation. In this figure, we see that, at constant fraction of the second unit, the increasing volume fraction of silver particles shifts the optical absorption into the infrared. Meanwhile, the peaks broaden and the peak intensities change with the increasing Ag volume fractions, as summarized in Table I.

Table I

Concentration Effects: An 100Å Thick Layer of 50Å Diameter Ag Particles in Vacuum

Volume Fraction P(%)	10	20	30	40	50	60
First Unit Peak Position ω_0 (μm)	0.35	0.37	0.37	0.38	0.41	0.43
n_{eff} at First Unit Peak Position	1.0	1.12	1.23	2.15	2.58	3.15
k_{eff} at First Unit Peak Position	0.67	1.54	1.89	3.71	4.19	4.65
First Unit Peak Intensity (%)	19	40	45	47	46	43
First Unit FWHM (eV) $\Delta\omega=1/\tau$	0.4	0.4	0.4	0.5	0.6	0.9
Scattering Time τ ($\times 10^{-15}$ sec)	1.65	1.65	1.65	1.32	1.10	0.73
2nd Unit Peak Position (μm)	x	0.45	0.52	0.62	0.76	0.98
2nd Unit Peak Intensity (%)	x	8.1	8.6	8.9	9.0	11.9
n_{eff} at 2nd Unit Peak Position	x	1.51	1.73	1.91	2.15	2.54
k_{eff} at 2nd Unit Peak Position	x	0.21	0.23	0.26	0.30	0.31

From Table I and Fig. 4.11, we see that when the Ag volume fraction is low the absorption due to the isolated Ag particles (first unit) is also low. As the volume fraction increases to above 40%, the scattering time reduces corresponding to line shape broadening. This is understandable since as the number of Ag particles increases, the inter-Ag-particle interactions become more prominent and the scattering rate (damping) of electrons in the particle thus increases. Note that according to the Eqn.(2.4), the scattering time of a single Ag particle 50 Å in diameter is $3.22 \times$

10^{-15} sec. The scattering rate for a collection of similar small particles has thus been increased by a factor of two to four depending on the volume fraction, a reflection of electron-electron interactions between the Ag particles. The peak intensity increases while the peak width (and hence the scattering time) remains pretty much constant as a function of the Ag volume fraction from 10% to 40%. This seems natural because more Ag particles should contribute to more photoabsorption if the damping of the bounded free electrons due to the inter-Ag-particle interactions are not important at low Ag concentration. Above 40%, the peak intensity decreases while the peak width (and hence the scattering rate) increases as the Ag volume fraction increases. This can be understood using the Lorentzian oscillator model for forced oscillations. At these higher concentrations, the optical absorption may not be a drastic function of concentration. However, since the resonance peak intensity is proportional to τ / ω_0 , [27] the intensity should weaken as the peak broadens while it should strengthen as the resonance has a red shift.

The reason for the red shift is the increase in the effective refraction index n_{eff} of the effective medium embedding the isolated and aggregated Ag particles, where $(n_{eff} + i k_{eff})^2 = \epsilon_{l,eff} + i \epsilon_{eff}$. Similar to the effect of increasing polarizability of metal particles by selecting a embedding dielectric (or semiconductor) matrix with larger dielectric constant ϵ_m , the increasing volume fraction p creates a more polarizable environment due to the larger refraction index n_{eff} . This will be further discussed later on. The respective values of n_{eff} and k_{eff} at the resonance wavelengths for the two units of microstructure are also listed in Table I. In any case, these two factors (lifetime τ & resonance frequency ω_0), together with the fact that the increasing volume fraction increases the optical cross-section, can interpret the overall variations in peak intensities and line shape near 0.41 and 0.8 μm in Fig. 4.11. As shown in the same figure for the second microstructural unit near 0.8 μm , there are also red shift and line broadening as a function of increasing volume fraction. These peak values are listed in Table I. Precise line widths are not easy to extract from the figure at 0.8 μm due to the weak peaks and therefore no attempt are made here to explain the intensity change as a function of Ag volume fraction. Similar host matrix

reflection effects have also been observed in the alkali metal particles embedded in alkali-halide matrices.[28]

Before going any further into other microstructural effects, let's digress to look at the plasma oscillation of the small Ag particle system. From Fig. 4.12.a & b, we see that the real part of the complex dielectric constant vanishes while the imaginary part is very small (or close to zero) at ≈ 3.74 eV (3315 Å). The optical energy loss function[29-30] $-\text{Im}\{1/\epsilon\} = \epsilon_2 / (\epsilon_1^2 + \epsilon_2^2)$ peaks at the same energy. This function should show a δ -function type behavior at the volume plasma frequency.[15-29] For bulk Ag, it occurs at ≈ 3.9 eV (3200 Å). We thus see that the plasma oscillation for the small Ag particles takes place at lower frequency than the bulk silver does. In any event, the dip at ≈ 3.8 eV that exists in the optical absorption curve as well as the spectral response (quantum yield) curve of the small Ag particle system represents the plasmon loss. At plasma frequency, the transmittance should show a maximum while the reflectance a minimum. This is shown in Fig. 4.3. For surface plasma oscillation, it is believed that the surface optical loss function, $-\text{Im}\{1/(\epsilon + 1)\} = \epsilon_2 / [(\epsilon_1 + 1)^2 + \epsilon_2^2]$, should also show a δ -function type behavior at the surface plasma frequency.[15] This occurs at ≈ 3.62 eV (3425 Å) for both bulk Ag and Ag-particle suspension. From Fig. 4.3, it is found that the transmittance maximum and reflectance minimum occur at ≈ 3.74 eV for the S-1 surface. This leads us to believe that the volume plasmon loss in the photoelectric quantum yield, as will be shown later in the following section, could be responsible for the minimum in the spectral response of the S-1 photocathode at 3.8 eV.

Now, let's turn to the particle size effects on the optical properties of composites. Fig. 4.13.a gives a 3-D plot of the optical absorption of the S-1 surface whose Ag particle size ranges from 20 to 90 Å. It is seen that the second unit peaks are less conspicuous at smaller particle size for the same amount of second units. In other words, at bigger particle size, the optical absorption peak at around 0.8 μm sharpens for constant fraction of particle aggregations. This seems reasonable since the scattering rate at smaller particle size is higher which leads to the broadened

line shape. The size effect on the line shape broadening also comes up in the first unit absorption peak. This peak at 0.4 μm broadens as the particle size decreases, though it also intensifies. The weakening of the first unit peak at increasing particle size can be explained as follows.

As discussed previously, the dielectric anomaly is characteristic of bounded free electrons in small metal particles, when particles become bigger, the free electrons start losing their bound nature which leads to less scattering at particle boundaries. The resonance peak width therefore decreases. In the mean time, the peak intensity drops because, at constant volume fraction of Ag, the number density of the Ag particles decreases with increasing particle size. The contribution of bounded free electrons to the resonance is thus reduced, giving rise to lower peak intensity. To get a clearer picture of the change of the line shape due to the varying particle size, we give in Fig. 4.13.b a 2-D plot revealing the variations in resonance frequencies, peak widths and intensities and scattering times. These results are summarized below in the Table II.

Table II

Size Effects: An 100Å Thick Layer of 50% Ag Particles in Vacuum with 2% 2nd Unit

Particle Diameter (Å)	20	40	90	500
First Unit Peak Position ω_0 (μm)	0.41	0.41	0.41	0.40
First Unit Peak Intensity (%)	49	48	40	30
First Unit FWHM (eV) $\Delta\omega=1/\tau$	0.9	0.7	0.5	0.4
Scattering Time τ ($\times 10^{-15}$ sec)	0.73	0.94	1.32	1.65
2nd Unit Peak Position (μm)	x	0.70	0.80	0.80
2nd Unit Peak Intensity (%)	x	8.9	9.5	9.8

Finally, let's look at the overall optical properties of the whole S-1 photocathode with a surface layer covering a base layer. It is well known that the absorption curve is qualitatively different from the photoelectric quantum yield (PQY) curve.[2] Because of the inelastic scattering of the photoelectrons in the material, only the surface layer is responsible for the PQY. The

optical absorption, on the other hand, are due to both the surface and base layers, although a large fraction of the photoexcited electrons in the base layer may not be able to escape into the vacuum and be collected as the photoelectrons.

In Fig. 4.14, taking the multiple reflection of light into account, we show the absorptance of a multilayered structure of vacuum / surface layer / base layer / glass substrate. Again, the surface layer is 100Å thick with Ag-particle 50 Å in diameter, 50% volume fraction and 2% of aggregation. This ensemble of Ag particles is embedded in a host medium of unitary dielectric constant. The base layer is 300Å thick with 50% volume fraction and 30% of aggregation of Ag particles embedded in cesium oxide of dielectric constant of 4. The particle size in the base layer is larger than the surface layer and ranges from ≈ 100 Å to ≈ 1000 Å.[12,13] As mentioned previously, the particle size distribution in this layer follows the γ -type distribution function with mode radius 700Å and g factor ≈ 4 . The absorptance curve of the composite agrees qualitatively with the experimental results shown in Sommer's book.[2] Fig. 4.14 also contains the absorption of individual layers for comparison. From the line shape and peak positions, we can infer that the photoelectric yield (spectral response) of the S-1 photocathode must be primarily determined by the surface layer while the optical absorption by the base layer. This statement coincides with Sommer's interpretation: the optical absorption characteristics of the Ag-Cs₂O composite was due to the constant absorption of silver particles in the visible and in the infrared.

We have shown the microstructural effects on the optical properties of the S-1 photocathodes so far. These structural parameters are the Ag-particle size and its distribution, the volume fraction, the percentage of the aggregation and the embedding host matrix. Based upon these calculations, we can now pursue the calculation of PQY of the S-1 to interpret the experimental results theoretically.

IV. Numerical Results of Photoelectric Quantum Yields

In this section, we will present the numerical results of the PQY of the S-1 photocathode

based on the multiple-step model of the photoemission described in Section II and the extended DEMA of the optical absorption described in Section III. We will demonstrate the microstructural effects on the PQY and evidence the precision of our calculation. In this work, we take the multiple elastic scattering of photoexcited electrons at the Ag particle boundary into consideration. As described in Section II, the mean free path of the photoexcited electrons in the Ag is $\approx 1000\text{\AA}$ at the cut-off (threshold) wavelength (1.1 eV or $1.1\text{ }\mu\text{m}$) of the S-1 photocathode. For a surface layer with particle size of 50\AA , the inclusion of the geometric factor γ (Eqn. 4.10) due to the multiple elastic scattering of electrons in the particles makes the PQY close to 20 times larger than that excluding γ . Interestingly enough, the number of multiple elastic scattering of electrons in a particle of 50\AA in diameter is roughly $1000\text{\AA} : 50\text{\AA}$, which makes a factor of 20 as well. Fig. 4.15 exhibits this enhancement factor. The consideration of the geometric factor leads to the results close to the experimental data.[6] In the meantime, Fig. 4.16 reveals the Ag-particle size effects on the PQY. Since the number of multiple elastic scattering of an electron in the particle is larger when the particle is smaller, the probability for a photoexcited electron to escape into the vacuum and be collected is therefore also larger. This phenomenon was first observed experimentally by Wu[12,13] through the electron microscopic studies and the photoelectric measurements. It is worth stressing here that the PQY enhancement at higher photon energy (the peak near $0.41\text{ }\mu\text{m}$), where the photoelectron mean free path is short and the geometric enhancement factor therefore less important, is due to the higher photoabsorption of smaller particles, the larger transmission coefficient and the higher escape probability (larger escape cone or θ_c) of the photoelectrons. On the other hand, the enhancement at the lower photon energy end is due to the long mean free path of the photoexcited electrons.

From Eqn.(4.12)-(4.14), we can see the individual contributions of the surface and base layers to the PQY of the S-1 photocathode. Fig. 4.17 shows the PQY of these two layers separately and the overall PQY. The corresponding optical absorption is shown in Fig. 4.14. It is found that the surface layer does contribute to the most part of the photoyield. The different

features of the optical absorption curve and the spectral response curve are thus accounted for: the surface layer determines the photoelectric yield while the base layer the photoabsorption of the S-1. Before further showing the microstructural effects on the quantum yield of the S-1 photocathode, it is worth repeating here that the minima at about 3.8eV for all PQY curves given in this section represent the plasmon loss as discussed in the previous section.

The contribution of the second microstructural unit to the PQY is given in Fig. 4.18. We see that as the second unit disappears, the PQY in the near infrared diminishes accordingly. It has been reported by Asao[2,20] that the increasing amount of silver deposited escalates the photoelectric current at $h\nu \approx 0.7 \mu\text{m}$ which in our model is attributed to the aggregation of the Ag particles. Fig. 4.19 reveals the Ag volume fraction effects on the PQY. As is obvious, as the Ag volume fraction steps up from 40% , 50% to 60%, the PQY peak in the near infrared shifts toward longer threshold wavelength although the peak intensity near $0.8 \mu\text{m}$ is lower for larger volume fraction. This trend is somewhat different from the optical absorption property exhibited in Fig. 4.11 given in previous section where the red shift and the increasing of the second unit peak intensity occur simultaneously.

The threshold wavelength is determined by the Schottky barrier height at the interface between silver and cesium oxide. Compared with that at high photon energy, the escape probability of photoexcited electrons near threshold is smaller since they carry less kinetic energy to overcome the energy barrier. This becomes a limiting factor of shifting the threshold wavelength into the infrared unless the Schottky barrier width can be narrowed by impurity doping so that the tunneling of photoexcited electrons from the metal particle into vacuum become possible at kinetic energy lower than the Schottky barrier height. Otherwise, some other materials providing lower Schottky barrier height will be needed for a photocathode with cut-off wavelength greater than that ($1.1 \mu\text{m}$) of the S-1 photocathode. Regarding the Schottky barriers confronted here, another substitute for such composite system is a metal that forms ohmic contact with the semiconductor matrix. For this case, the threshold would become $E_c - E_F$. One can then shift the

threshold unlimitedly by doping the semiconductor to bring E_F as close to E_c as one desires. The limitation now becomes the noise level that may be incurred due to the impurity doping of the semiconductor, as in an extrinsic semiconductor photodetector.

Combining all the microstructural parameters, we can reproduce many other PQY curves representing the S-1 surface of various microstructures. The concurrence of all the microstructural effects can therefore be possibly employed to explain certain PQY curves measured experimental.[3,5,6] For example, in processing the S-1 photocathode, the additional silver deposition was found to increase the PQY in the near infrared although it shortens the threshold wavelength. As the additional silver is evaporated, both the amount of Ag-particle aggregation and the particle size should increase.[2,20] At the same time, the effective volume fraction of the silver particle should also go up. From the theoretical results just presented, together with the fact that the energy barrier of the small silver particle may vary for different silvering processes which will therefore affect the threshold wavelength, the increasing Ag volume fraction and amount of aggregated Ag particles may well explain the experimental observation. If the energy barrier heights of the additionally deposited Ag particles are not as low as 1.1 eV (1.1 μm), the cut-off wavelength will certainly shorten although the optical absorption of the surface layer in the infrared may still go up due to the formation of the second microstructural unit. The work function of the pure Ag is about 4.9 eV which, upon cesiation, lowers to 1.1 eV. As stated before, the Cs_{11}O_3 coating the Ag particles were just to lower the Ag work function and did not affect the dielectric constants.

The enhancements of photoabsorption and photoemission have to occur simultaneously to give enhanced photoyield. For too large particles the photoabsorption cross-section and photoelectric yield are low as compared with smaller particles. However, though smaller particles may seem more desirable for better photoelectric efficiency, quantum size effects may come into play if the size is too small. The particle may then lose its metallic nature and our classical electrodynamic theory fails to properly describe its properties. As yet, it is not well-understood as

to how work functions change with particle size. The end values are the ionization energy of atoms for the atomic state and the work function of materials for the bulk state. The former is larger than the latter while that of a small particle can be lower than both cases.[1-4, Chapter III] But there is no conclusive results as to how it varies as particle sizes and how small a particle can be which still retains its metallic character. For reasonable photoyield, an optimal particle size may exist as Wu and Bates,Jr. have suggested 30-50Å particles as most sensitive to incident photon at 800nm.

As a matter of fact, our studies have shown that particle size is not very critical in enhancing photoabsorption especially for particles larger than 20Å, according to the classical theory. Recently, there have been studies on the particle shape effects.[8,31-33] It is found that spheroidal or ellipsoidal particles with smaller minor to major axial ratio show stronger absorptions. Radiation dampings at the tips of these elongated particles are employed to explain these enhancements. This shape effect has already been attacked in a more classic work[34] with similar conclusion. In Fig. 20, we include the work by Skillman and Berry[35] on small silver particles in gelatine. The particle sizes and axial ratios are shown below the figure. A calculation based on Sheng's electric dipole approximation of effective medium theory[8] is given in Fig. 4.21 for silver particles in vacuum with spherical shape of 50Å in diameter ($a:b=1:1$) and spheroidal shape with $a=200\text{Å}$ and $a:b=3:1$. The results agree to each other at least qualitatively.

V. Conclusions and Material Designing Rules

In conclusion, we have proposed a multiple-step model of photoemission that takes the multiple elastic scattering of the photoelectrons in the Ag particles into consideration. Incorporated with the extended dynamic effective medium approximation, this model allows us to calculate the PQY curves for various types of microstructures which represent different stages of processing. Our calculations are done in a more or less precise way since no adjusting factor has been involved. The numerical results seem to agree well with the experimental data. The main features

of the PQY and the absorptance of the S-1 surface can be interpreted quite successfully.

Based upon the success of this theoretical survey, we can infer the material-design rules for a heterogeneous composite system. As demonstrated in Section III, it is found that copper and gold particles also show similar properties such as the anomalous dispersion due to the bounded free electrons as well as the aggregation effects on the optical absorption in the near infrared. We can tailor desired optical properties through selecting adequate microstructural parameters. These parameters includes the types of metal particles and their volume fractions, particle sizes, and extent of aggregations of these particles. The semiconductor selected as host matrix also has significant influence on enhancing the photoabsorption of these small metal particles.

The larger dielectric constants of semiconductors imply higher polarizabilities which suggest that it requires less energy to excite a resonance. Therefore, there is a red shift as the embedding matrix is replaced with a higher dielectric constant semiconductor for the same species of metal particles. Fig. 4.22 indicates this host matrix effect. Besides the significant photoabsorption in the infrared, photoelectrons have to be efficiently collected in some way for photon detection applications. Tunneling of electrons between metal particles is not an efficient way of electron transport compared with the conduction band transport. For fast response we need to provide a collector for electrons escaping from the metal particles to transport within and be collected therein. The energy barriers for electrons to escape depend on the type of semiconductor chosen. High dielectric constant materials such as Si, GaAs and CuInSe₂ etc. are good candidate for these purposes. What is crucial to the rules of materials selection for proper host matrix now is the technological accessibility to fabricate the random composites of various small metal particles in semiconductors without the involved metal-semiconductor compound formations and interdiffusions.

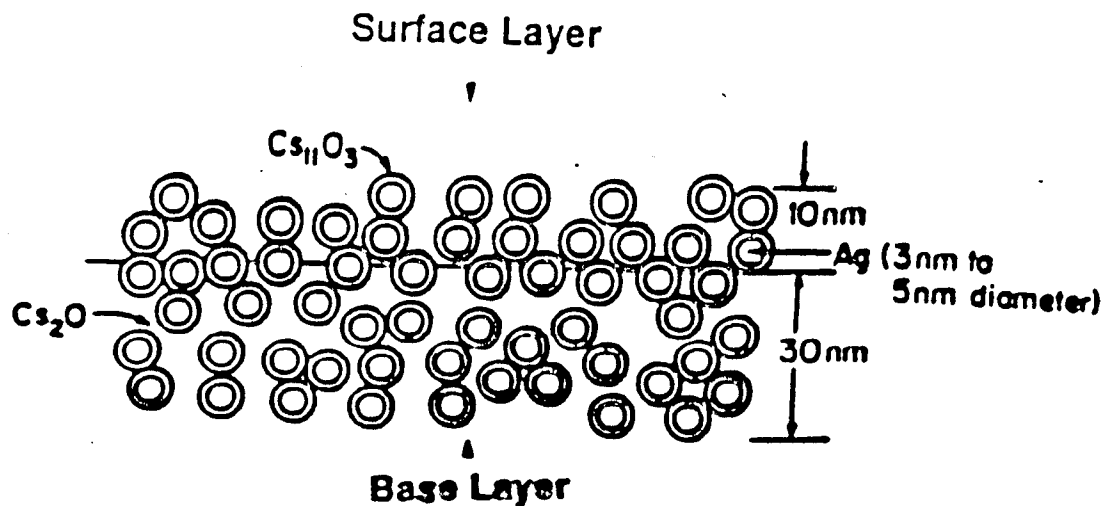


Fig. 4a The microstructure of the S-1 photocathode composed of a surface layer residing on a base layer.

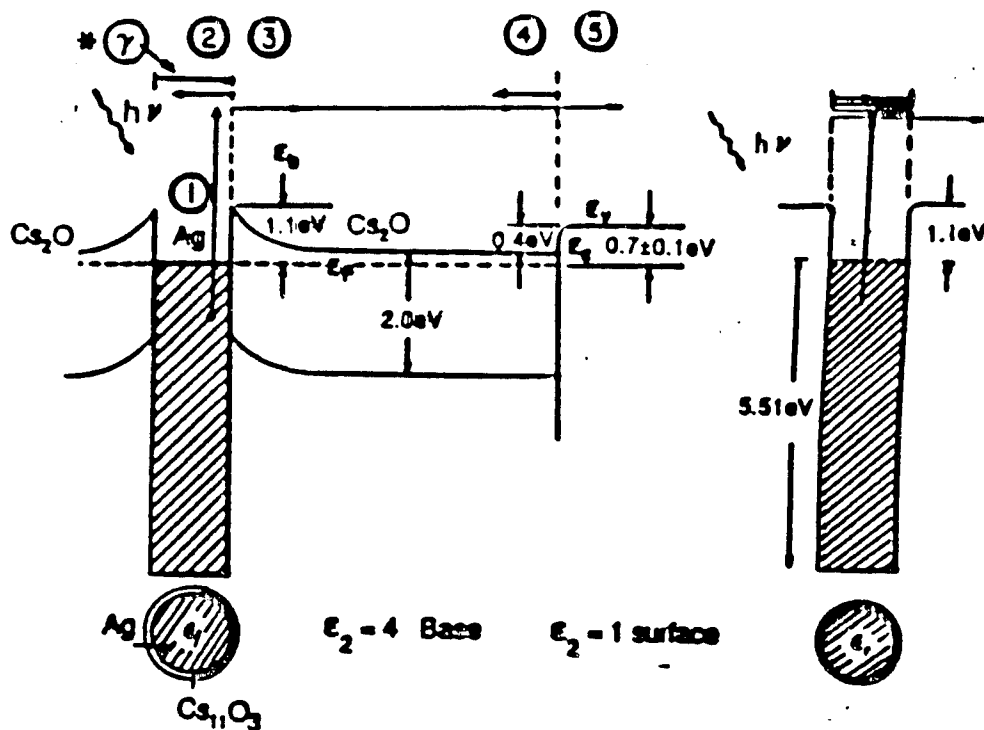


Fig. 4b The energy band diagram of the separated layers of the S-1 photocathode. E_F = Fermi level. E_b = Schottky barrier height. E_v = vacuum level, E_c = bottom of conduction band of Cs_2O . * γ is the enhancement factor due to multiple scattering.

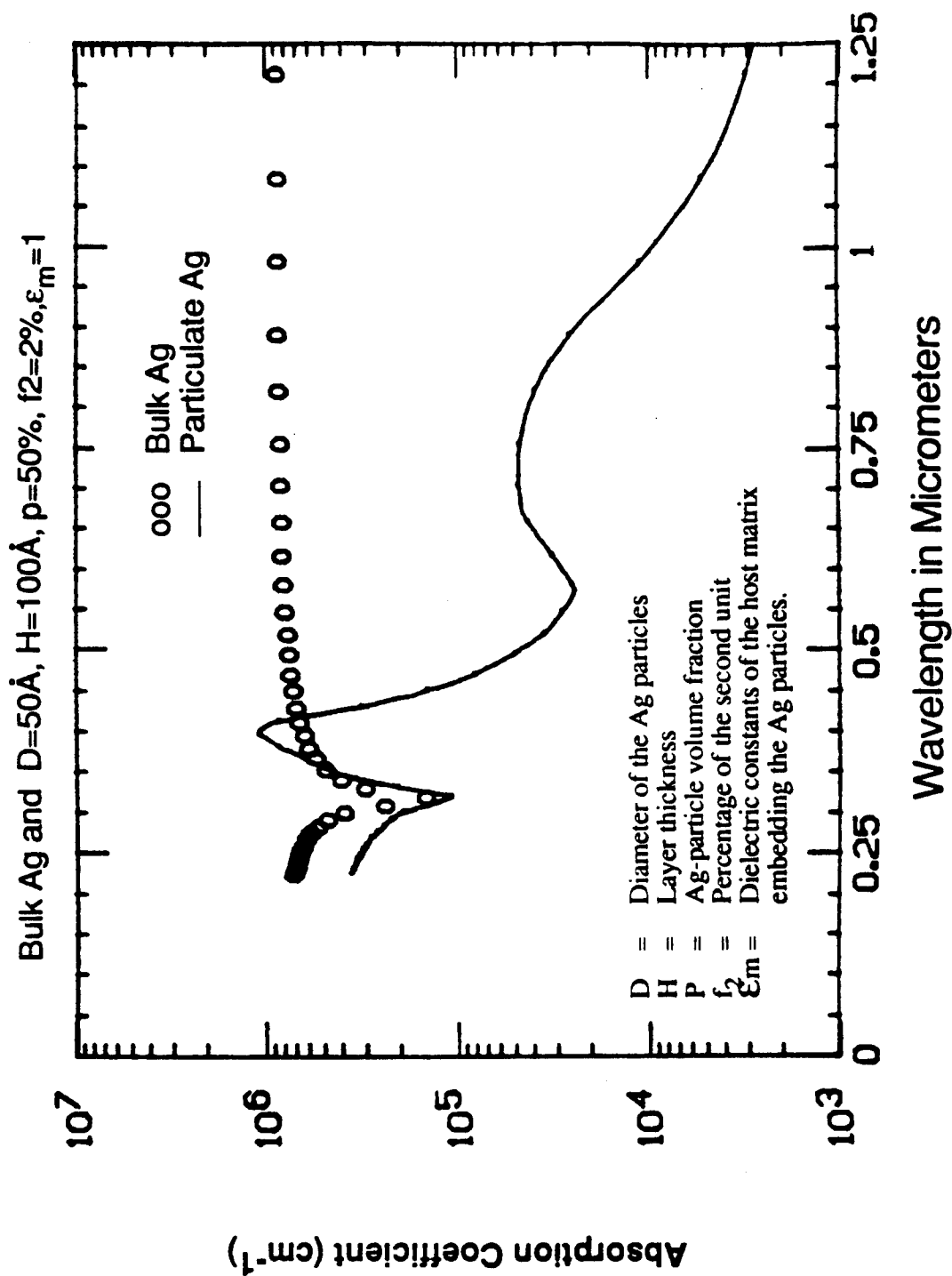


Fig. 4.2 Optical absorption coefficient of a surface layer of Ag particle suspension compared to the bulk Ag.

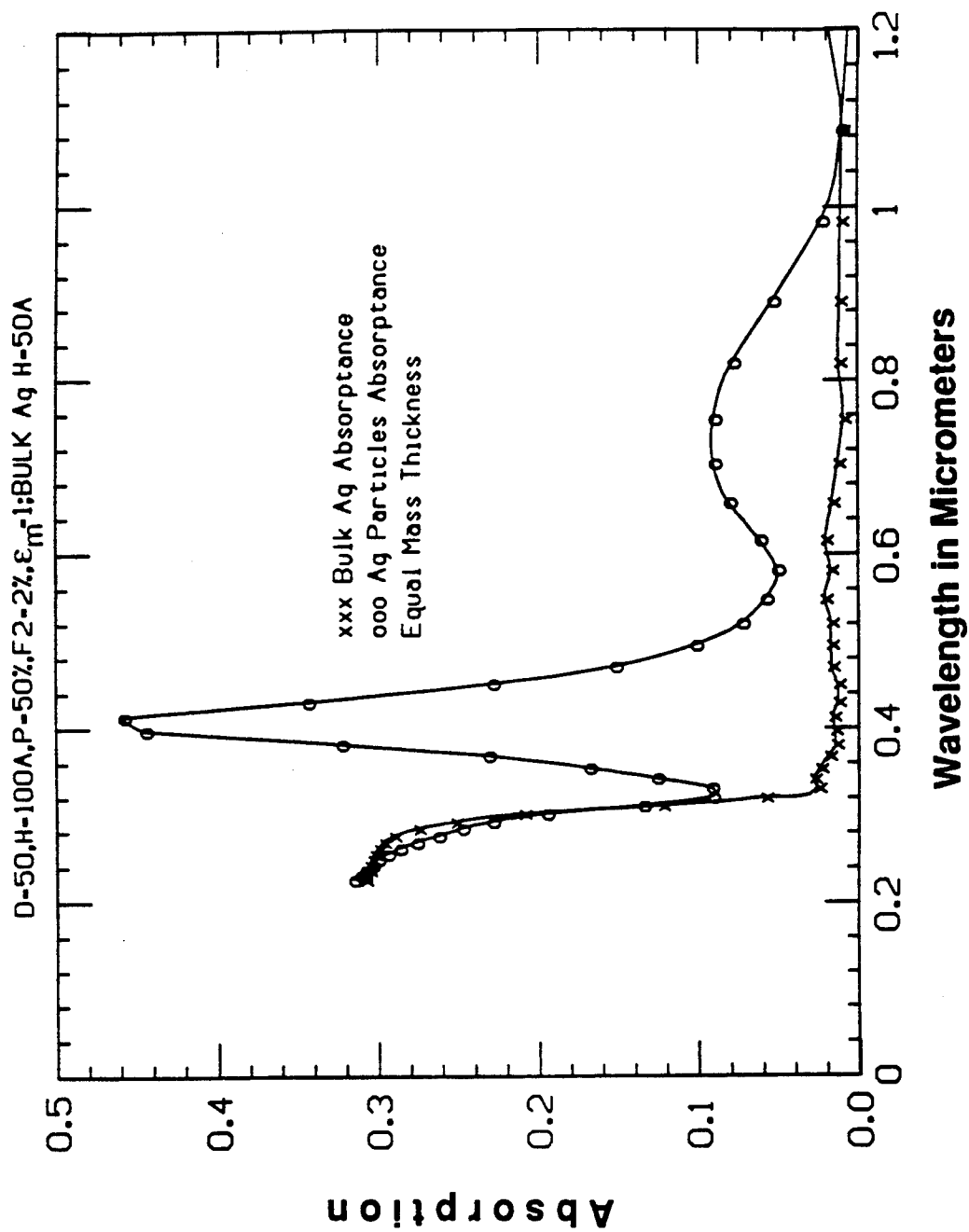


Fig. 4.3 Comparison of optical absorption of the same Ag particles and bulk Ag with absorption coefficients given in Fig. 2.

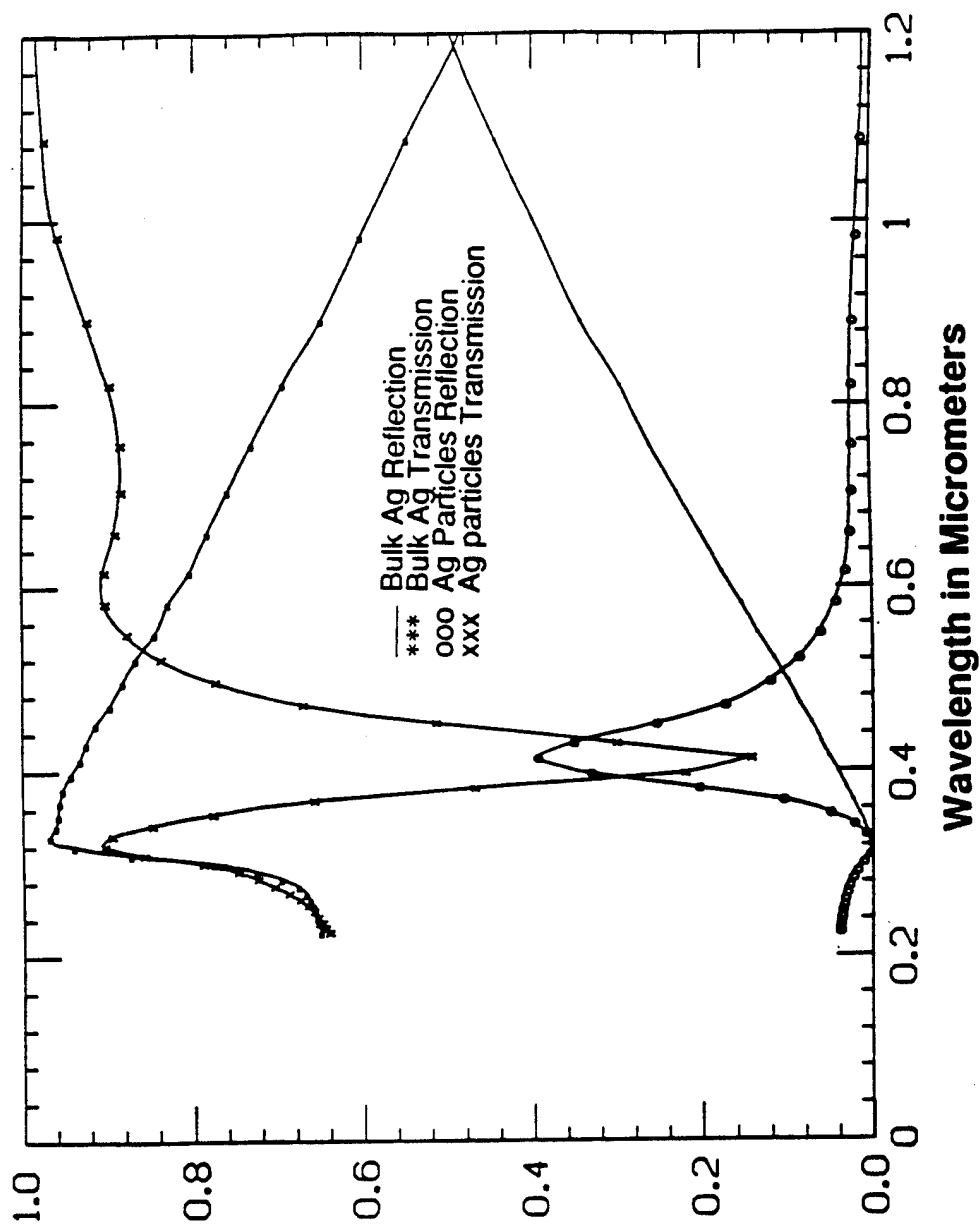


Fig. 4.4 Comparison between the R and T of particulate and bulk Ag of the same mass thickness. Parameters are the same as Fig. 4.2.

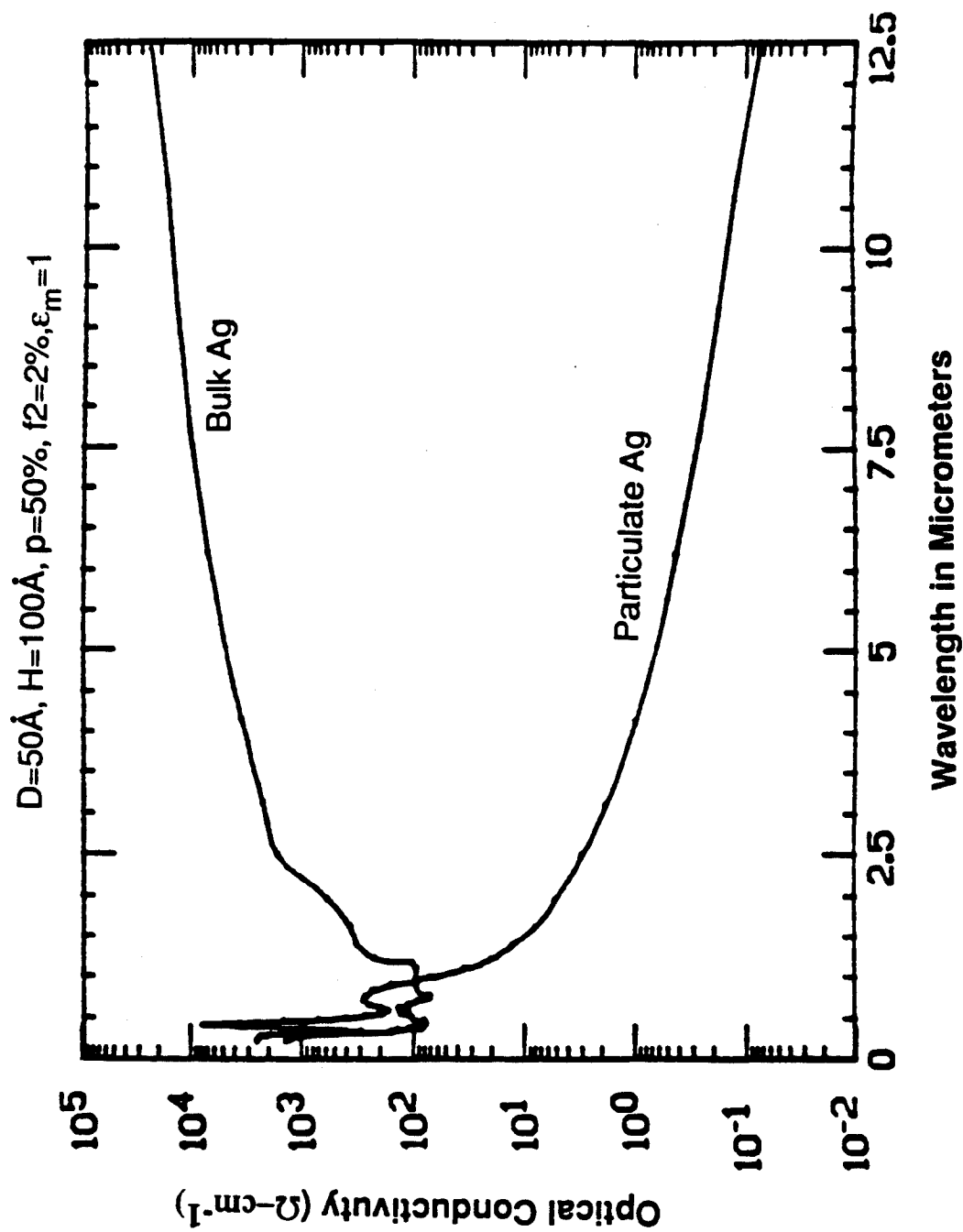


Fig. 4.5 Comparison between the optical conductivities of particulate and bulk Ag at various frequency regions.

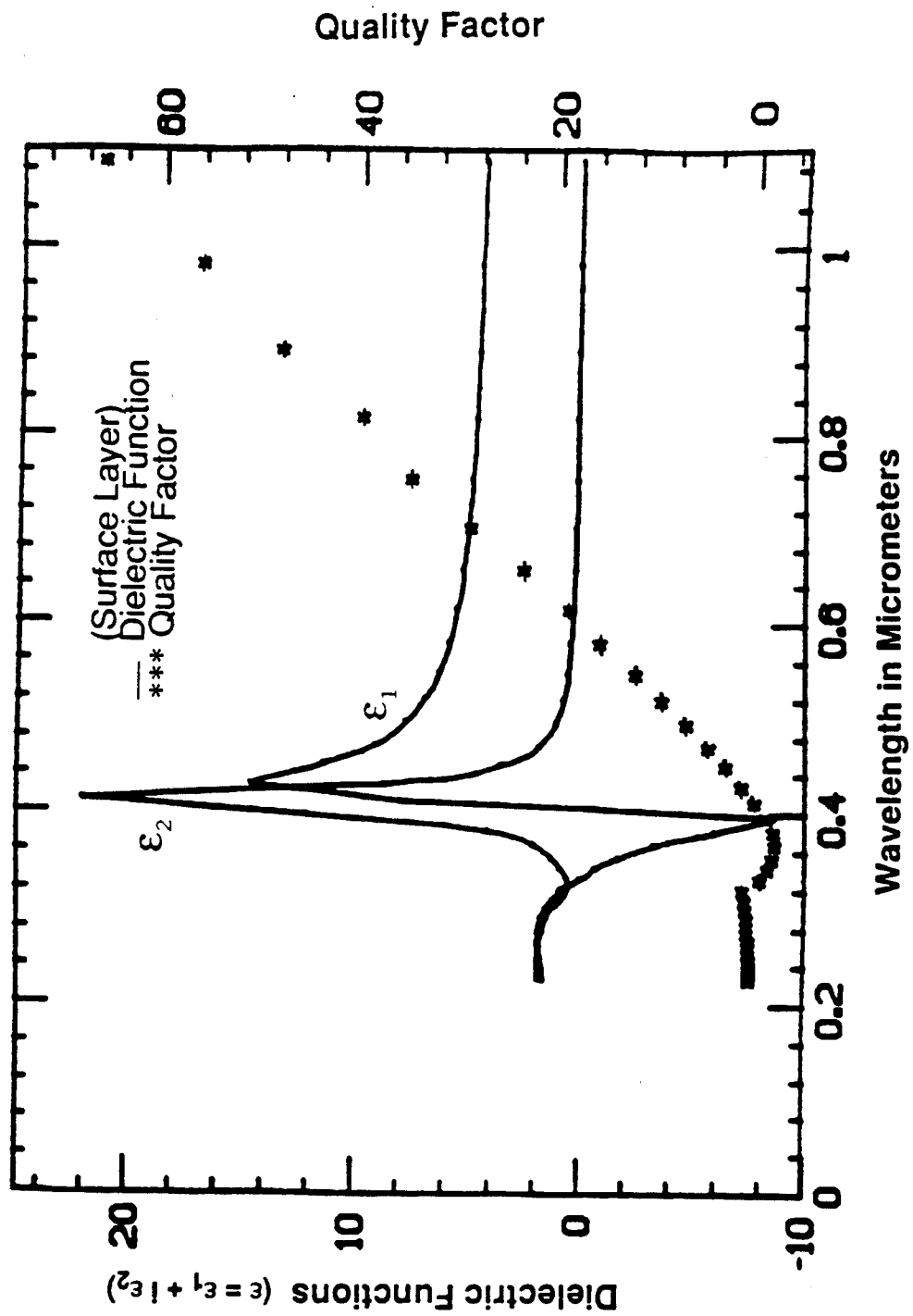


Fig.4.6 The Q-factor and the real part and the imaginary part of the complex effective dielectric constant corresponding to Figs. 4.2-4, except that there is no second unit included in this layer.

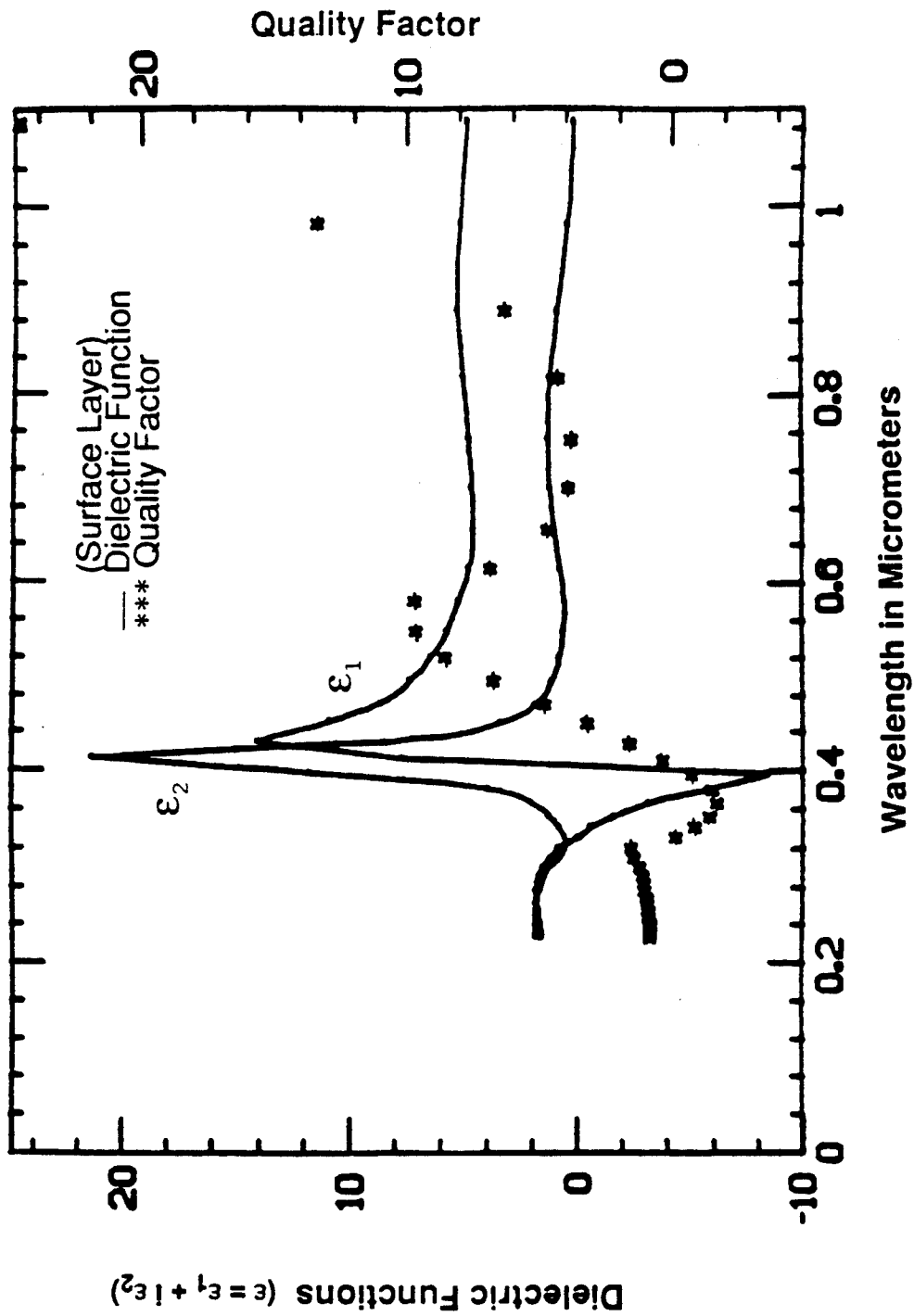


Fig. 4.7 Similar to Fig. 4.6, except that there are 2% second unit which leads to two dielectric anomalies at 0.4 and 0.8 μm .

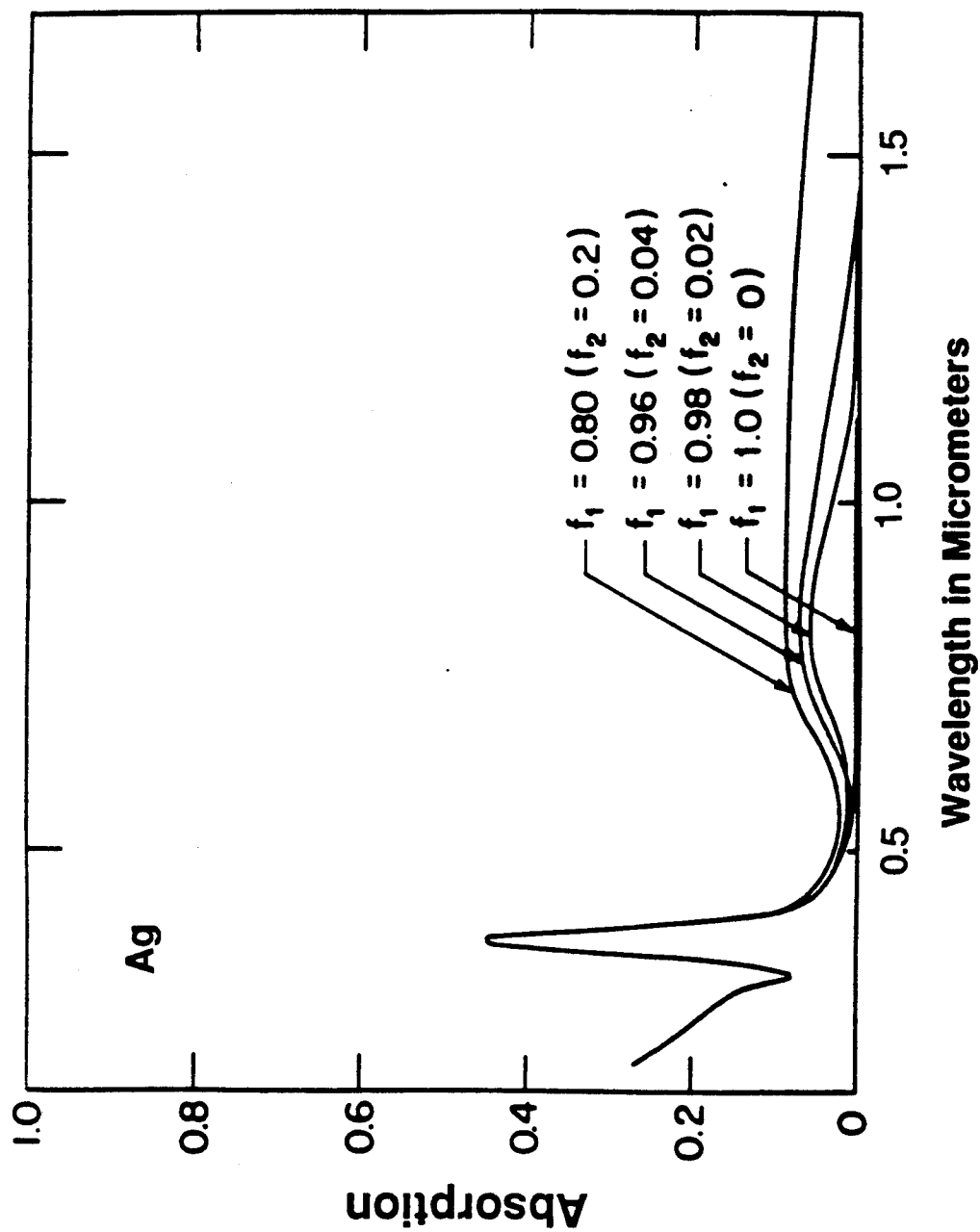


Fig. 4.8 The second unit effect on the absorbance of the S-1 surface with microstructural parameters $D = 50\text{\AA}$, $H = 100\text{\AA}$, $P = 50\%$, $f_2 = 0, 2, 4, 20\%$ and $\epsilon_m = 1$.

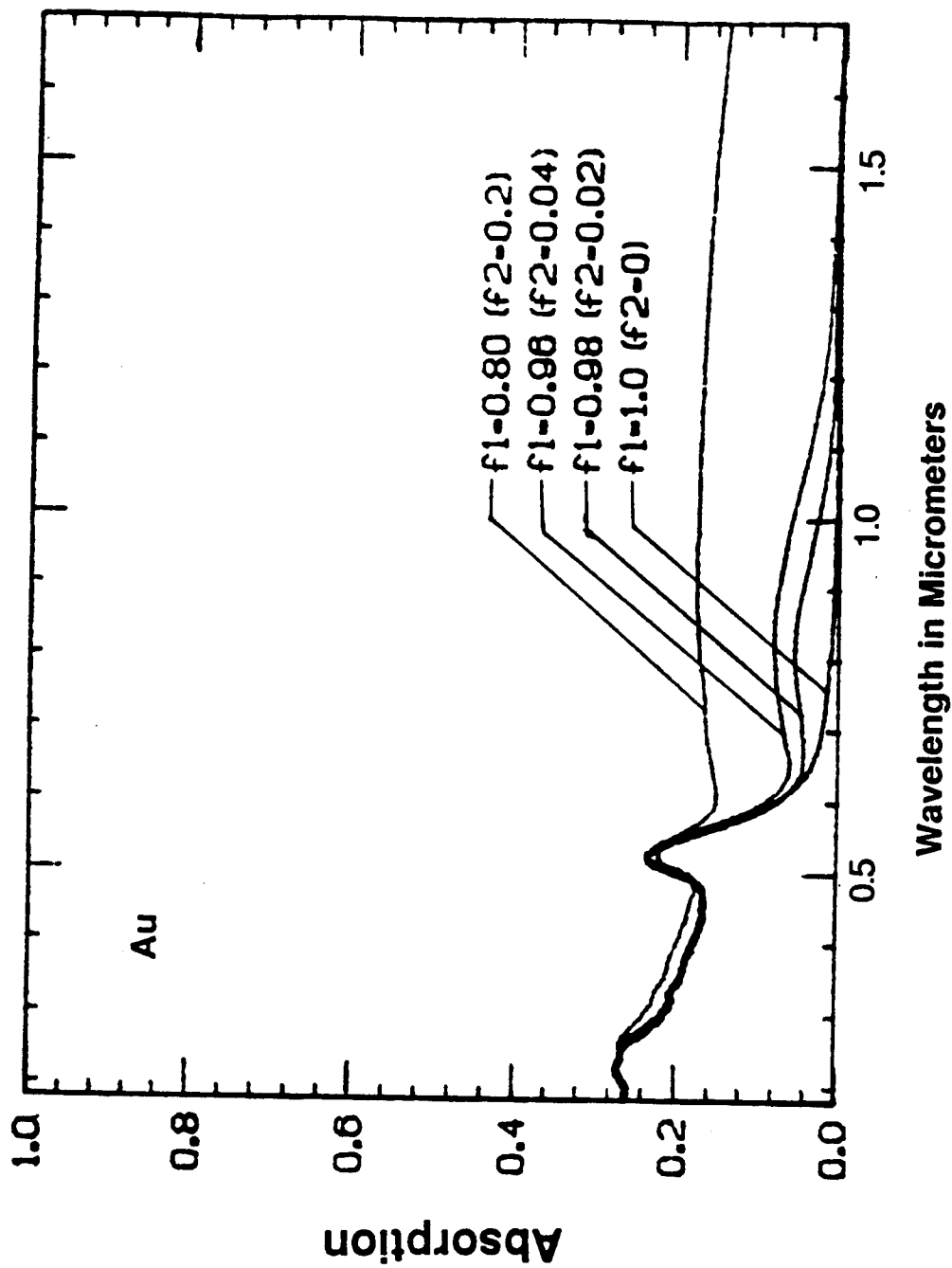


Fig. 4.9 Absorption of Au-particle suspension. $D=50\text{\AA}$, $H = 1000\text{\AA}$, $P = 40\%$, $f_2 = 0, 2, 4, 20\%$ and $\epsilon_m = 1$. The increasing absorption above 2 eV is due to the interband transitions.

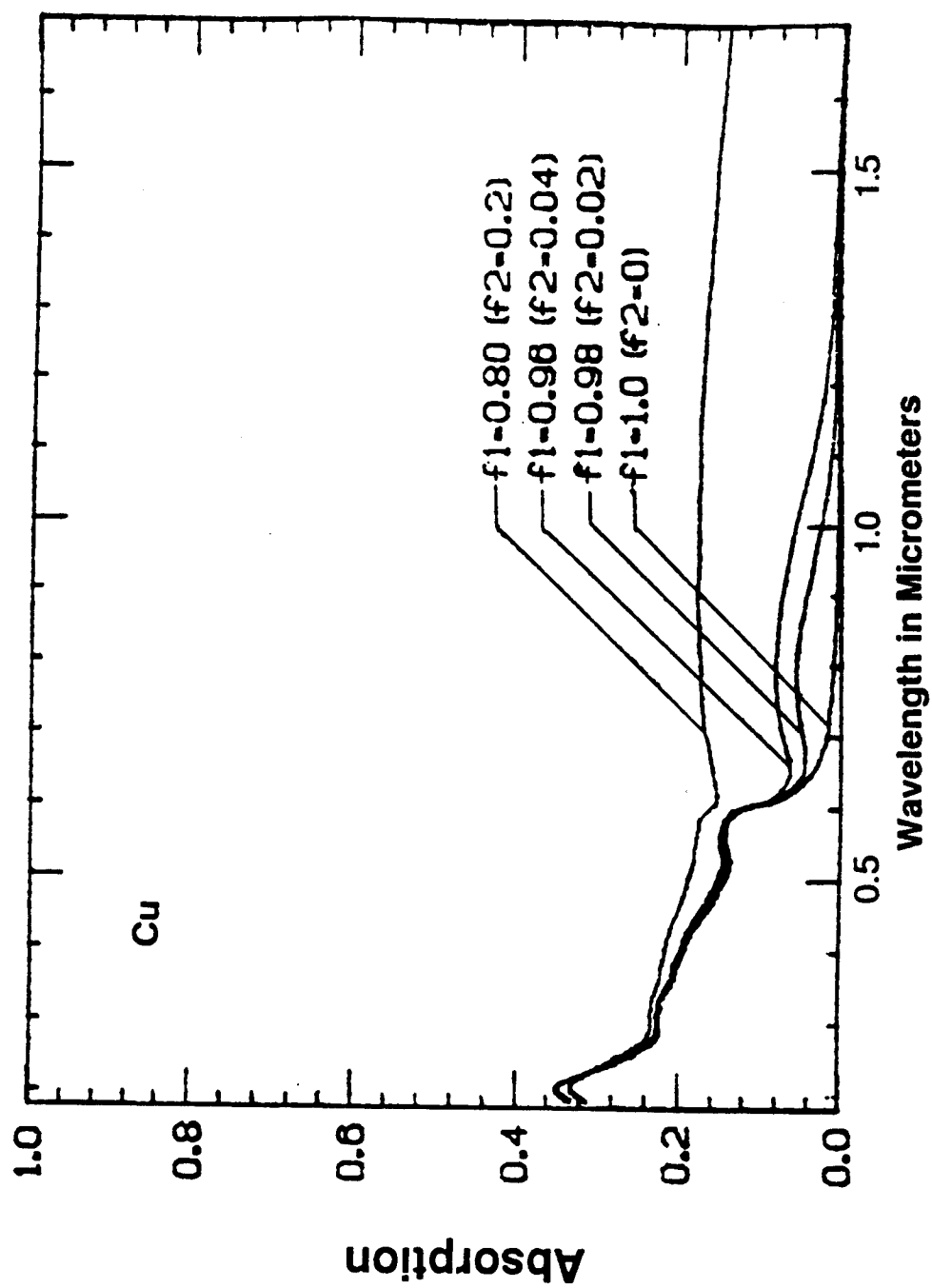


Fig. 4.10 Absorption of Cu-particle suspension. $D=50\text{\AA}$, $H = 1000\text{\AA}$, $P = 40\%$, $f_2 = 0, 2, 4, 20\%$ and $\epsilon_m = 1$. Note the increasing absorption above 2 eV is due to the interband transitions.

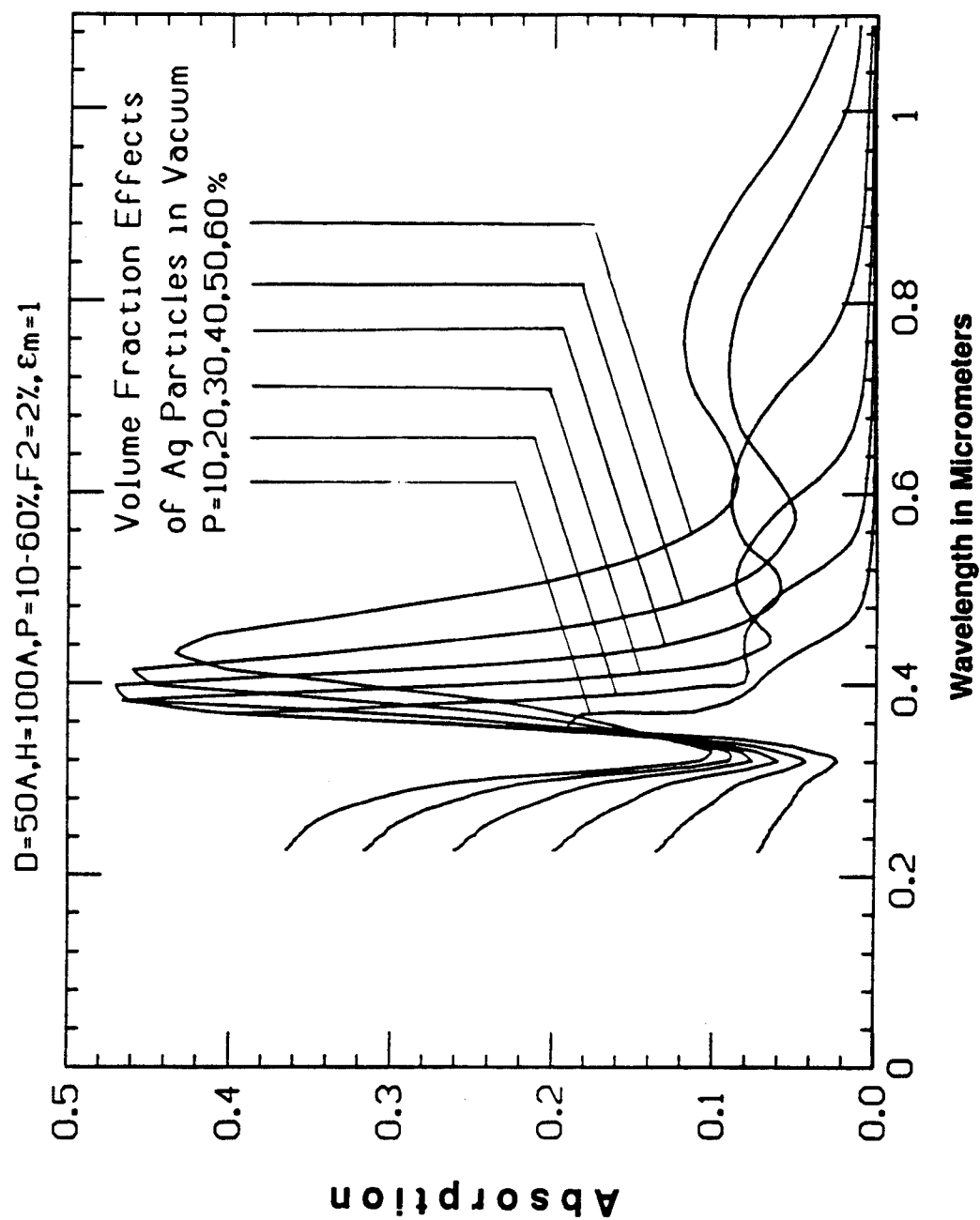
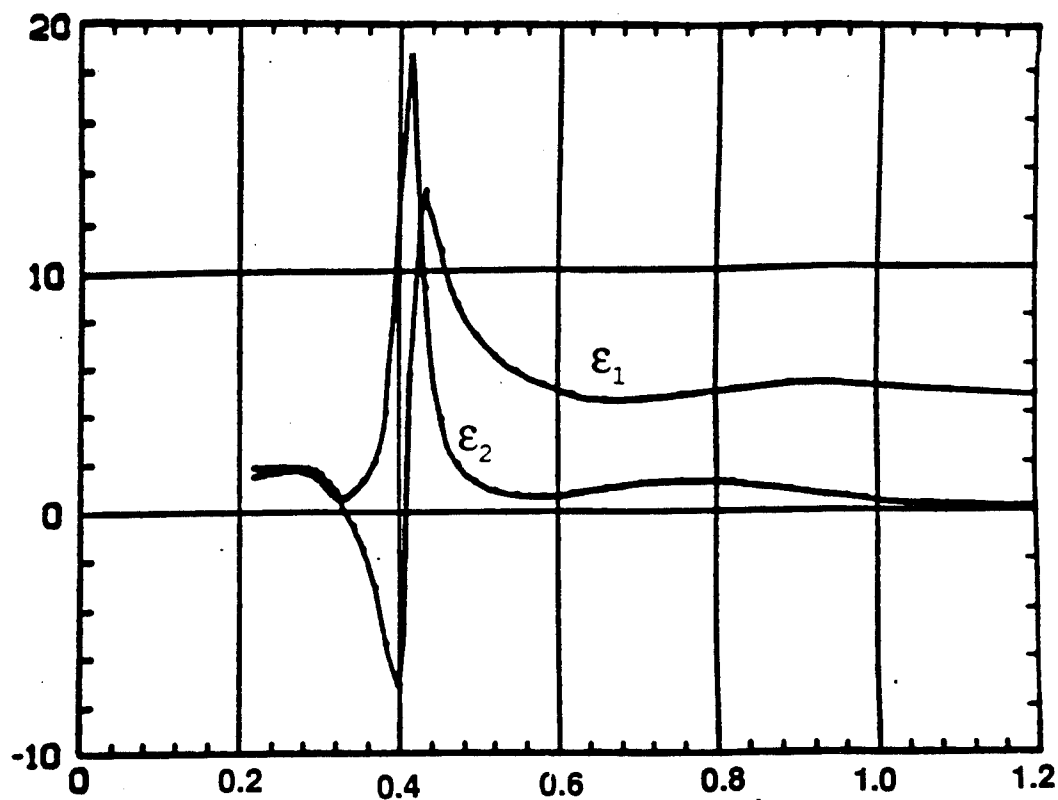


Fig. 4.11 Ag volume fraction effects on the optical absorption of the S-1 surface. $D = 50\text{\AA}$, $H = 100\text{\AA}$, $P = 10, 20, 30, 40, 50$ and 60% , $f_2 = 2\%$, $\epsilon_m = 1$.

$D=50\text{\AA}$, $H=100\text{\AA}$, $p=50\%$, $f_2=2\%$, $\epsilon_m=1$

DIELECTRIC CONSTANTS

(a)



LOSS FUNCTION

(b)

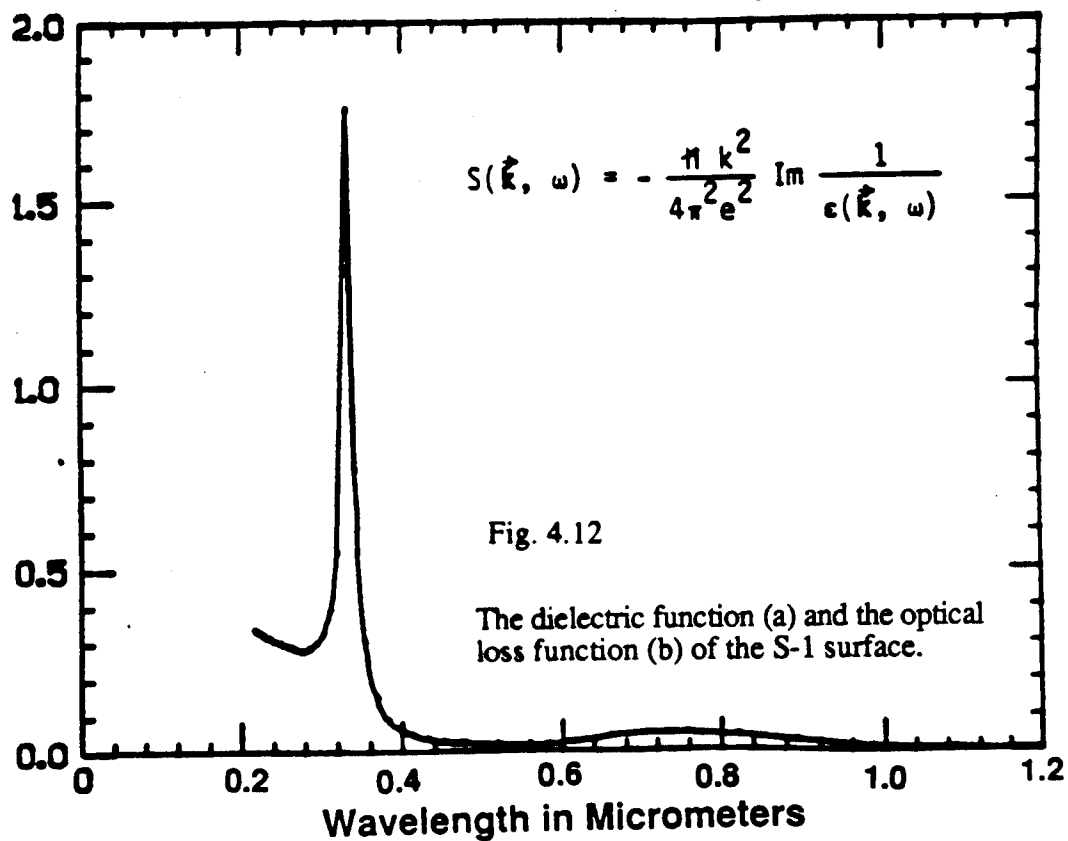


Fig. 4.12

The dielectric function (a) and the optical loss function (b) of the S-1 surface.

Ag in Vacuum ($\epsilon=1$)

$H=100\text{\AA}$, $p=50\%$, $f_2=2\%$, $\epsilon_m=1$

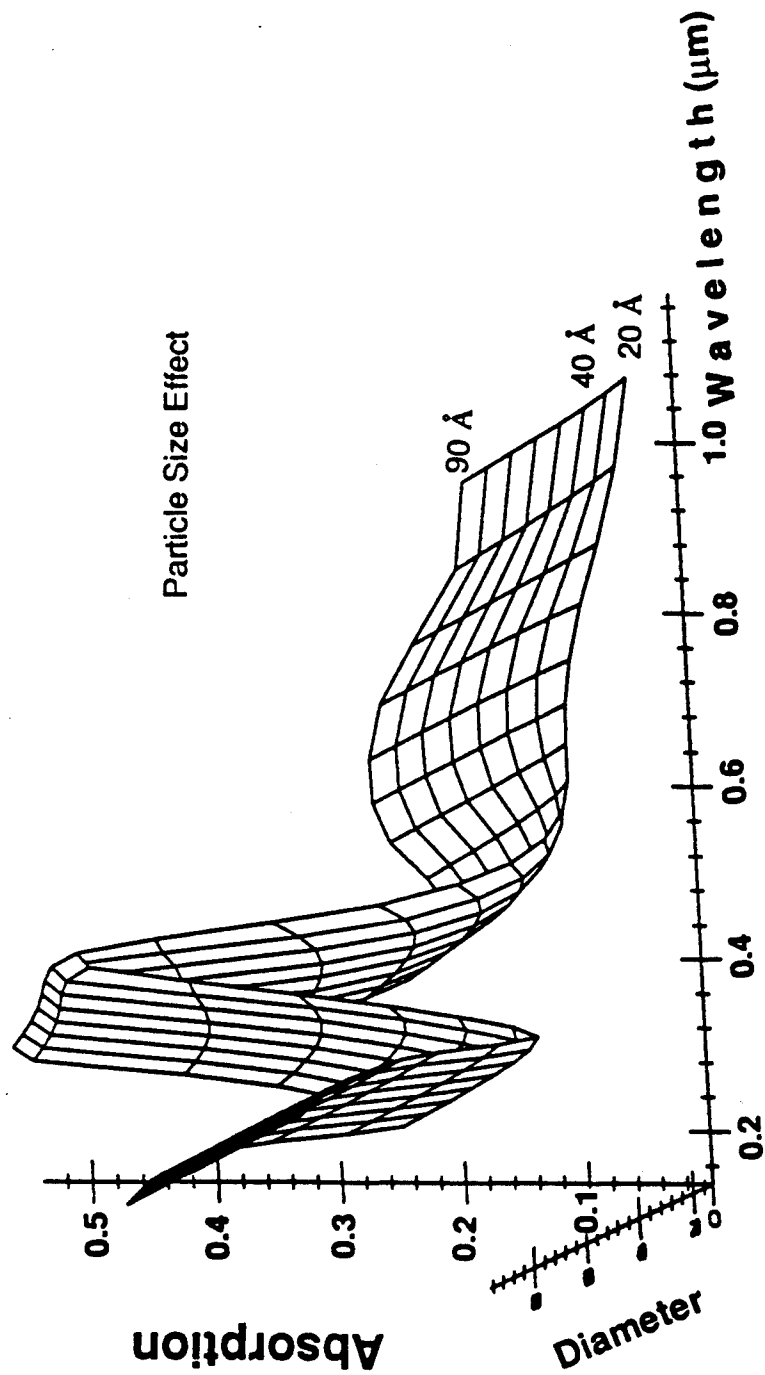


Fig. 4.13 Ag particle size effect on the S-1 surface. (a) 3-D plot

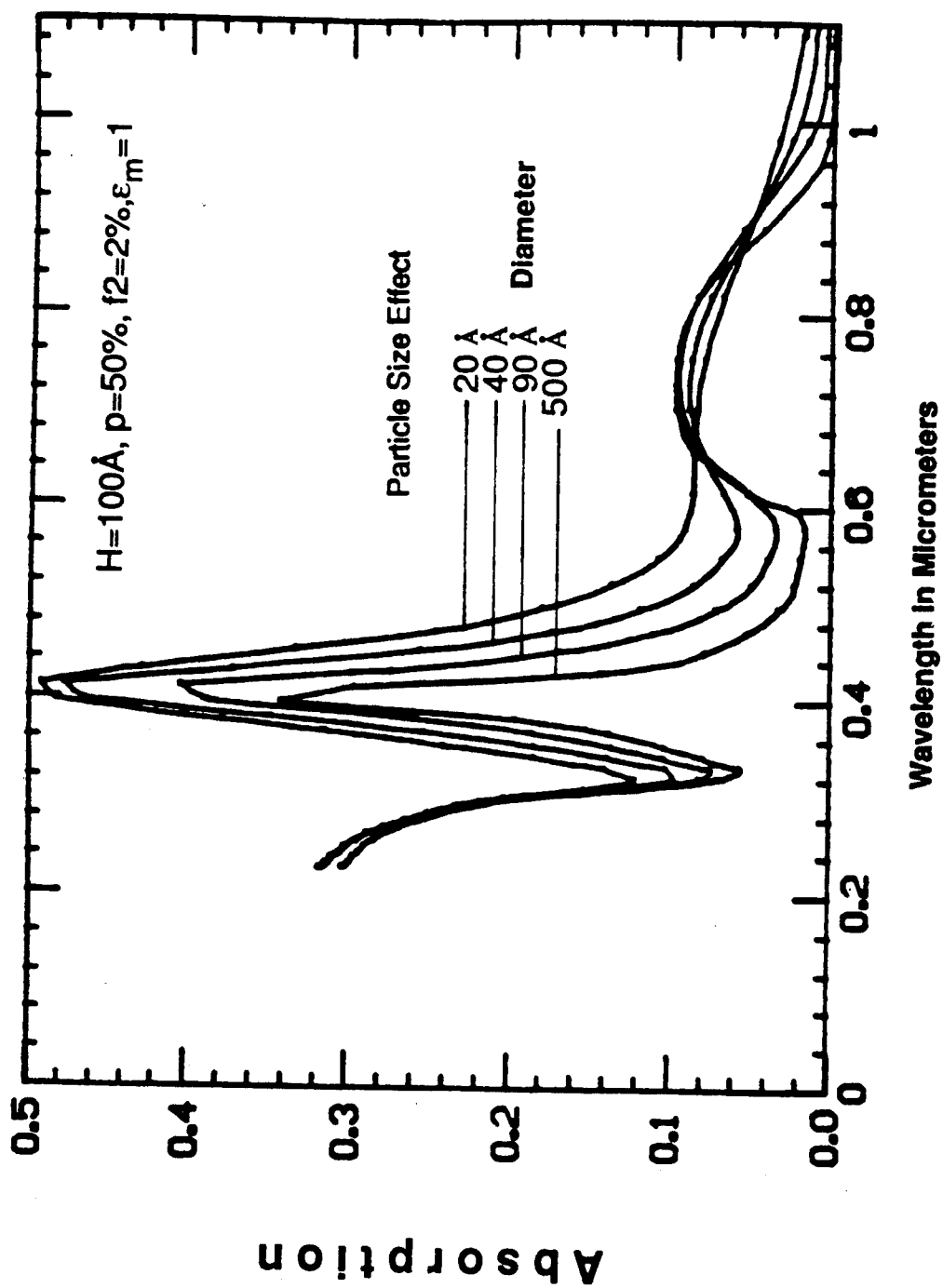


Fig. 4.13 Ag particle size effect on the S-1 surface. (b) 2-D plot.

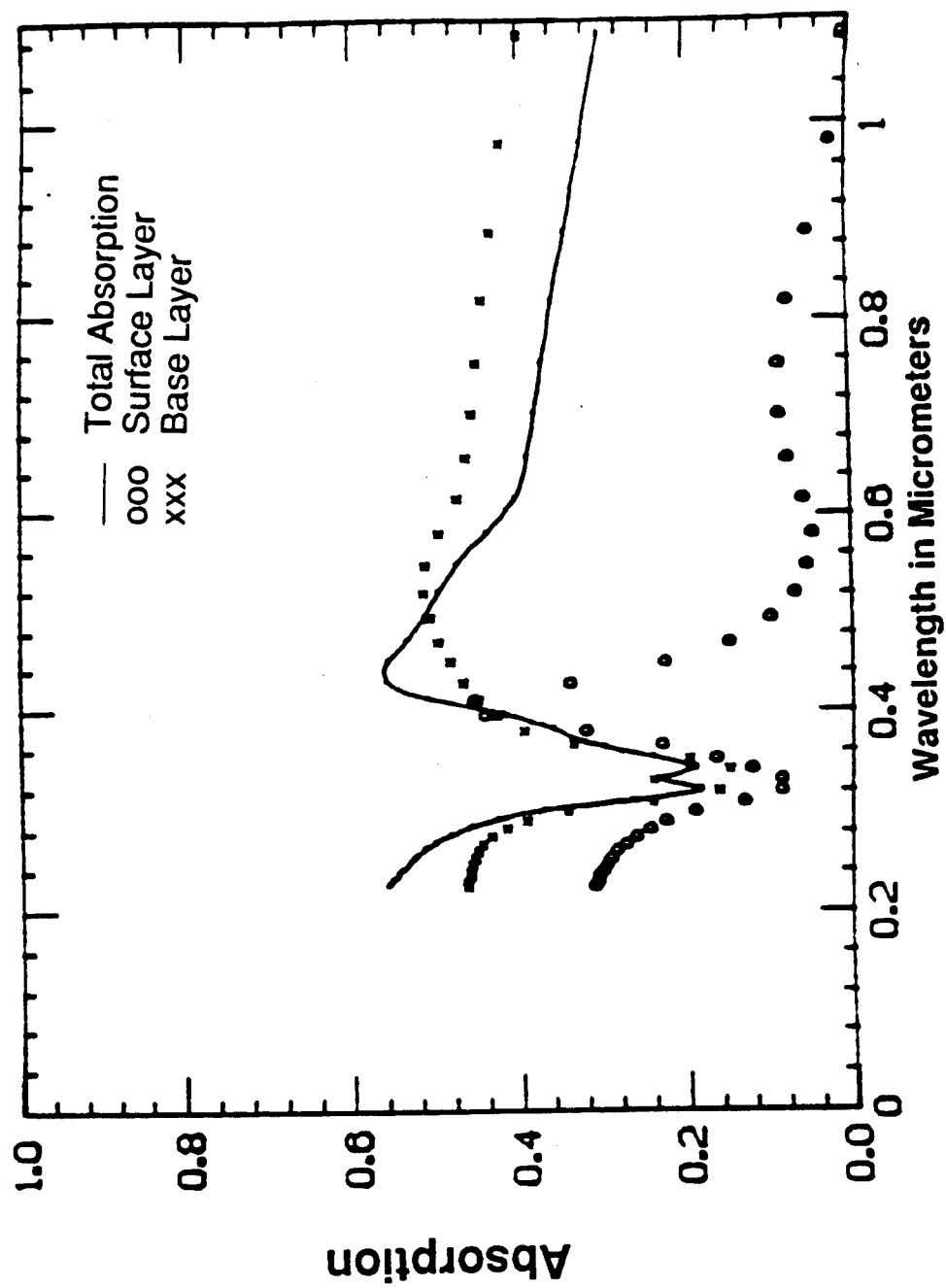


Fig. 4.14 The optical absorption of the S-1 photocathode.
 $D = 50\text{\AA}$, $H = 100\text{\AA}$, $P = 50\%$, $f_2 = 2\%$, $E_m = 1$ for surface layer.
 $D_m = 2R_m = 700\text{\AA}$, $H = 100\text{\AA}$, $P = 50\%$, $f_2 = 30\%$, $E_m = 1$ for base layer. D ranges from ≈ 100 - 1000\AA corresponding to $\alpha = 4$ in the γ -distribution.

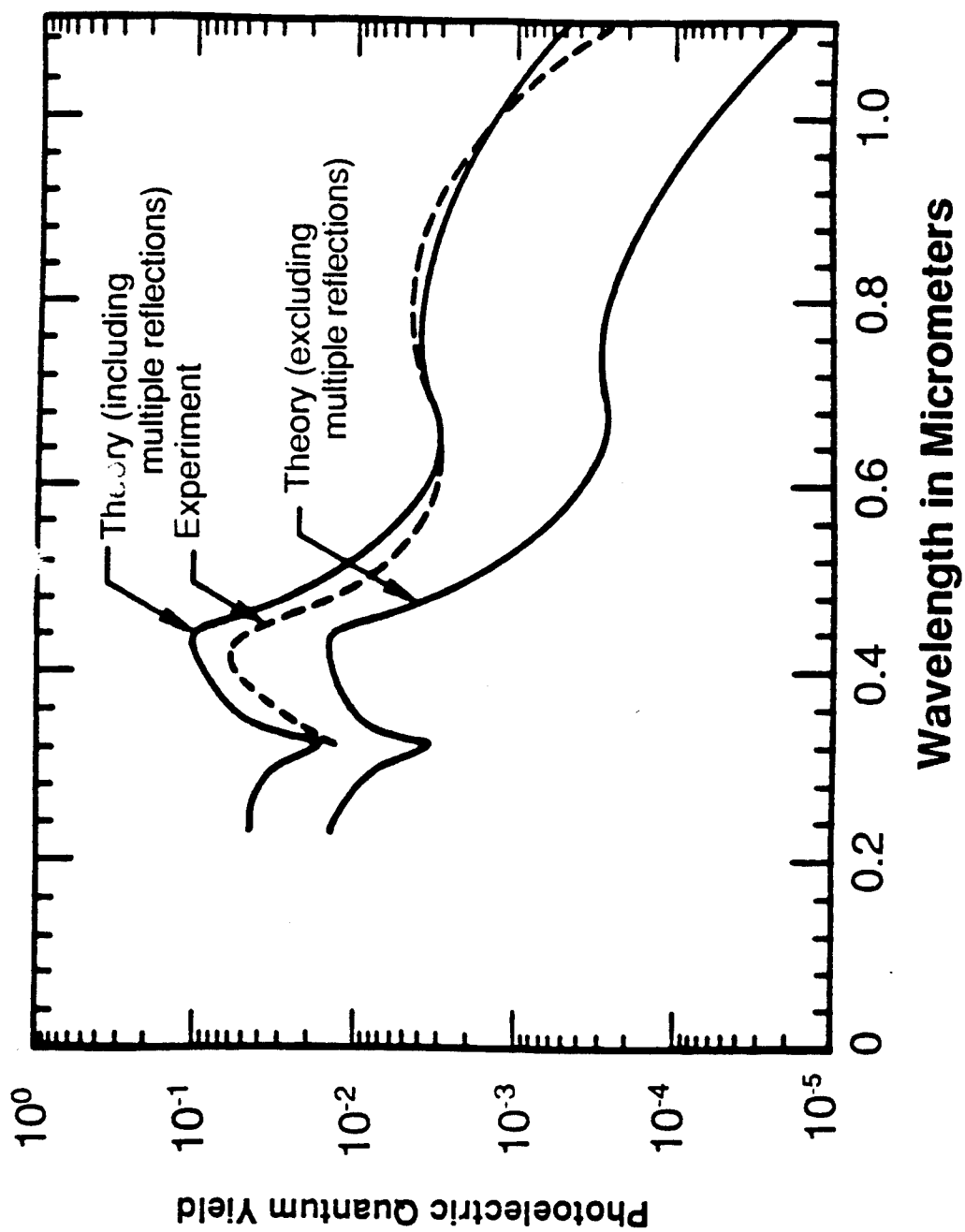


Fig. 4.15 The geometric enhancement due to the multiple-reflections of electrons in the Ag-particles.

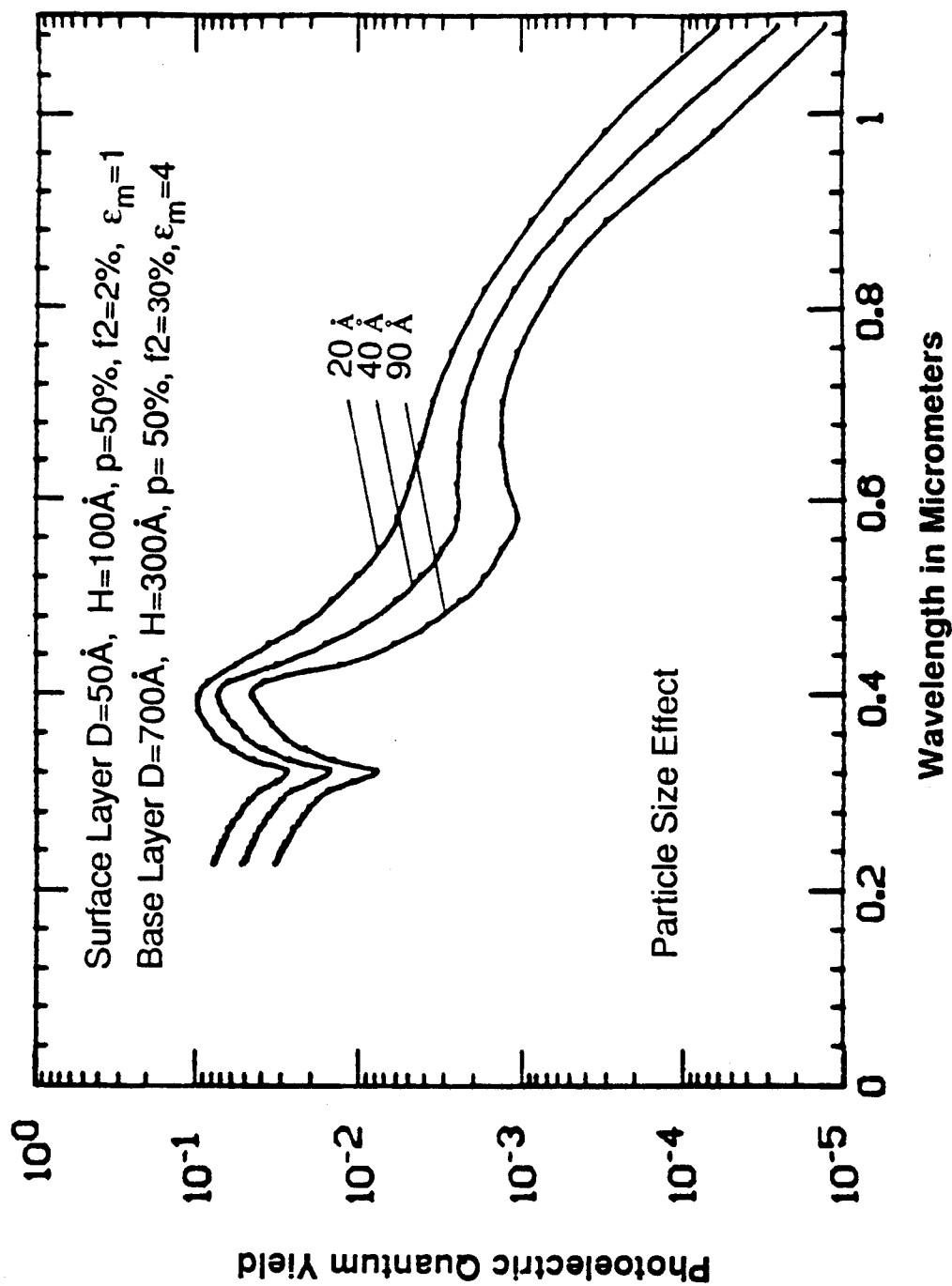


Fig. 4.16 The particle size effect on the photoelectric quantum yield of the S-1 photocathode. Note the increasing PQY at decreasing particle size D .

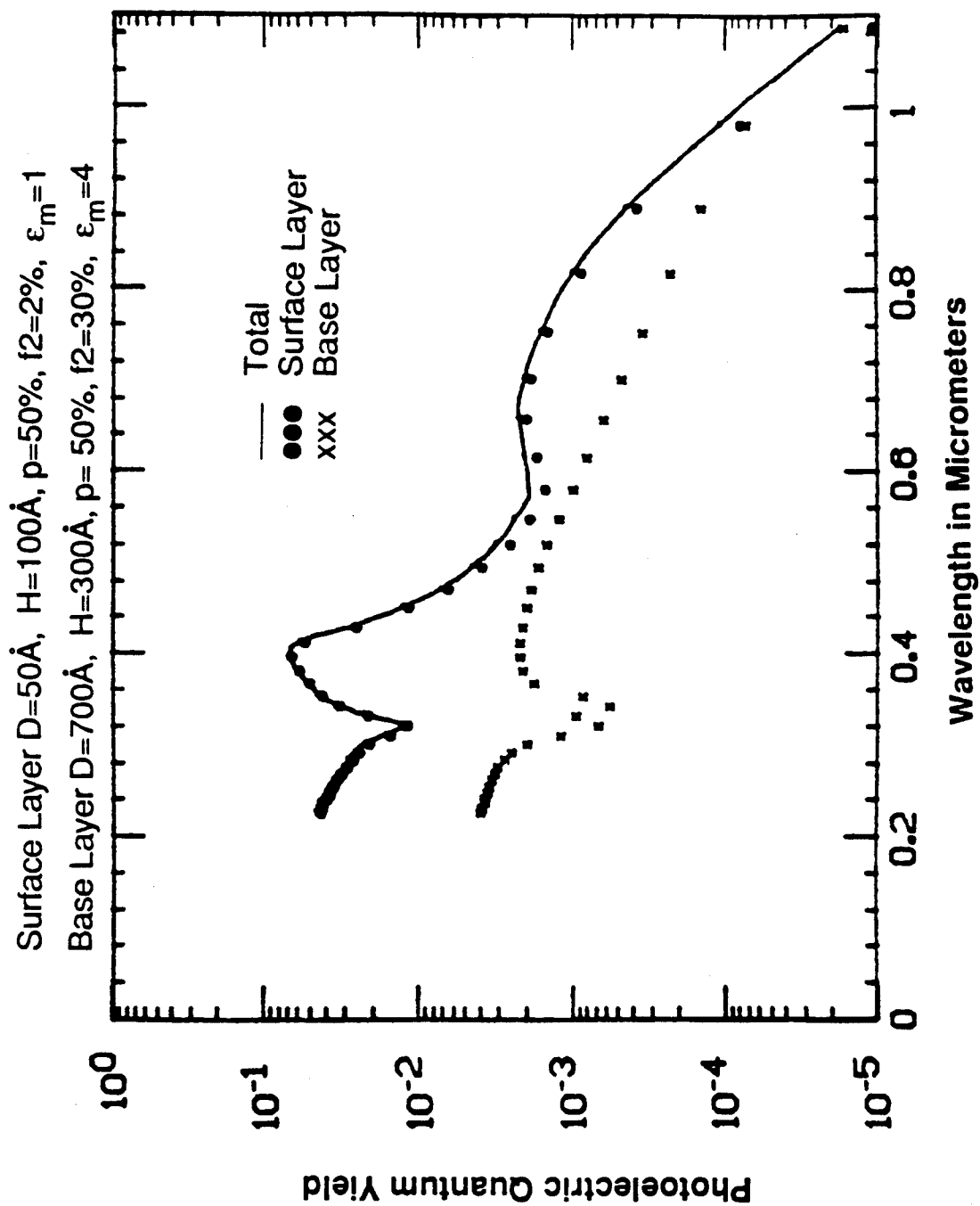


Fig. 4.17 Comparison of the contribution of PQY from the surface layer and the base layer. The solid line is the total yield given by Eqn.(20). ●●● Surface layer xxx base layer

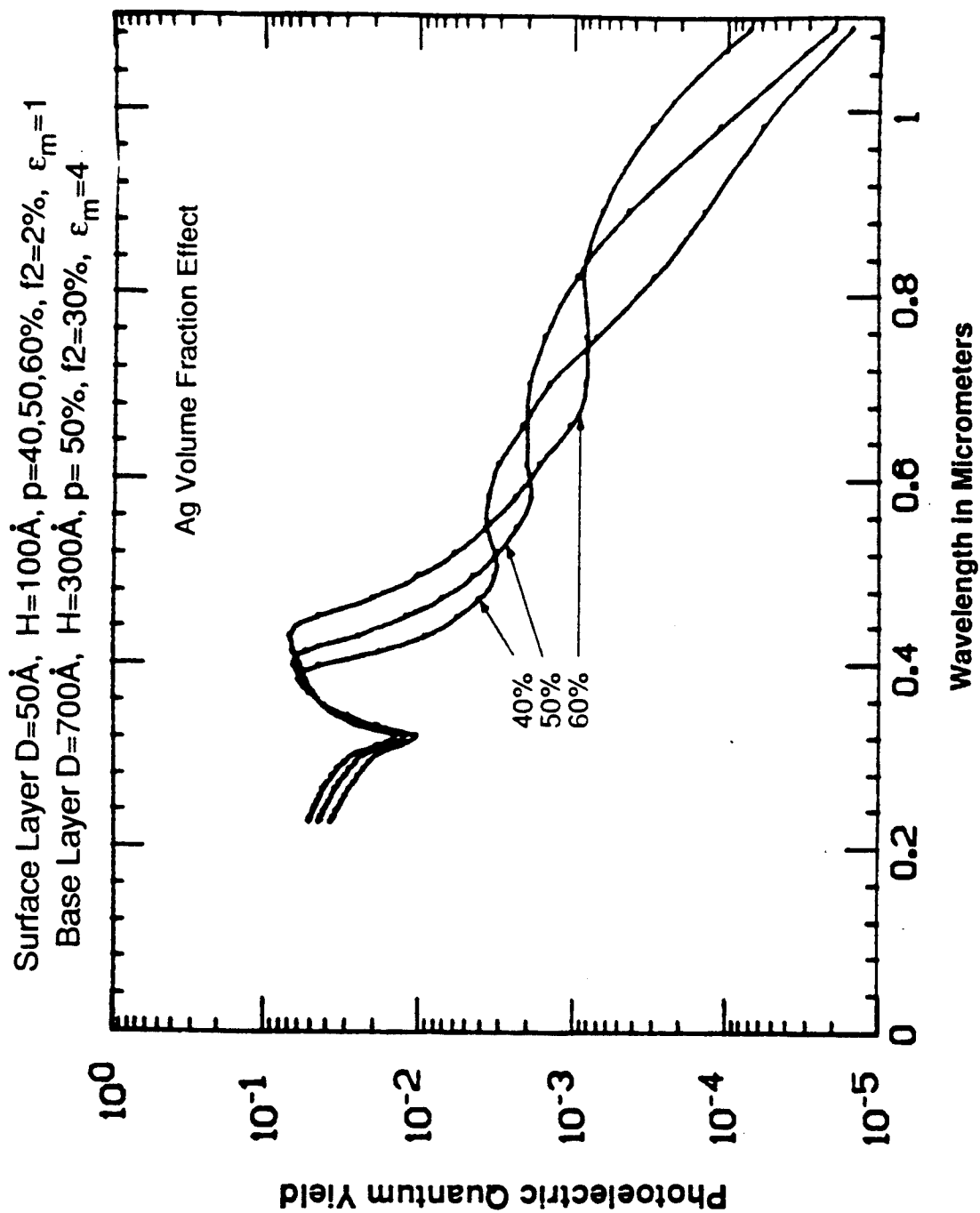


Fig. 4.18 Ag-particle volume fraction effect on the PQY of the S-1 surface.

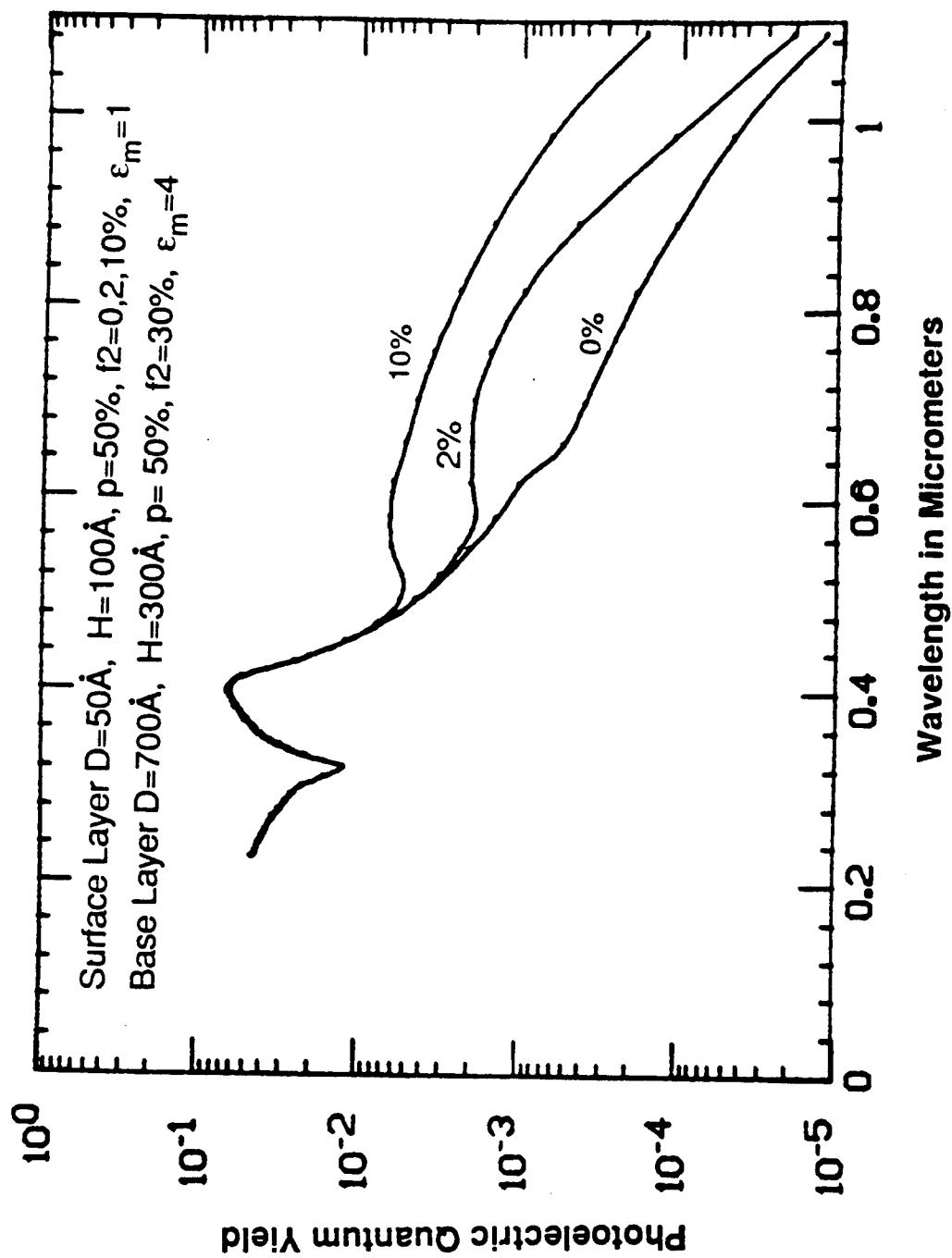


Fig. 4.19 Ag-aggregation (second unit) effect on the PQY of the S-1 surface.

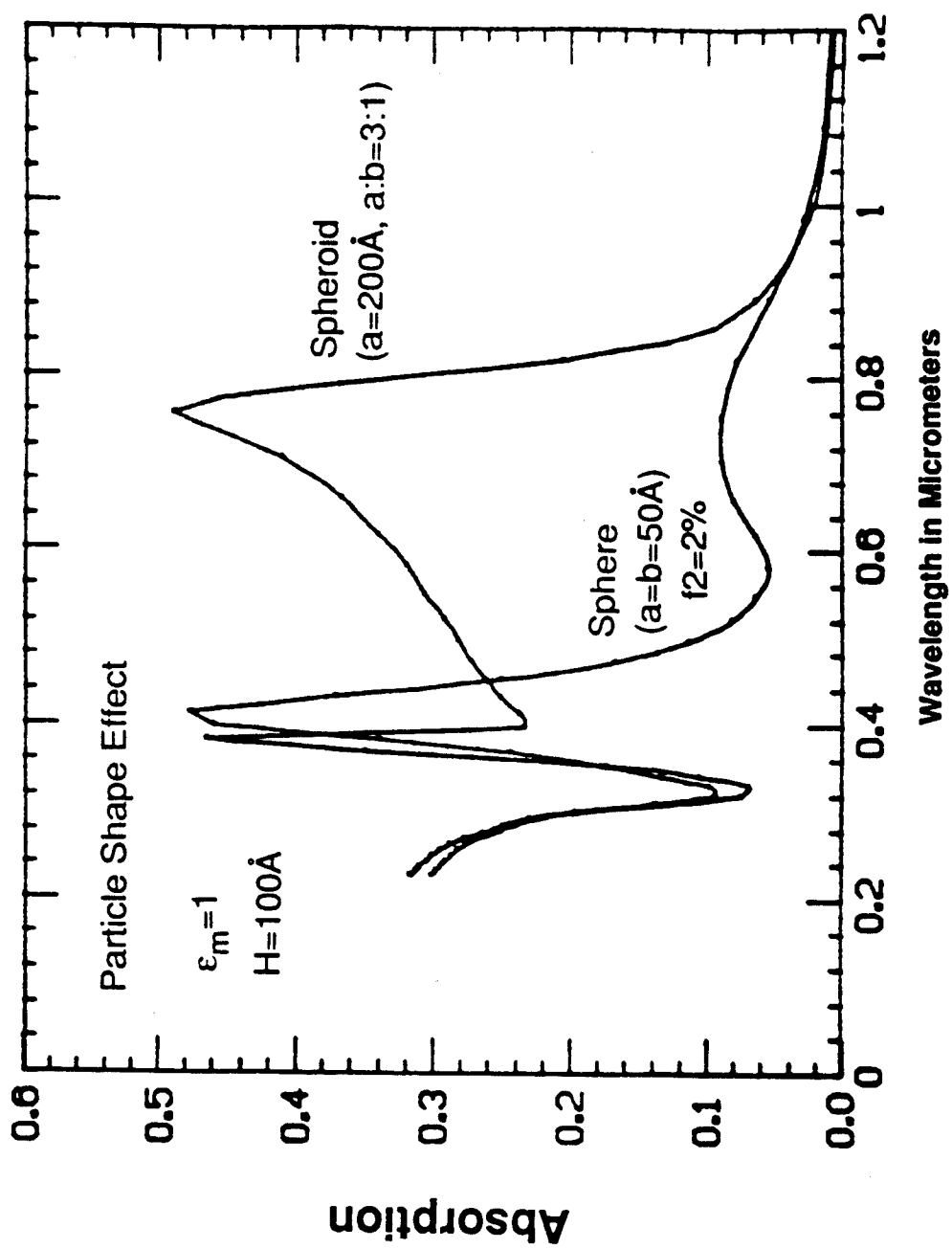
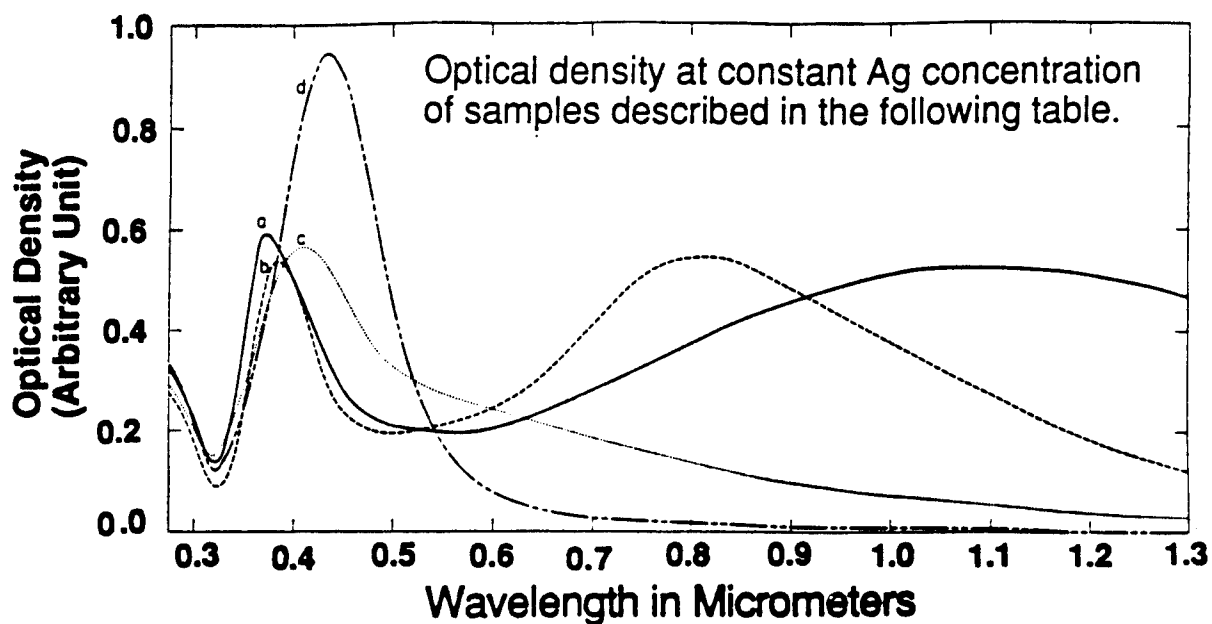


Fig. 4.20 Calculated shape effects on the optical absorptions. Spheroidal particles are more efficient in absorption than spherical ones in the infrared. Calculation based on Sheng's theory.[8]



Samples used in the work of Skillman and Berry.
[J. Chemical Physics, 48 (7), 3297-3034 (1968).]

Sample Number	Average Axial Ratio (a:b)	Equivalent Sphere Diameter (d_e in Å)
a	2.732	244
b	2.114	365
c	1.346	166
d	1.125	329

Fig. 4.21 Experimental results on the shape effects of small Ag particles in gelatine.[34,35] Agreements with calculations are remarkable.

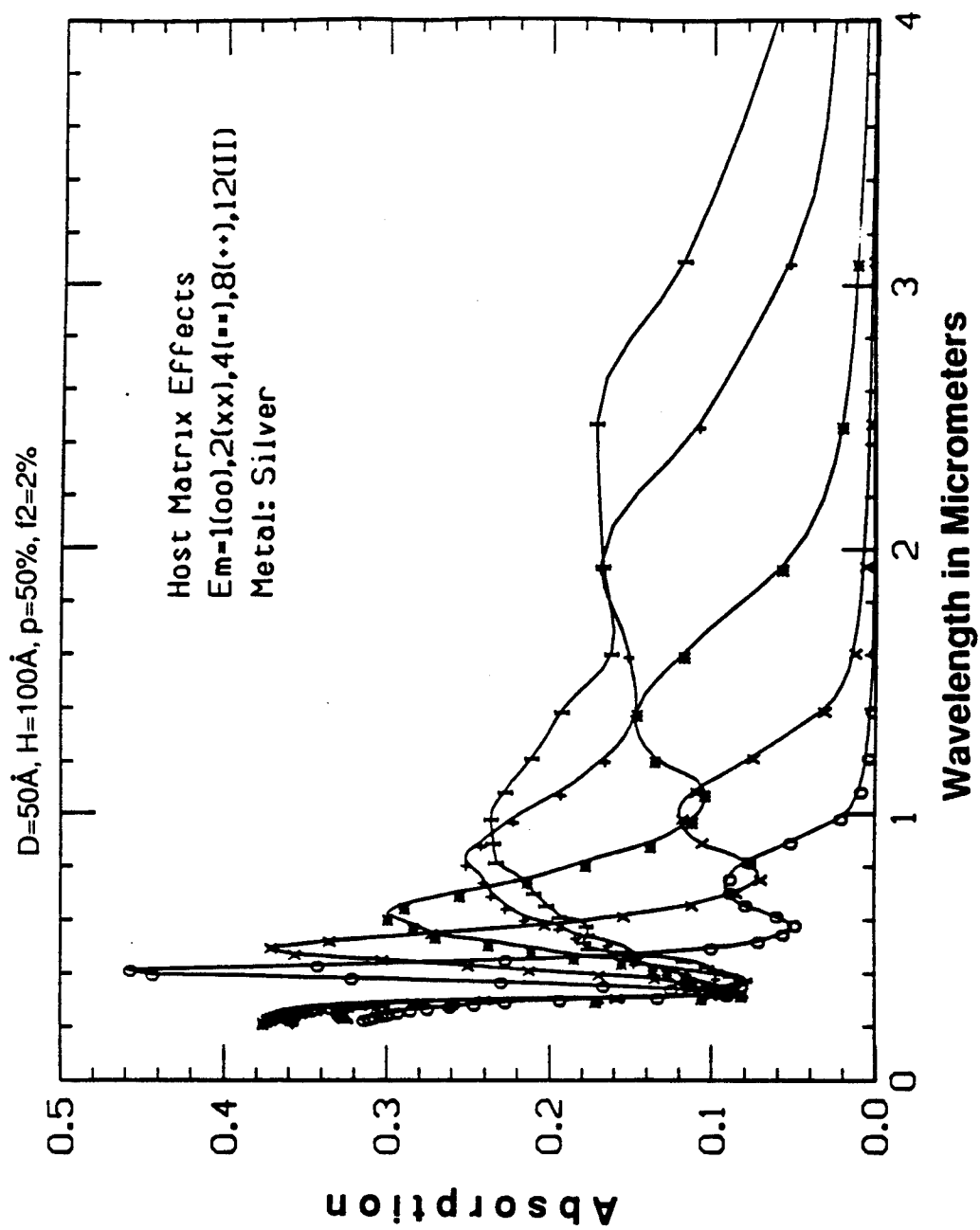


Fig. 4.22 Effects of host matrix dielectric constants on the optical absorption enhancements.

Chapter Five

Silver Particles in Semiconductors - Synthetic Random Composites -

I. Introduction

As we have already shown in the previous chapter that host matrix semiconductor materials with higher dielectric constants give higher photoabsorption, we now present the syntheses, based on this principle, of these random composites and their properties. Table I lists the dielectric constants and band gaps of a number of technologically important semiconductors,[1,2] among which many possess fairly large dielectric constants. In selecting proper materials for our applications, we also need to consider possible metallurgical complications such as the compound formation and interdiffusion between the chosen metals and semiconductors. For this reason, elemental semiconductors are the simplest to start with. Fig. 5.1.a is the phase diagram of the Ag-Si binary alloy which is characteristic of a simple eutectic system.[3] As shown in Fig. 5.1.b, the solubility of either component in the other is negligible at the temperatures we work with which are below T_E -the eutectic temperature. It suggests that annealing a Ag-Si alloy should produce the precipitation of one phase, which is a "pure" element of either constituent. When compositions are properly controlled, the second phase can be silver particles, exactly what we are driving at. In preparing Ag-Si composites, we do not go beyond the eutectic temperature in order to avoid the dissolution of silver atoms into the silicon matrix which may cause deep impurities in the Si band gap.

There are two approaches through which we made the Ag-Si random composites. One is by the co-deposition of silver and silicon followed by annealing to produce Ag precipitates (particles) in Si matrix as suggested above. The other is by alternating layer (tandem) deposition of the two constituents. Since most metal films exist in particulate form at the early stage of deposition which coalesce later on to form continuous film, it is possible to control the particle size and volume

fractions of metal particles by specifying the mass thickness of each layer and substrate temperatures. The coverage of semiconductor matrix and discontinuous metal layer stack up alternatively to reach the desired thickness. As for Ag-CuInSe₂ composites, only tandem deposition was used. In this chapter, I shall describe in section II the set-up for preparing these materials. Their microstructures are studied with X-ray diffraction, electron microscopy, photoelectron spectroscopy and sputter Auger profiling. These will be given in Section III. The optical and electrical properties will be presented in the following chapter.

Table I

**Dielectric Constants and Energy Band Gaps
of Typical Semiconductors at Room Temperature**

	$\epsilon(0)$	$E_g(300^\circ\text{K})$ eV
Diamond	5.5	5.4
Si	11.7	1.14
Ge	15.8	0.67
InSb	17.9	0.24
InAs	14.6	0.35
InP	12.4	1.35
GaP	10.2	2.26
GaAs	13.1	1.43
GaSb	15.7	0.78
PbS	205	0.35
PbSe	2800	.27
PbTe	400 -1300	0.3
ZnO	8.5	3.44
ZnS	8.1	3.91
CdS	8.3	2.58
CdTe	9.7	1.60

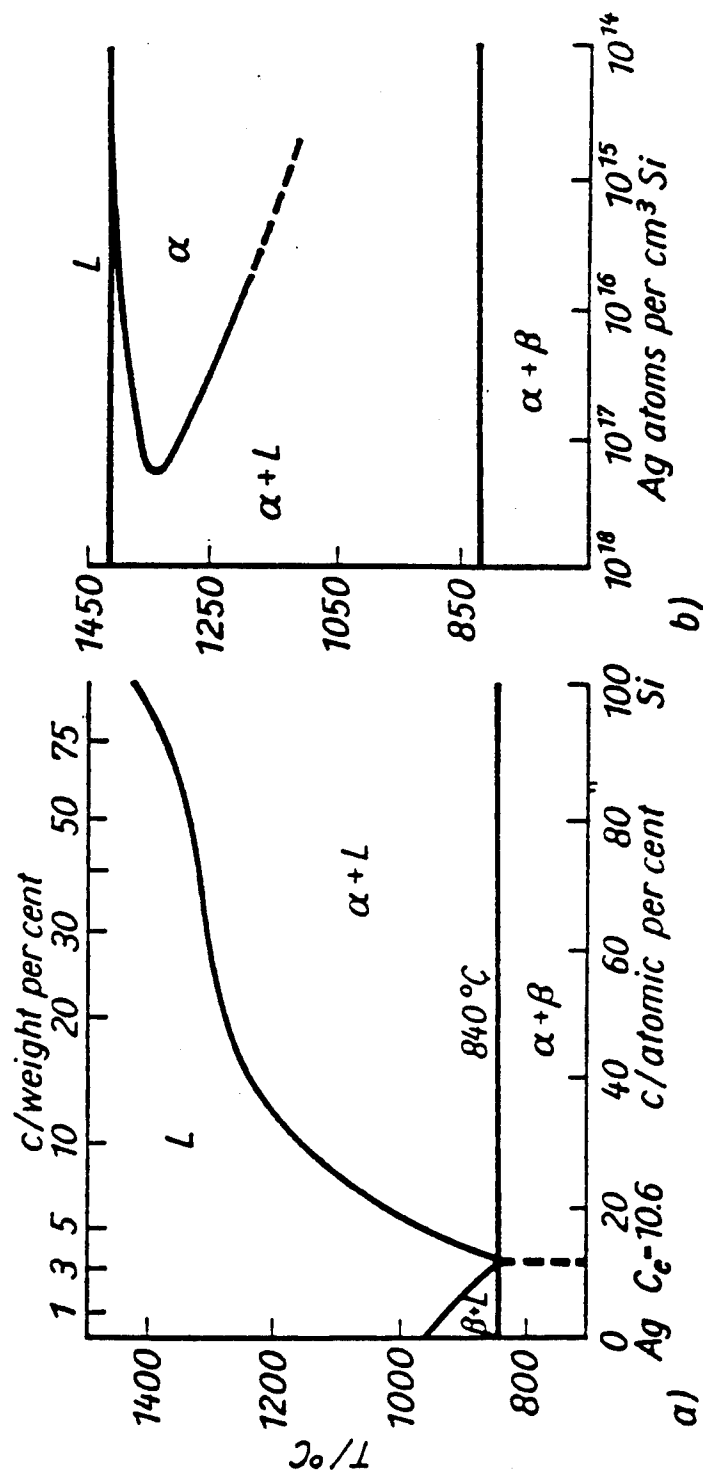


Fig. 5.1 Phase diagram of the Ag-Si system (a), and maximum solubility of Ag in Si (b). [3]

II. Experimental Set-up of Material Preparations

II.1 Sputtering Apparatus

Figure 5.2 sketches the set-up of the magnetron sputtering apparatus used in this work. It consists of a cylindrical stainless steel vacuum chamber sealed with Viton O-ring, a CTI cryogenic cryopump, mechanical roughing pump, RF and DC power supplies and a UTI 100C residual gas analyzer. Three magnetron sputtering sources mounted in the sputtering down position, which can be tilted up to 45° , and at least three side-arm magnetron sources, which can be rotated freely around the armature axis, may operate simultaneously. There is a computer controlled rotating table on which substrates are placed and a slip ring assembly which allows electric connection to rotating fixtures such as heaters. The chamber is 24" in diameter and 13.5" high.

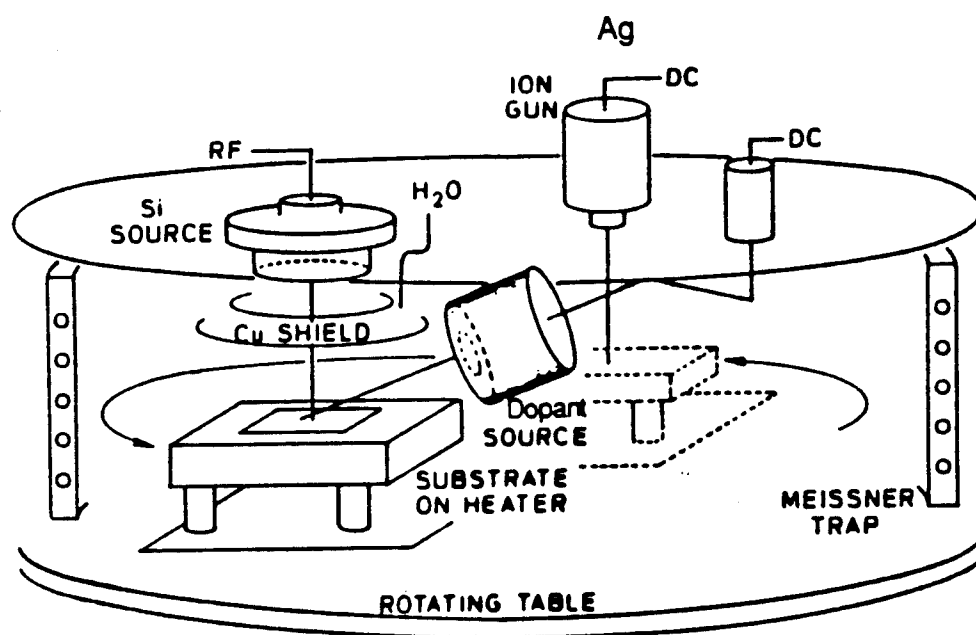


Fig. 5.2 Sketch of cosputtering configuration.

The sputter source may be 2", 3" or 6" in diameter. The sputter sources used to sputter Ag and Si are shown in Fig. 5.3. The body, target retaining ring and ground shield are aluminum. The magnets are Alnico-5 and cobalt-samarium. Target disks are mounted to the water cooled sources with vacuum grease containing silver powders for increased thermal conductivity. Reasonable deposition rates can be achieved with the magnetron configuration using low voltages (up to 1 kV) to reduce the number of high energy particles damaging the deposition surface. Low sputtering gas pressures of about a micron Hg (10^{-3} Torr) were used to attain longer mean free path of sputtered species and depositions farther from the sources with reduced particle bombardments.

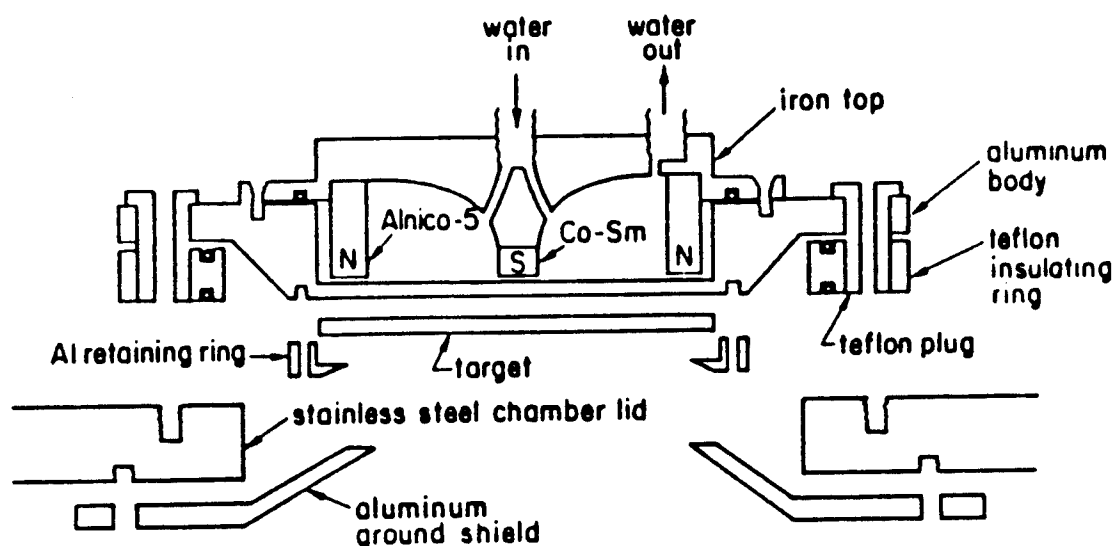


Fig. 5.3 Sketch of circular magnetron source. It shows the position of the target, chamber lid and ground shield.

A typical normalized deposition rate profile relative to that at the center of a target as a function of radial distance is shown in Fig. 5.4 for Ag and Si. Specifically for these rates, the powers are 100 Watts for Ag and 500 Watts for Si. Such a power and rate ratio is good for a 50-50 Ag-Si alloy film. For large horizontal distance between the source and substrate, such as at 20 cm in the Figure 5.4, film thickness distribution is quite uniform for both targets. The deposition profiles can be predicted with an extended ring source model.[4,5] Given stable power supplies, film thickness and composition can be precisely controlled by choosing the relative position of sources and substrates. Fig. 5.5 shows the relative position of sputter sources used in this work.

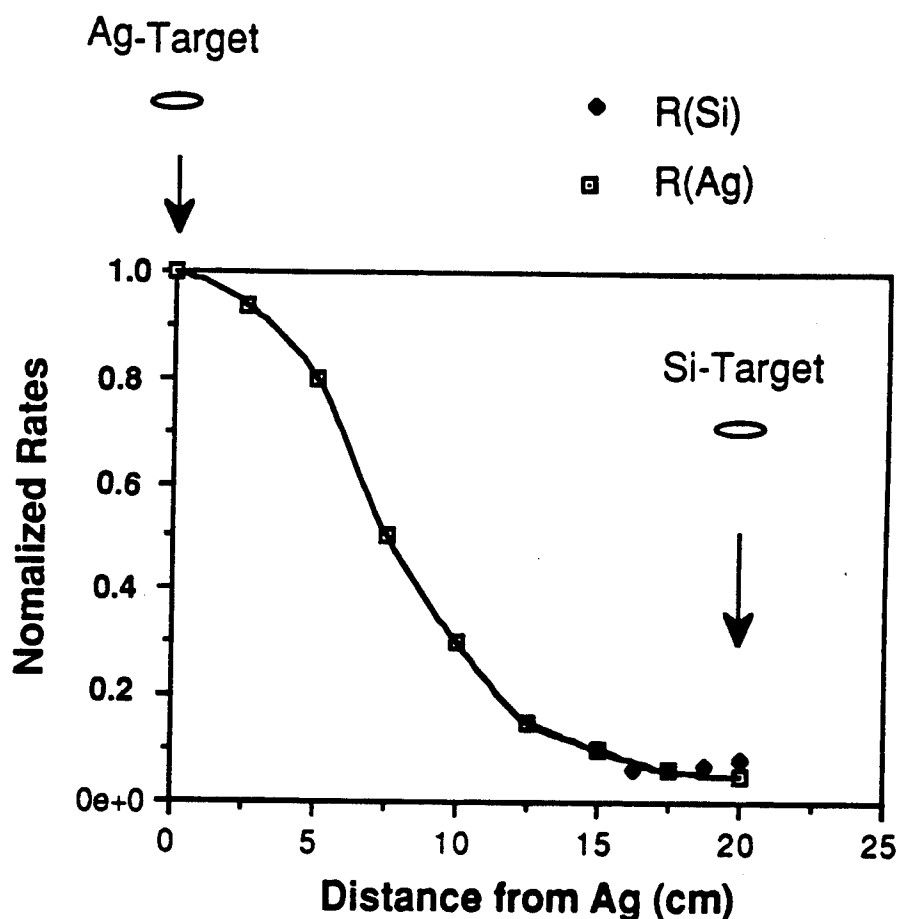


Fig. 5.4 Normalized sputtering rate as a function of the horizontal distance R between the source and substrate. (also see [4],[5])

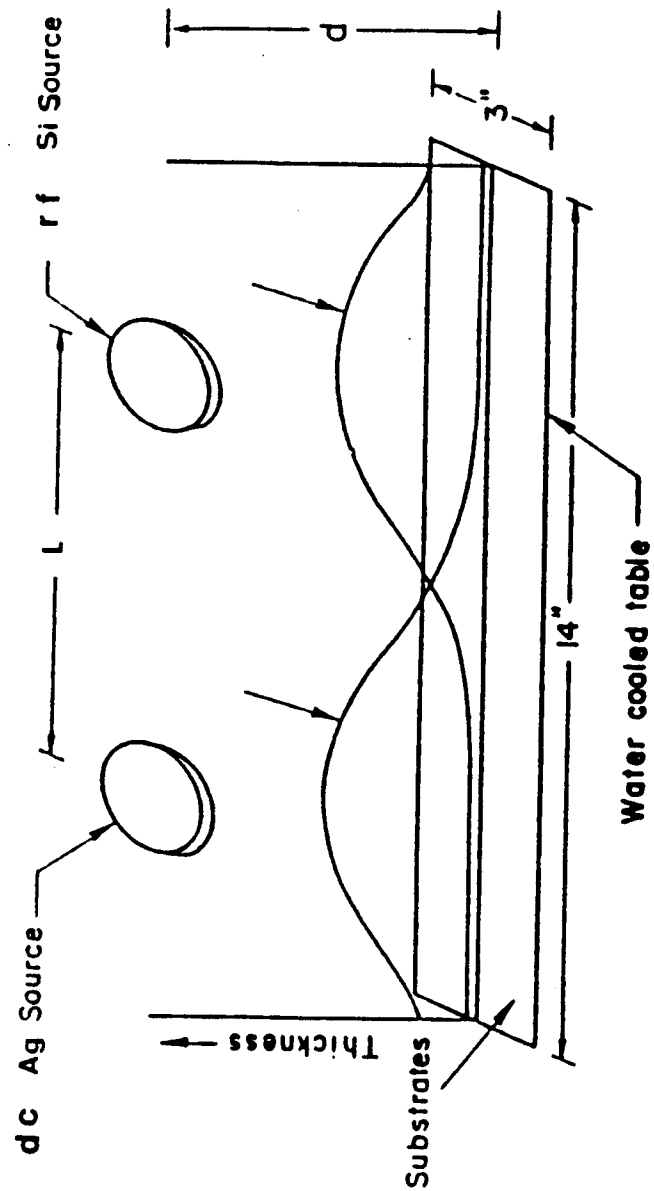


Fig. 5.5 By adjusting L and d for both sources, binary alloy films of various compositions can be obtained.

II.2 Electron Beam Deposition

Ag and Si random heterostructures can also be prepared by the electron beam deposition. The electron beam evaporation source is made by Airco-Termiscale (Gemini Model) where dual crucibles are arranged next to each other to allow co-deposition with homogeneous vapor distribution. Each crucible is independent of each other for emission power, beam density change of one pocket does not offset the rate of evaporation in the other pocket.

The Gemini electron beam source allows a shorter source-to-substrate distance, as compared with the two-source evaporation apparatus, with centers of the two sources only three inches apart. The alloy composition, which is controlled by adjusting relative evaporation rates of individual sources, is created at a relatively low point above the evaporation pools and the deposition rate can be as high as at least $15\text{\AA}/\text{sec}$, depending on the power rating. The base pressure of the bell jar can reach 10^{-7} torr while the substrate can be heated to 750°C in about two hours which then takes about 4-5 hours to cool to room temperature without purging inert gases in the the jar.

II.3 Spray Pyrolysis of CuInSe_2

The basics of spray pyrolysis have been well known and described in the literature.[6] The equipment used to prepare samples for this study consists of a separatory funnel connected with Tigon tubing to a Matheson 612 flow controller and then to a glass spray nozzle. The substrate can be heated on a stainless steel holder. Silver films are first deposited separately using sputtering techniques on glass substrates. The silver films were then heated to 300°C at which the spray deposition of CuInSe_2 was conducted. At such temperature the silver films are supposed to further break up to form more isolated small particles.[7] After deposition of CuInSe_2 on the silver film, the sample was cooled in the nitrogen flowing spray chamber to the room temperature. This process can be repeated to produced tandem layers of Ag and CuInSe_2 of arbitrary thickness.

III. Experimental Results on Microstructure Engineering

III.1 Co-deposited Random Composites

The first samples were prepared by cosputtering Ag and Si sources at room temperature on sapphire (Al_2O_3) substrates whose relative positions are arranged in such a way that the ratio of deposition rates are $R_{\text{Si}} : R_{\text{Ag}} = 85 : 15$. If the mixing of Ag and Si were complete, the post-annealing of such a sample should give the precipitates of Ag phase in the form of separated particles dispersed in the silicon matrix. The mutual solubility between them is very small and can essentially be ignored below the eutectic temperature T_E . (See Fig. 5.1) However, in Fig. 5.6 we see that the silver and silicon are separated into two layers for the cosputtered Ag-Si film. Ag atoms outdiffused to the surface of the alloyed film leaving only trace amount of silver particles behind in the silicon matrix. The total film thickness was 2000\AA while the semicontinuous Ag film showed an average grain size of ca. 300\AA according the X-ray diffraction and TEM micrographs – an implication of almost complete segregation. ($2000\text{\AA} \times 15\% = 300\text{\AA}$.) Though the exact causes of Ag outdiffusion in the Ag-Si alloy are not known without further investigations, we can speculate that the strain and surface energies incurred by the silver second phase precipitation in the Si matrix may be so large that the exclusion of the silver phase from the silicon is favored. This TEM result is confirmed by the sputter Auger profiling, as shown in Fig. 5.7 of a sample film with 50:50 Ag:Si cosputtered under the otherwise similar conditions compared to the previous 15:85 Ag:Si film. The intriguing phenomenon recognized in this film is the high oxygen content in the silicon matrix. For comparison, in Fig. 5.7 we have already normalized the Auger peak to peak intensities with relative sensitivity factors of 1.03:1:3.3 for Ag:Si:O. It is possible that as Ag atoms outdiffused to the free surface and joined each other to form a discontinuous film, the vacancy sites previously occupied by Ag atoms left behind in the a-Si matrix were taken up by oxygen from the surface on exposure to the air. This speculation on the oxygen uptake is supported by the similar relative amounts of Ag and O in Si. The oxygen did not come from the sapphire substrate since no aluminum peak was identified accompanying the

oxygen peak. For detailed atomic transport mechanism, more investigation will be needed. This, however, will not be explored in the present work.

In order to overcome the problem of surface segregation, we put on top of the cosputtered Ag-Si alloy film an overlayer of either silicon or carbon right after the co-deposition. When either of these overlayers is introduced, the surface condition of the Ag-Si film could have been changed in such a way that the Ag atoms prefer to stay in the Si matrix rather than to outdiffuse. The Ag phase then precipitate out of the matrix upon subsequent annealing at an adequate temperature.

In Fig. 5.8 we show the TEM micrograph of the sample with a 200Å Si overlayer deposited 5 minutes after the cosputtering of the 2000Å Ag-Si alloy film ended. We can see that the clustering of silver particles (dark areas) has already begun. These clustered particles sit at the interface between the 2000Å Ag-Si alloy and the 200Å Si overlayer. In this micrograph we notice that there are regions where silver particles are isolated and regions where particle clusters enclosing silicon matrix. As was discussed in the previous chapter, the later regions, the so called second microstructural unit, are essential to enhanced infrared absorption while the isolated particles, the so called first microstructural unit, are responsible for photoabsorption in the shorter wavelength range. The optical properties of the materials discussed in this chapter will be presented in the following chapter. Fig. 5.9 is a cross-section TEM micrograph showing these clustered particles. They are formed by the outdiffused (segregated) Ag-atoms from the Ag-Si alloy film. If there were no delay in the surface coverage after cosputtering, this segregation can be avoided. Fig. 5.10 shows the sputter Auger profile of a sample similar to the previous one except for no delay in depositing the surface overlayer. There is no surface segregation of Ag observed. Furthermore, the composition of this film is fairly uniform. The volume fraction of silver is around 40% according to this result. From the XPS analysis of the integrated intensities of Ag 3d and Si 2p peaks, we also obtain similar compositions for these samples.

Meanwhile, carbon overlayer works as effectively as silicon in the prevention of silver surface segregation. Fig. 5.11 is the TEM micrograph of a 2000Å thick 50-50 Ag-Si alloy film

cosputtered at room temperature and covered with 30-50Å of carbon on the surface. The homogeneous mixture of silicon and silver without any segregation is clearly observed. X-ray and electron diffractions show a silver (111) peak on the background of amorphous silicon which suggest that the silver phase exists in microcrystalline form, rather than atomic. As this sample was heated by an electron beam at an energy of 120 KeV with beam size $\approx 2000\text{\AA}$ at a medium aperture for a few seconds, microparticles of silver precipitated out of the silicon matrix. The particle size is around 20-50 Å and the particle distribution is fairly uniform. If this sample was heated at 500°C for 30 minutes, larger particles of 50-100Å are observed as shown in Fig. 12. This coarsening of particle size is also observed in the X-ray and electron diffraction patterns. Fig. 5.13.a and b show the Ag (111) electron diffraction pattern of a Si-overlayered Ag-Si alloy film as-cosputtered and heated under the above-mentioned conditions, respectively. The breakage of electron diffraction patterns for as-deposited films from continuous rings into discrete spots for annealed film further demonstrates the growth of Ag particles.

If there was a delay of 5-10 minutes in this carbon coverage, a certain amount of Ag surface segregation occurred which was then stopped by the carbon overlayer. As shown in Fig. 5.14, the sputter Auger profile evidences this segregation. From these results we can therefore conclude that silicon and carbon overlayers work equally well in preventing surface segregation of silver in Ag-Si alloy film.

III.2 Tandem Deposited Random Composites

Now, we consider the tandem deposited films. We again start with the Ag-Si system. Fig. 5.15 shows the SEM micrograph of a sample deposited on the sapphire substrate at 600°C in the sequence of Al₂O₃/Si 200Å/Ag 200Å/Si 200Å/Ag 200Å/Si 300Å. The α -step interferometer measurements give the thickness of this film as approximately 1200-1400Å. The dark areas in this micrograph are silicon while the bright ones silver particles, contrary to the black and white contrasts in TEM micrographs. Note that there are regions where silver particles are surrounded

by silicon (i.e., isolated silver particles or the first microstructural unit), and regions with clustered silver particles enclosing the silicon matrix (the second microstructural unit). The particle size ranges approximately from 100Å to 3000Å with central (mode) radius of 1000Å. From X-ray diffraction analysis, it is found that the silicon matrix is polycrystalline with better crystallinity and texture (narrower and more intensified Si peaks) as compared with the cosputtered a-Si/Ag films followed by annealing at 600°C for 70 minutes. With higher substrate temperature, the particle size increases. SEM observation of a 0.5µm film deposited at 700°C in the sequence of Al₂O₃/Si 200Å/Ag 200Å/Si 200Å/ ---- /Ag 200Å/Si 200Å indicated that the particle sizes were indeed larger than those deposited at lower temperature. From the kinetic and thermodynamic point of view, the coarsening of silver particles at higher temperatures reflects the surface diffusion of silver atoms on silicon surface. It also suggests that, thermodynamically, the total surface free energy will decrease at growing particle sizes (and thus smaller surface to volume ratio). The growth of larger particles at the sacrifice of smaller ones resembles that in Ostwald ripening[8] for the nucleation and growth of second phase in alloy systems.

Complicated as a Ag:Cu-In-Se quaternary system might seem at first glance, CuInSe₂ as host semiconductor matrix embedding silver particles prepared by tandem deposition seems to work satisfactorily well with no observable silver compound formation. SEM micrograph of this film is shown in Fig. 5.16. As will be described in the upcoming chapter, optical measurements also suggest that no such compounds as AgSe₂ or CuSe₂ has been identified in the Ag-composite system while CuSe₂ phase has been observed in the bare CuInSe₂ film (both deposited at 300°C exactly under the same conditions).

In principle, at a proper substrate temperature, tandem deposition of very thin metal and semiconductor films may result in random composites of metal particles in a semiconductor matrix as long as no metal-semiconductor compound formation or interdiffusion is incurred. To understand why such a complicated quaternary system has no Ag compound formation or alloying, extensive studies are necessary although not attempted in this work.

IV. Conclusions and Further Discussions

As shown above, random composites of small metal particles in a semiconductor can be fabricated in a number of ways. In the tandem deposition method, we have not attempted in this work to control the particle size by atomizing the evaporated materials before their depositing onto substrates. However, it is well known that metal particle size is closely related to the nucleation and growth processes of small metal clusters or islands. If we could make the deposition happen at low temperatures where diffusion is limited, the Ostwald ripening type growth of metal particles would be deterred or even prohibited and the particle size could therefore be as small as how many atoms ever arrived at the nucleation sites on the substrate. In other words, if the nucleation occur more evenly on the substrate and, furthermore, the subsequent coalescence of these nuclei could be overcome, the particle size may be controllable. This can also be achieved either by a plasma process (ion beam bombardment) or purging inert gas through the evaporation chamber.

It is also understood that the metal particle shapes are more difficult to control in tandem deposited films. Co-deposition is thus preferred in this regard. In co-deposition of Ag and Si, surface segregations of Ag were observed. This surface segregation is a dynamic process which may well have started while the alloy film is being deposited. It can be prevented by controlling the film surface condition through depositing an overlayer.



Fig. 5.6 TEM micrograph of a discontinuous Ag film on a-Si layer for an alloy of $\text{Ag}_{15}\text{Si}_{85}$ cosputtered at room temperature.

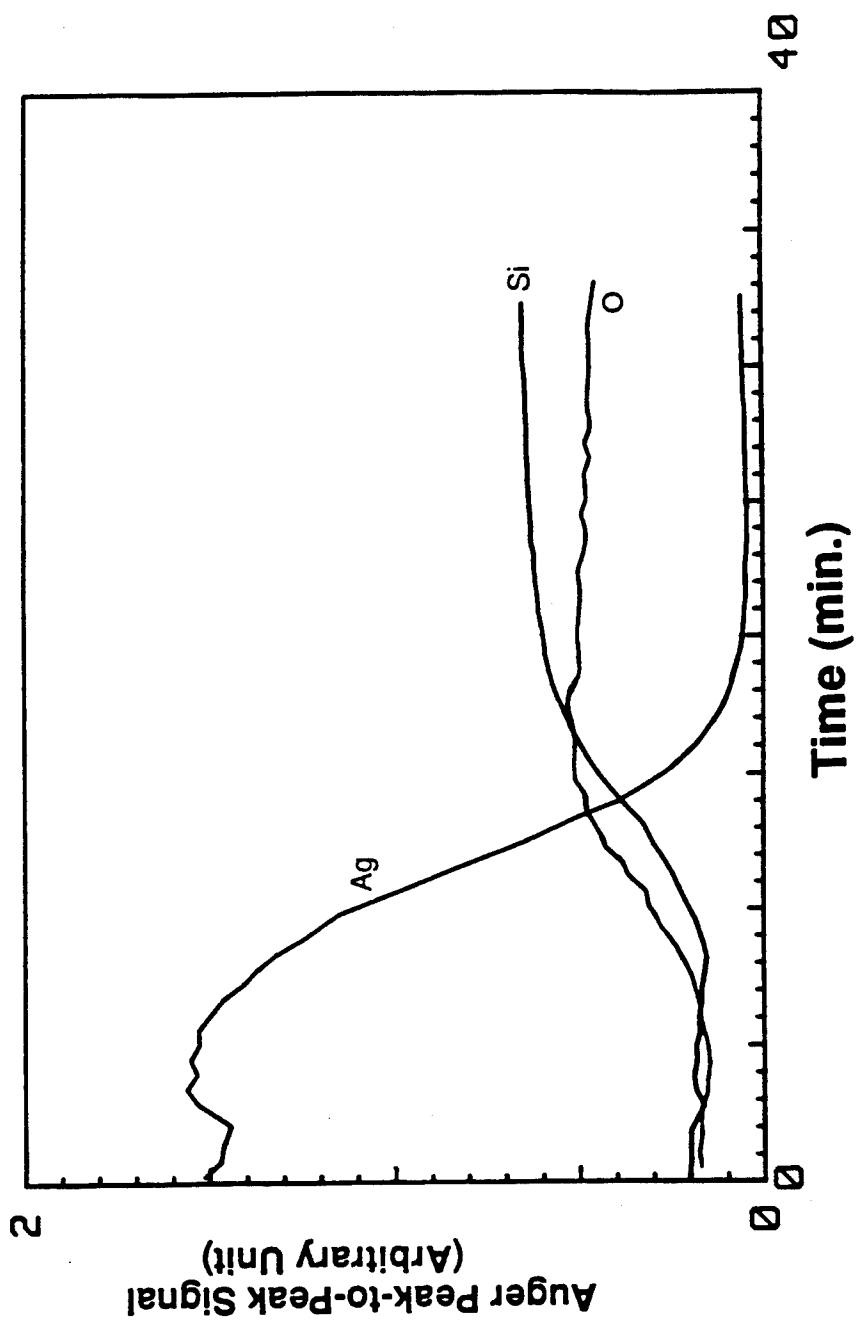


Fig. 5.7 Auger depth profile for a film of $\text{Ag}_{50}\text{Si}_{50}$ cosputtered at room temperature. Si 2p and Ag 3d peaks as references. Sensitivity factors have been included.

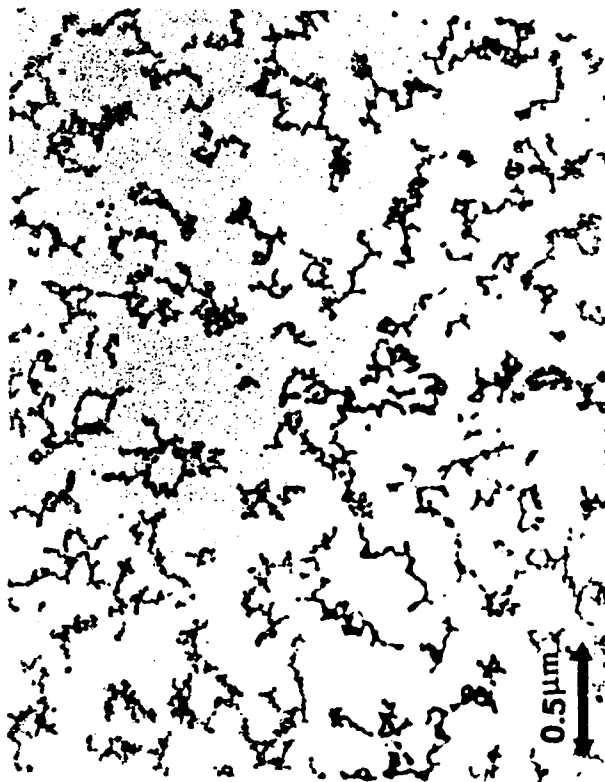


Fig. 5.8 Surface segregation of Ag in AgSi alloy film is a dynamic process even at room temperature. Small clusters of Ag have begun to form when an overlayer was not deposited in time.



Fig. 5.9 Cross section view of the previous figure.

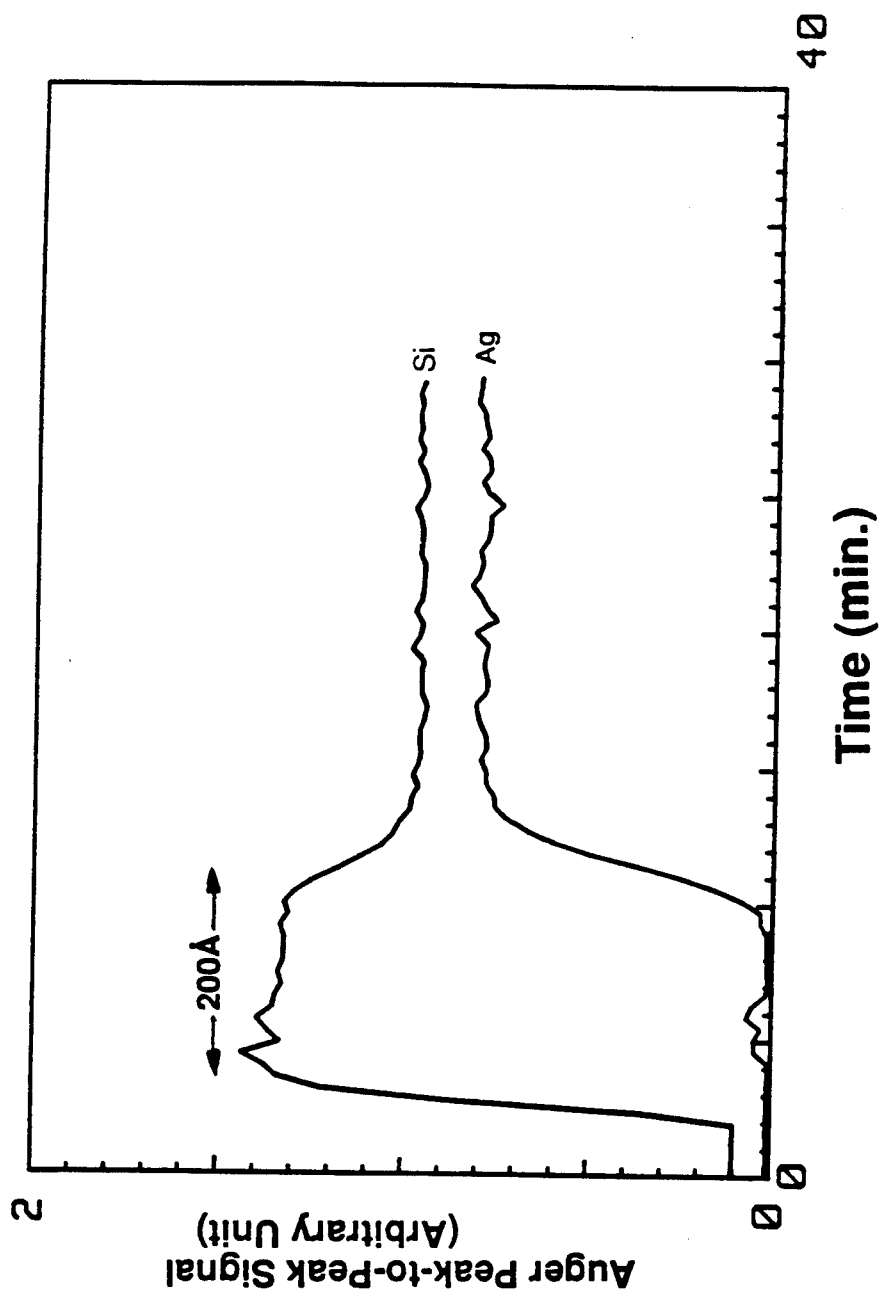


Fig. 5.10 Sputter Auger profile of AgSi film with a timely deposited 200Å Si overlayer. (Cosputtered at R.T.)

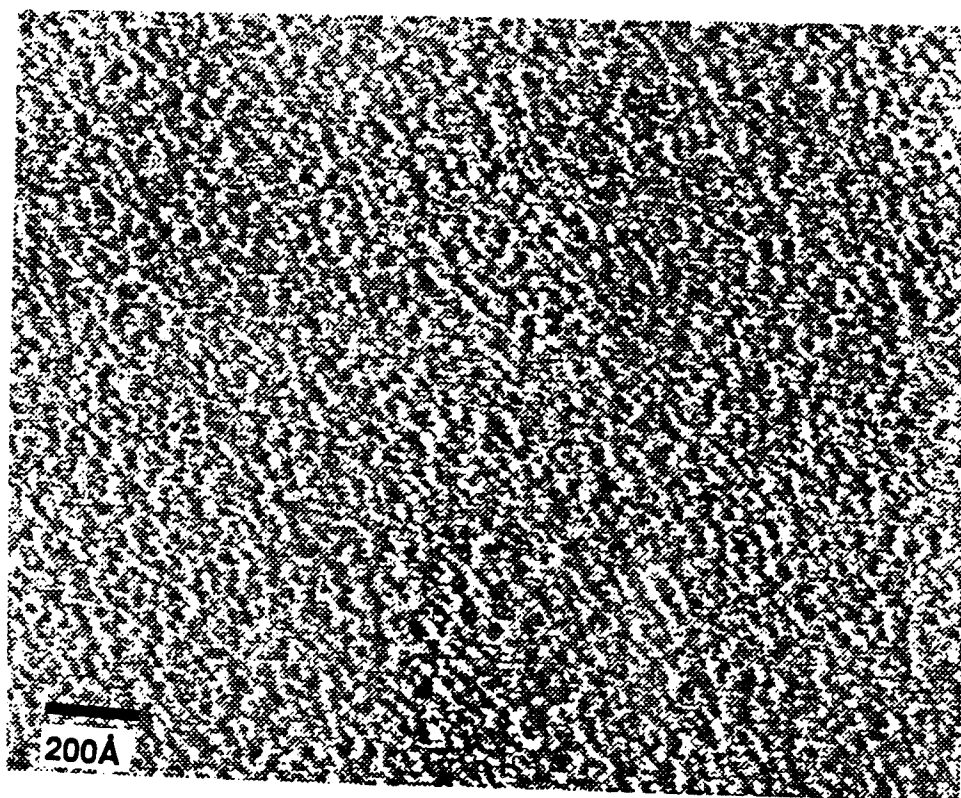


Fig. 5.11 Top view TEM micrograph of AgSi film with a timely deposited 30-50Å carbon overlayer.

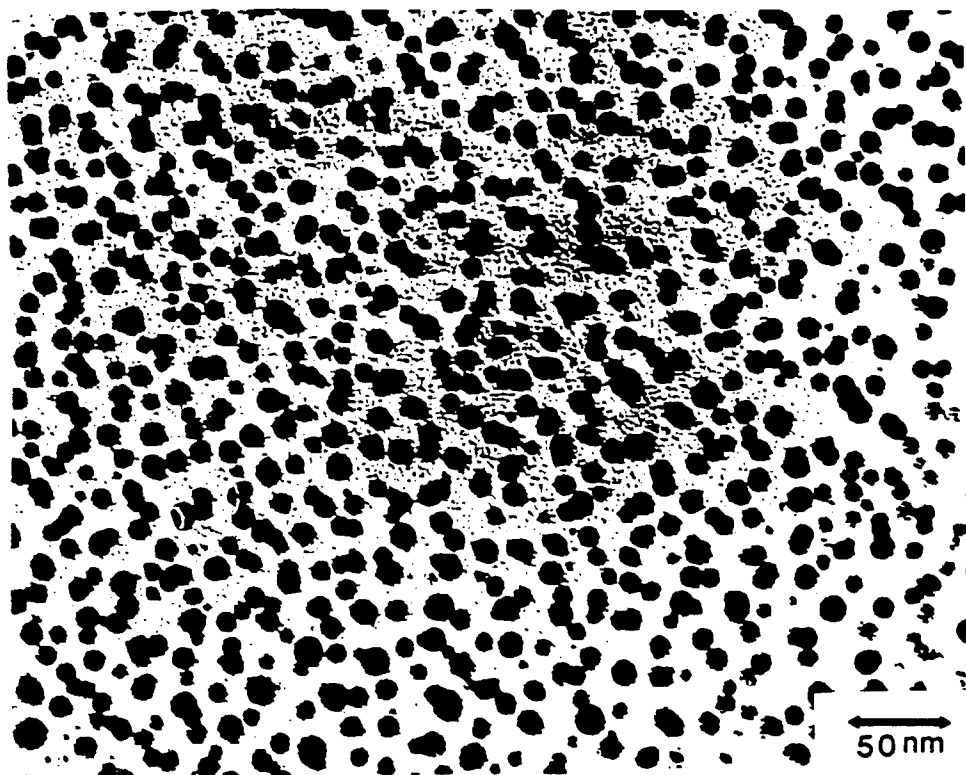
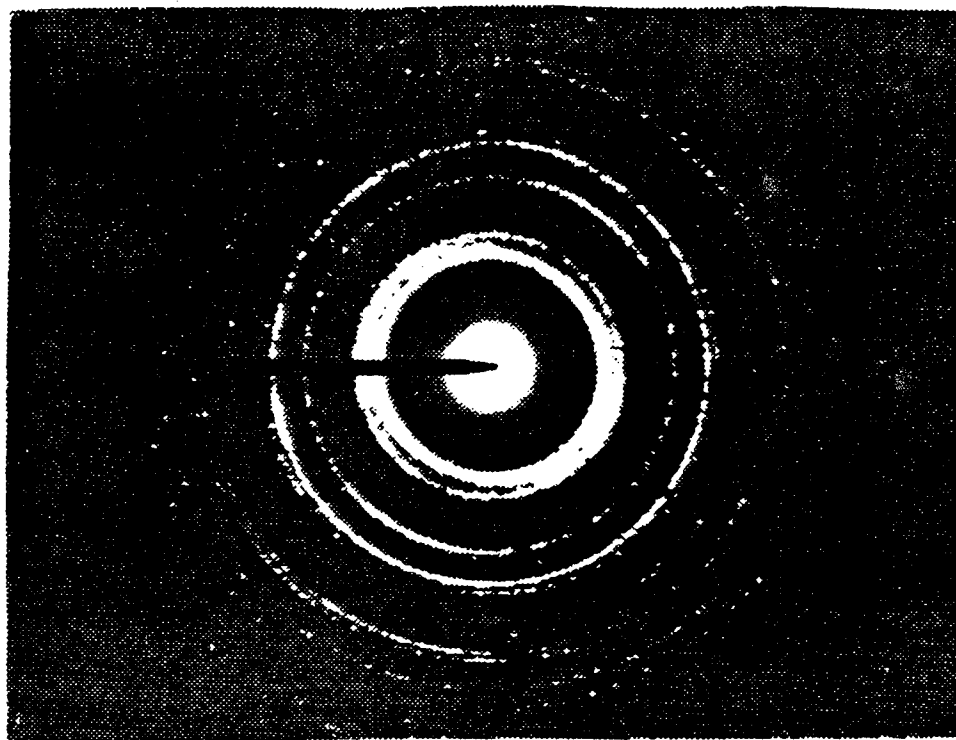


Fig. 5.12 Sample of Fig. 5.11 heated at 500°C for 30 mins., small Ag particles $\approx 100\text{\AA}$ in size precipitate out of the matrix.



(a)



(b)

Fig. 5.13 (a) Electron diffraction pattern corresponding to Fig. 5.11, and (b) to Fig. 5.12.

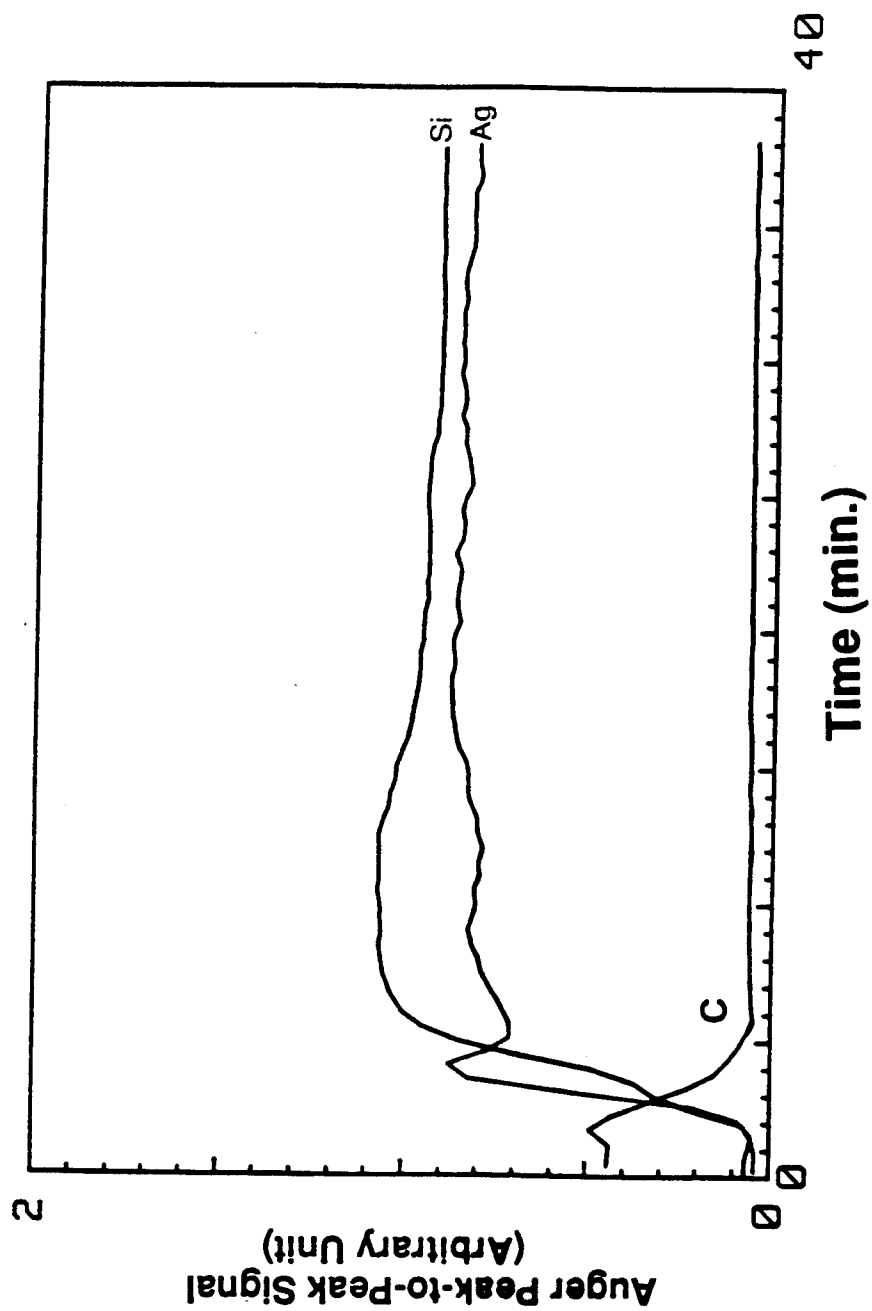


Fig. 5.14 Auger profile of a film as in Fig. 5.11 except for a 5-10 minutes delay in overlayer deposition.

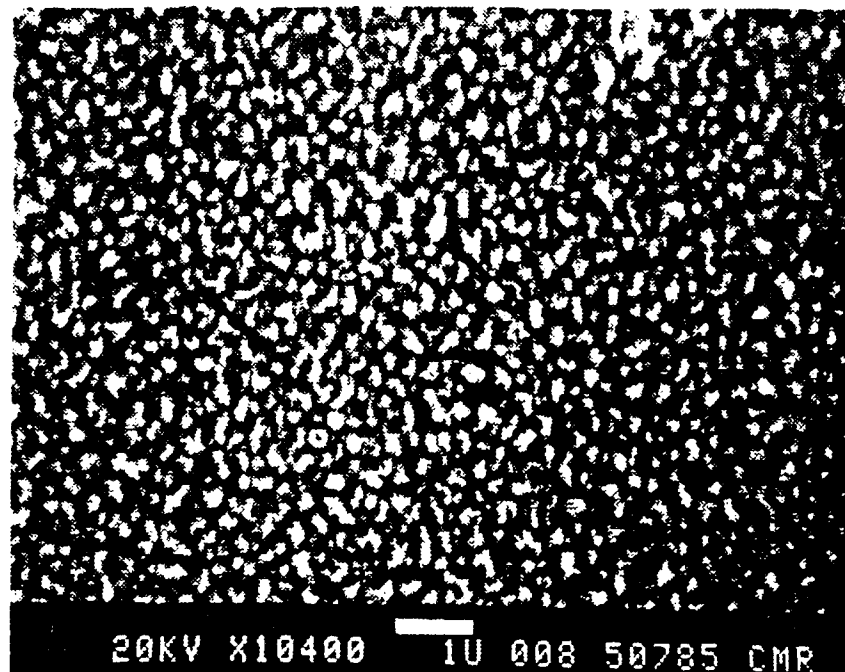


Fig. 5.15 1100Å AgSi film prepared by tandem deposition of five $\approx 200\text{\AA}$ alternating layers of Ag and Si. Substrate Temperature $T_{\text{sub}}=650^\circ\text{C}$.

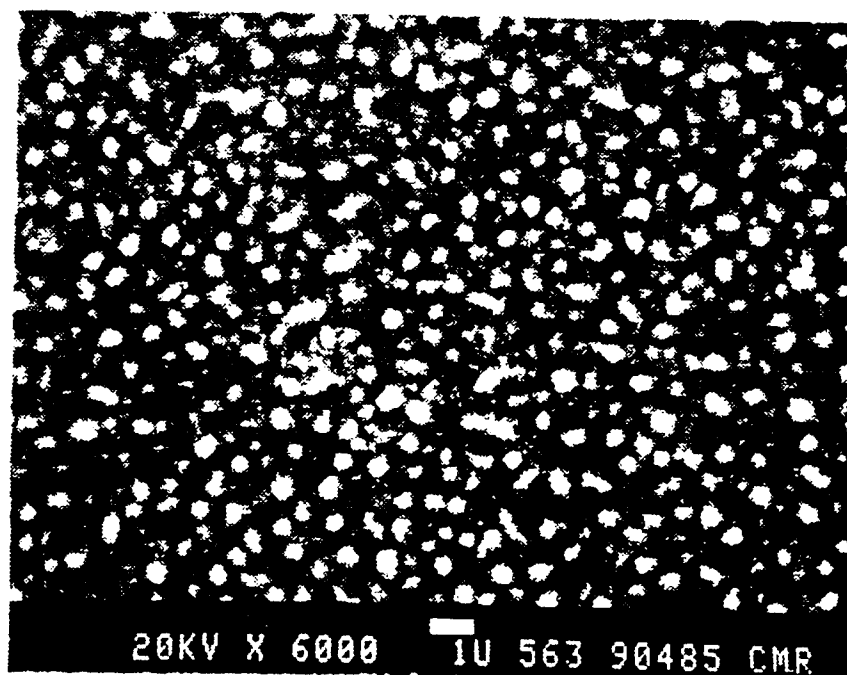


Fig. 5.16 Ag particles embedded in CuInSe_2 prepared by spray pyrolysis of CuInSe_2 onto Ag film at $\approx 300^\circ\text{C}$. SEM micrograph, white areas are Ag.

Chapter Six

Physical Properties and Applications of Random Composites

I. Introduction

The optical properties of small silver particles embedded in semiconductors will be presented in this chapter. The wavelength of interest in this investigation will be split into two main regions due to instrumental limitations. One is from 0.3 to 2.5 μm and the other from 2.5 to 20 μm . For $\lambda < 2.5\mu\text{m}$, a traditional spectrophotometer (in this work the Beckman Model DK-A ratio recording spectrophotometer) equipped with MgO- or BaSO₄- coated integrating sphere was used. The optical coating technology nowadays provides integrating sphere reliable only up to 2.5 μm due to characteristic optical absorptions of these oxides.[1-4] For $\lambda > 2.5\mu\text{m}$, we used a IBM-98 Fourier transform infrared (FTIR) spectrophotometer equipped with a diffuse reflectance accessory—model DRA 2-CI from Harrick Scientific Corp. In both regions the total transmission (T) and reflection (R) are measured and the absorption (A) is calculated from $A = 1 - T - R$. Consideration of diffuse reflection is important in this work due to the surface roughness of random composites.

In the Beckman spectrophotometer, a single beam is chopped into alternate reference and sample beams to provide a double beam system within the sample compartment. Both sample and reference beams have common detection and amplification components. Ratio recording (comparison of sample beam intensity with reference beam intensity) eliminates the inaccuracies due to such effects as source and amplifier gain fluctuations, sensitivity or spectral response of the detector and the presence of gases in the sample and reference beam paths. The detectors used are a photomultiplier for $\lambda < 400\text{nm}$ (0.4 μm) and a lead sulfide (PbS) cell otherwise.

In the FTIR spectrophotometer, only a single beam is used although the sample beam

intensity is referred to a reference beam intensity run at a different time. The sample compartment is in vacuum for reflection measurements while in N_2 ambient for transmission measurements. The detector used is HgCdTe operating at liquid nitrogen temperature. For our samples, transmission as low as one percent can be detected with rather good signal to noise ratio.

Optical functions $\mathbf{n} = n + i k$ and film thickness can be inverted by the so-called (R,T) method from the measured transmittance (T) and reflectance (R) of films with 1% or better accuracy as reported in the literature.[5-14] When multiple reflection of light in the film and substrate are significant, this inversion becomes a formidable job. The mathematics reduces to the solution of two simultaneous 4th order equation of n and nonlinear in k . [15,16] Analytical solutions obviously seem very difficult and numerical solutions also seem a nontrivial task. To understand the physical significance of the transmission and reflection of small particle composite thin films, here we have tried to evade that approach. We first calculate the optical constants of small particles of various microstructures based on the previously developed effective medium theory and then calculated the R and T. For a thin film, the multiple reflection of an electromagnetic wave between the interfaces of the film have to be included. The calculation and experimental results will be compared from which characteristic absorptions can be understood unambiguously.

II. Experimental Results and Discussions

Optical properties of ultrathin metal films and small metal particles have been extensively studied in the past two decades. Optical properties of Ag films less than 80\AA have been reported by S. L. McCarthy.[17] The anomalous optical behavior characteristic of a strong absorption has been associated with the particulate and aggregated island-like structure of films in their early stage of deposition.

Fig. 6.1 shows the optical absorption (A) of Ag films, as deposited at room temperature in the vacuum of base pressure 3×10^{-6} Torr, and mass thickness 200\AA and 300\AA respectively. Fig. 6.2 shows the corresponding absorptance of each film after 380°C vacuum anneal for 10

minutes. Both films appeared blue both by transmission and reflection. It also showed a little metallic luster when observed at oblique angles. As these films were heated, they change from blue to yellowish brown by transmission and reflection suggesting the absorption of blue and shorter wavelength light. This absorption peak around 3 eV and is shown in Fig. 6.2 for heated films.

As a comparison, Fig. 6.3 shows the work by McCarthy[17] where films are 40Å and 60Å thick respectively. It is understood that the particles broke up and regrew at new nucleation sites upon annealing at 350°C for at least 5 minutes. After annealing the particles became larger ranging from 50Å to 300Å in his baked films. Our samples show similar trends. The annealed samples demonstrate clear resonance peaks around 3 eV where the intensities are associated with the volume fraction, particle size and film thickness. The resonance frequency for the 200Å film appears to be higher than that of the 300Å film in agreement with previous reports[17] and is related to the higher volume fraction of the thicker film as discussed in Chapter IV on the optical properties of the S-1 photocathode.

In Fig. 6.4 we show the absorption of the Ag-Si multilayered composites with the structure of Si (200Å) / Ag (200Å) / Si (200Å) / Ag (200Å) / Si (300Å) / Sapphire substrate. Due to the 30% reflection at the surface of Si layer, the actual absorptance for Ag-Si composite film could be 50% higher in the absence of such surface layer or in the presence of an antireflection coating. But, in any event, the optical absorption in the Si energy band gap region has been greatly enhanced by about three orders of magnitude compared with the optical absorption coefficient of pure silicon. To understand this optical behavior, we now perform a simulation based on the effective medium theory discussed earlier.

From SEM studies in the previous chapter, we understand that the particle sizes range from a few hundred to two thousand Å's with central (mode) radius around 1000Å embedded in the matrix of polycrystalline silicon. In Fig. 6.5 we plot the absorptance of a system with mode particle size $R_m = 1000 \text{ Å}$ (see Chapter IV) and particle size distribution number $\alpha = 10$

corresponding to sizes ranging roughly from about three hundred to two thousand Å's. The Ag particle volume fraction is 50% and the Si dielectric constant is taken as 12 in the infrared region of our concern. In this plot we include two curves, one with 2% (f_2) of aggregated Ag and the other with no aggregation ($f_2=0$). Obviously, the one with 2% fits the experimental better. We see a kink at about $1\mu\text{m}$ and two peaks at $1.4\mu\text{m}$ and $2\mu\text{m}$ respectively. As we remove the 2% of aggregated Ag particles, the peak at $2\mu\text{m}$ disappear while the kink and the peak at $1.4\mu\text{m}$ remained. This tells us that the $2\mu\text{m}$ peak is associated with the second microstructural unit or, in other words, the aggregated Ag particles.

Now, we need to know where the first unit peak is. To this end, we plot in Fig. 6.6.a and 6.6.b the dielectric constants of such films ($f_2=0$ and 2% respectively). We find that, indeed, at $2\mu\text{m}$ there shows a typical fluctuation in ϵ_1 and a bump in ϵ_2 when $f_2=2\%$. However, the prominent resonance peak occurs not at $1.4\mu\text{m}$ but rather at close to $1\mu\text{m}$ where the absorptance does not show a peak but rather a broad-band absorption takes place below $1\mu\text{m}$.

This result is due to interference effects of the multiply reflected electromagnetic waves in this composite thin film as will be explained in the following. For a thin film whose thickness H is the odd multiples of a quarter wavelength in the material, i.e., $H = (2m+1)\lambda_0/4n_1$, where m is an positive integer and λ_0 is the vacuum wavelength of probing wave, the reflectivity is maximum or minimum depending upon whether the refraction index n_1 of the thin film is greater or smaller than the previous medium.[15] For the present case, the film has refraction index greater than one ($n_1=1$ for vacuum) and therefore the maximum reflections occur as $H = (2m+1)\lambda_0/4n_1$ and the minimum reflections occur as $H = m\lambda_0/2n_1$ for any positive integer m . Maximum absorption will therefore occur when $H = m\lambda_0/2n_1$, or when thickness is the even multiples of the quarter wavelength. If $M=4n_1H/\lambda_0$ is plotted against λ_0 , maximum absorption due to interference will be observed for $M=2,4,6\ldots$ etc. As shown in Fig. 6.7 where M is plotted as a function of λ_0 for the 1100\AA film, such condition are found satisfied at $\lambda_0 = 0.2\mu\text{m}, 0.3\mu\text{m}, 0.4\mu\text{m}, 0.8\mu\text{m}, 1.05\mu\text{m}$ and $1.4\mu\text{m}$. The absorption peak at $1.4\mu\text{m}$ is therefore due to interference. The broad-band

absorption below $1\mu\text{m}$ is a result of superimposed absorption due to the interference absorption in the film at 0.3 , 0.4 and $0.8\mu\text{m}$ on top of the first microstructural unit (or isolated Ag particles) resonance absorption at $1\mu\text{m}$.

It is now clear that as the thickness is varied in such a way as to match the phase relation of the probing wave at the two interfaces of the composite thin film, the effective optical path is increased and the absorption is thus enhanced. We therefore prepared films of microstructure similar to the previous sample except for the increased thickness— $1\mu\text{m}$. The alternating layers of Si (200\AA for 21 layers) and Ag (200\AA for 20 layers) are in similar sequence.

Fig. 6.8 shows the absorptance of such a film from $\lambda_0 = 2.5\mu\text{m}$ (4000cm^{-1}) to $20\mu\text{m}$ (500cm^{-1}). Among the many peaks we now would like to identify their interference nature. We do so by calculating the absorptance of films with $H = 1\mu\text{m}$, leaving other microstructural variables as adjusting parameters. We will be dealing with wavelengths in a broad range from submicron to $20\mu\text{m}$, and the Drude model will be assumed for bulk Ag metal whose dielectric constants for $\lambda_0 > 2\mu\text{m}$ can be calculated as described in Eqn. (2.1) of Chapter Two. The dielectric functions of small silver particles are then obtained from Eqns. (2.1) to (2.4).

We will be choosing a number of microstructural parameters for a composite film to calculate its optical properties. The match between theory and experimental data can be achieved through the variation of these parameters. This approach gets around the (R,T) method mentioned previously where one has to undertake a formidable job of inverting the optical measurement of reflection and transmission data to n and k as functions of frequencies.

Table I gives the sets of parameters used in this calculation. The results are plotted in the figures as numbered.

From these calculations we have been able to interpret the absorption peaks for the $1\mu\text{m}$ film shown in Fig. 6.8. Prominent peaks at $1/\lambda_0 (\text{cm}^{-1}) \approx 850, 1700, 2550, 3400$, and 4250 or $\lambda_0(\mu\text{m}) \approx 11.9, 5.9, 3.9, 3.0$ and $2.4\mu\text{m}$ are related to the interference with $M = 2, 4, 6, 8$ and 10 , respectively. For a $1/2\mu\text{m}$ film, only $M = 4, 8, 12\ldots$ are possible as can be seen from a

comparison between calculations #2 and #12. In Fig. 6.9.1 the absorption peaks occur when $M = H/(\lambda_0/4n_1) = 2,4,6,8,10$ at $\lambda_0 = 12.2\mu\text{m}$ (820cm^{-1}), $6.0\mu\text{m}$ (1650cm^{-1}), $4.0\mu\text{m}$ (2500cm^{-1}), $3\mu\text{m}$ (3300cm^{-1}), $2.46\mu\text{m}$ (4080cm^{-1}) for a $1\mu\text{m}$ film without aggregation of Ag particles ($f_2=0$) with size varying from 300\AA to 2000\AA . These peak positions calculated have been fairly close to the ones observed experimentally for the $1\mu\text{m}$ film of Fig. 6.8. The $12.2\mu\text{m}$ absorption is of the first order interference corresponding to $m=1$ (i.e. $M = 2$) and the $6.0\mu\text{m}$ peak is the second order one with $m=2$ or $M=4$, and so on so forth.

Table I

#	H	D	α	P	f_2	Fig. #
1	$1\mu\text{m}$	1000\AA	10	50%	0%	6.9.1 (oooo)
2	$1\mu\text{m}$	1000\AA	10	50	2	6.9.2
3	$1\mu\text{m}$	1000\AA	10	50	20	6.9.3 & 6.9.4
4	$1\mu\text{m}$	1000\AA	10	50	30	6.9.3
5	$1\mu\text{m}$	1000\AA	10	50	40	6.9.3
6	$1\mu\text{m}$	1000\AA	10	50	50	6.9.3
7	$1\mu\text{m}$	1000\AA	10	60	0	6.9.1 (xxxx)
8	$1\mu\text{m}$	1000\AA	single size	50	0	6.9.5
9	$1\mu\text{m}$	100\AA	Single size	50	0	6.9.6
10	$1\mu\text{m}$	30\AA	Single size	50	0	6.9.7
11	$1/2\mu\text{m}$	1000\AA	Single size	50	2	6.9.8
12	$1/2\mu\text{m}$	1000\AA	10	50	2	6.9.9

When the degree of segregation increases to $f_2=2\%$, as shown in Fig. 6.9.2, the void resonance (i.e., the second unit peak) at $2\mu\text{m}$ starts to intrude on the long wave regime and superimpose itself onto the interference peaks and the peak of $M=12$ at 4900cm^{-1} (i.e., 6th order

interference with $m=6$) disappear completely as seen from the comparison between Figs. 6.9.1 and 6.9.2. The absorption maxima have red shifted. In this figure we also plot the transmission and reflection for such a film to show its interference characteristics. The five absorption maxima counting from the right correspond to $M=2, 4, 6, 8$, and 10 respectively. The reflection is minimum when the absorption is maximum. Also note that included in Fig. 6.9.1 are the absorptions when volume fractions p 's are 50 and 60%, respectively. Absorptions are shifted toward longer wavelength as p increases. This red shift is due to the higher polarizability for higher volume fraction of particles reflected in the larger refraction index n_1 . Since the wavelength in the film is smaller if n_1 is larger, there are more interference modes in the same frequency interval at higher p (7 maxima vs. 6 maxima for 60% vs. 50%) between 5000 and 500 wavenumber (cm^{-1}). In the mean time, the effective optical path in the film is now longer, and the absorption peak intensities also increase as a result of increasing p .

As f_2 increases further from 2% up to 50%, the second unit peak broadens more and more from $2\text{ }\mu\text{m}$ into the longer wavelength regime. This void resonance absorption gradually dominates the optical absorption mechanism over the interference absorption as soon as the broadening runs into the associated interference peak. The higher order interference thus begins to disappear first as f_2 increases gradually. At $f_2 = 50\%$ the interference phenomenon vanishes totally. This is shown in Fig. 6.9.3.

The decrease in absorption as f_2 increases is due to the increasing reflection from these films. As f_2 goes up, the composite system becomes more and more percolated approaching an "porous metal". The electrons thus become less confined and the void resonance starts decaying. The high reflectivity is shown in Fig. 6.9.4 for $f_2=20\%$ where absorption (A), transmission (T) and reflection (R) are included. Note that in Fig. 6.9.3 the absorption above $5\text{ }\mu\text{m}$ is less than 25% for $f_2 = 50\%$ in which case almost 75% of the incident wave is reflected.

So far we have only considered particles distributed in size between 300\AA and 2000\AA . For single size particles, both the void resonance and the interference occur at longer wavelength

although weaker in intensity as compared with distributed particle sizes as will be shown later in the Figs. 6.9.8 and 6.9.9. From Figs. 6.9.5 - 6.9.7, we show the particle size effects on the resonance and interference. The line shapes for smaller particles are broader due to the lifetime effect. For 1000Å particles, the peak intensities seem to obey the principles that higher order interference give rise to longer optical paths and therefore larger absorption. For smaller particles 30Å and 100Å in diameter, this rule does not seem to be observed. These two sizes differ from one another in peak intensities and width but not in peak positions. On the contrary, their peaks occur at longer wavelength than that of the 1000Å particle system and the corresponding peak intensities of theirs are stronger.

Figs. 6.9.8 and 6.9.9 show the absorption of a $1/2\mu\text{m}$ film with single particle size and 300-2000Å distribution, respectively. First we see that, as expected and discussed before, the number of maxima is reduced by a half. Only $M=4, 8, 12 \dots$ etc. satisfy the interference conditions. Again the bump below $2.5\mu\text{m}$ (above 4000cm^{-1}) is also due to the void resonance of aggregated Ag particles. The film with single size shows maxima at longer wavelengths although the intensities are weaker. Furthermore, the refraction index of the single particle size film is higher since the inter-peak distance is smaller in this film.

These calculations are used to understand the optical behavior of the films we have prepared. Obviously enough, microstructure has crucial effects on the optical properties of composite films. To account for the exact origin of the absorption peaks, one has to look carefully into the effects of individual parameters. This is by no means trivial since our films are deposited on sapphire substrates whose optical behaviors above $5\mu\text{m}$ are not featureless and therefore may have caused some inaccuracy in the exact match between the calculations and experimental data. Nonetheless, in general we are able to fit the experimental values with a set of microstructural parameters. What is interesting is that the interference absorption can occur over a wide range of wavelength with fairly high intensities. These characteristics imply that these materials are potential candidates for applications in interferometry, filters, antireflection coatings, selective band optical detector in

photothermal mode and many other applications over a wide range of infrared spectrum. To serve different wavelength ranges one needs to tailor adequate thickness and small particle configurations. With all these knowledge, combinations of different metal species and semiconductors then become subjects of further research to seek materials of desired properties. For example, Ag-CuInSe₂ system prepared by spray pyrolysis of CuInSe₂ onto ultrathin Ag films demonstrated stimulating properties without chemical compound formation between the Ag metal and the ternary semiconductor compound.

Fig. 6.10 shows the optical absorption coefficient of such a system and a bare CuInSe₂ film prepared under the same condition (the same batch). Since CuInSe₂ is a direct band gap material, we plot α^2 vs. $h\nu$ to deduce the band gap or photoexcitation barrier of these films. It is found that the composite film show unambiguous band gap close to 1eV as it should be while the bare CuInSe₂ film shows second phase of CuSe₂ whose band gap is around 2.2 eV as can be deduced from this plot. Life may not be as complicated as it appears, although a lot of complications can arise when it is resorted to semiconductor compounds for host matrix materials.

III. Proposed Future Research and Applications for Photon Detection

The structure of the Si matrix in the materials synthesized so far has been either amorphous or polycrystalline which showed relatively low carrier mobility on the order of 1-10 cm²/V-sec as compared to 10 and 1000 cm²/V-sec for a-Si:H and intrinsic Si single crystals, respectively.[11] Hydrogenation of Ag/a-Si thin film appeared to produce anomalously high Hall mobilities which suggests a need to look more careful into the electric transport mechanism in small particle systems in order to understand the parameters controlling the efficiency of collecting photoelectrons from these metal particles. To do so, we need also to have better control of film qualities to avoid any complications from unknown material parameters such as the semiconductor grain boundaries in Ag-polysilicon. In the upcoming years, we thus propose to focus on growing composites of epitaxial silicon films embedded with small Ag-particles to reduce material factors mentioned

above.

The electrical transport mechanism between metal particles has been studied by some authors[18,19] and are believed to obey tunneling or hopping mechanism, as sketched in Fig. 6.11. Electrons in the metal particles tunnel from one particle to another at an applied field and move inside the particles in a conventional way.[18] Conductivities of small particles in vacuum or in insulators have also attracted great attention in the past few years. Many studies have been concentrated on the percolation theory of small particles but only a few on the DC and AC measurements of metal-semiconductor composites.[20-27]

The difficulties behind the electric property studies are probably due to the limited control of the quality of junction interfaces between small metal particles and semiconductor matrices. Contact properties are therefore important issues before an unambiguous knowledge of electron transport process can be obtained. The roles of Schottky junctions and the defect states in the junction areas have to be better understood. Materials of various microstructures therefore need to be prepared under controlled conditions and their electrical properties including the dark and photoconductivities, dielectric response, Hall mobility, thermoelectric power and many others have to be related to the microstructural variations.

For photon detection applications, we first need to consider surface and interface recombinations of free carriers and the supply of carriers from electrodes after electrons are knocked out of the small metal particles. Defect state assisted or phonon assisted tunneling is not an efficient way of electric transport as compared with conduction electron transport. One example is that through phonon assisted hopping between localized defect states, carrier mobility can only be on the order of milli- or even micro- $\text{cm}^2/\text{V}\cdot\text{sec.}$, while conduction electron transport due to the extended states are much more efficient with $10 \text{ cm}^2/\text{V}\cdot\text{sec.}$ for amorphous silicon.[28,29] For fast photoelectron collection we therefore wish to have the photocarriers transport in the semiconductor matrix rather than through metal particles.

Recently, there have been studies on the instability of small particle structure suggesting that

the coulombic force induced by charge accumulation may result in structural fluctuation.[30,31] Electrical conductivity measurements of small gold particle systems show that atomic rearrangements at the surface may be the reason for huge noise-like conductivity as a function of time.[32] They found that as hydrogen, carbon mono-oxide or oxygen streams were introduced, the fluctuations in conductivities can be suppressed by the adsorption of these gas molecules. They attributed this suppression to the stabilization of structure – a kind of surface passivation to reduce the coulombic interactions between charged metal particles as fields are applied across them. The significance of this effect on the electrical transport properties of our films is not clear. One should not ignore the contact phenomena at the semiconductor and small metal particle interfaces which, in fact, might be barriers to practical device applications.

For photodetection applications, three devices are proposed below based on (1) shallow p-region p-n diodes with lightly doped p-region embedded with small particles sitting on an n-region, for which the band diagram is shown in Fig. 6.12, (2) composite Ag-Si/Si multilayered structure as shown in Fig. 6.13, and (3) n-channel MOS device with small metal particles embedded in the p-substrate as shown in Fig. 6.14.

Device (1) will be fabricated via solid phase epitaxial (SPE) growth by depositing Ag_xAl_{1-x} alloys, whose compositions are specified according to the desired volume fractions of Ag particles, on n-Si followed by a layer of a-Si on the top. From the previous works[12-13] on the SPE growth of p-Si epitaxial layer using Al-metal and our results on Ag-Si which indicated that Ag atoms preferred not to outdiffuse through the Si-layer to the free surface, we predict that the annealing of such a structure at 500°C for 1/2 - 1 hour will result in device structure(1). Al-atoms will outdiffuse and then trade place with Si-atoms leaving Ag-atoms behind to cluster and form small particles. The outdiffused Al-layer on the top as a result of annealing will then be etched off. The epi-layer is going to be p-type due to Al-doping. The doping level is to be controlled by surface damaging with high energy ions followed by a gettering process. The mechanism of photodetection is through the photoexcitation of electrons from the silver into the p-region which

then diffuse to the depletion region generating a voltage (i.e., photovoltaic mode). Device (2), similar to device (1), uses the layers of Ag-Si composite as electron source and the Si-layers as carrier transport channels. It will be fabricated by the sequential epitaxial growth of these two types of alternating layers, the etching and gettering of Al.

To obtain some idea of how efficient these devices can be, we plot in Fig. 6.15 the theoretical quantum yield, according to our theory of photoemission[7], for the internal photoemission of electrons from Ag into Si where the barrier height is 0.6eV. Since Ag has high electron density of $6 \times 10^{20} \text{ cm}^{-3}$, a quantum yield of 0.1-1% at 1-2 μm still gives 10^{20} cm^{-3} photoelectrons, corresponding to an excitation from heavily doped semiconductors. Extrinsic semiconductors, however, suffer from serious dark current problem[14] which we do not encounter in our devices. The high quantum efficiency of the Ag-Si composite will therefore provide large signal to noise ratio, which, together with the fast response of metal-semiconductor junctions, will make a high efficiency optical detector operating at room temperature in photoconductive and photovoltaic modes.

Similarly, device (2) also makes use of small metal particles as photoelectron source. The composite layers provide photoelectrons which transport in the pure semiconductor layers and are collected therein. Due to the higher mobility in the semiconductor layer as a result of less scattering, the photo-efficiency will be higher. This concept is similar to the multilayered III-V compound semiconductor devices where layers of higher band gap materials are heavily doped and lower band gap materials remain intrinsic. The heavily doped layers suffer from more impurity scatterings and therefore have low mobility but they provide high density of free carriers which transfer into and travel in the high mobility quantum wells, due to less scatterings, of intrinsic semiconductor.

In devices (3), when a gate voltage V_G is applied between the gate and the substrate (ground) of a n-MOS device, the conduction channel is inverted from the p-substrate into a n-type channel if V_G is greater than the threshold voltage.[29] The electrons transport from the source to the drain

via the n-channel. When light is illuminated, photoelectrons from metal particles in the p-substrate will diffuse into the inversion layer and participate in the electrical transport. Optical signals are converted this way into electronic ones.

Furthermore, for modern fiber optic communication applications, Si p-i-n photodiodes have been widely used in short wavelength systems of 0.8 to 0.9 μm for short distance communications. The p-i-n diodes, with their high bandwidth and low noise, are promising for the next generation of fully integrated optical detectors. In the intrinsic layer, one can introduce small metal particles to enhance the carrier generation rate and therefore increase the sensitivity even further.

In conclusion, further research will be to fabricate practical devices for photodetectors and extend our understanding of the relationships among the electric transport properties, optoelectronic properties and the microstructures of these devices. X-ray diffraction, TEM, SEM, XPS, UPS and sputter Auger techniques are needed for microstructural characterizations. Transport studies need to involve the Hall mobility, temperature dependent conductivity and photoconductivity measurements. I-V and C-V investigations including DLTS and AC-conductivity measurements need also be conducted to determine the electrical and electronic properties. Various other physical properties such as the Seebeck effect should also be measured in order to widen the application fields of such materials and devices.

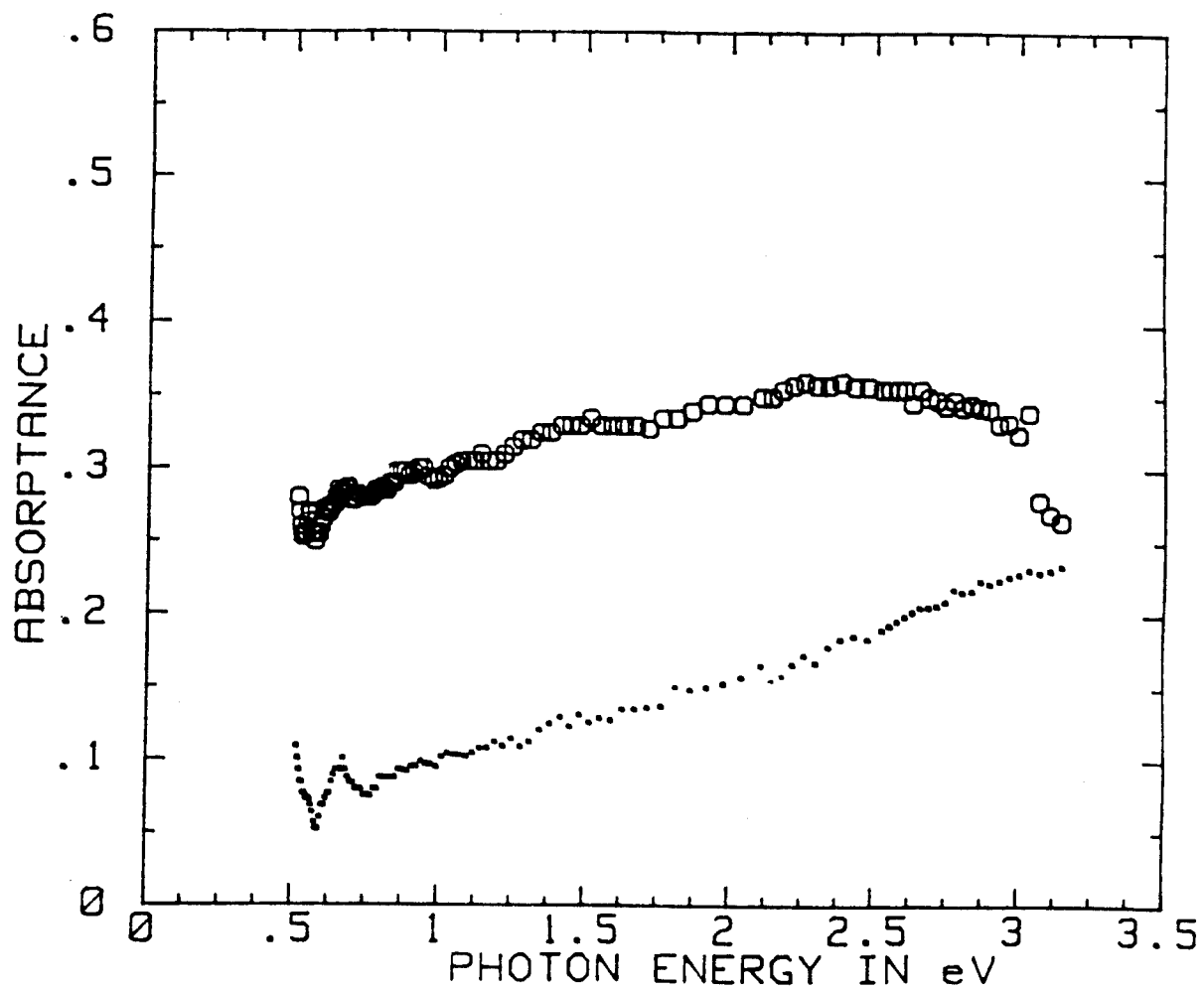


Fig. 6.1 The optical absorption of particulate thin silver films of mass thickness 200 Å (●) and 300 Å (○), respectively, deposited at R.T.

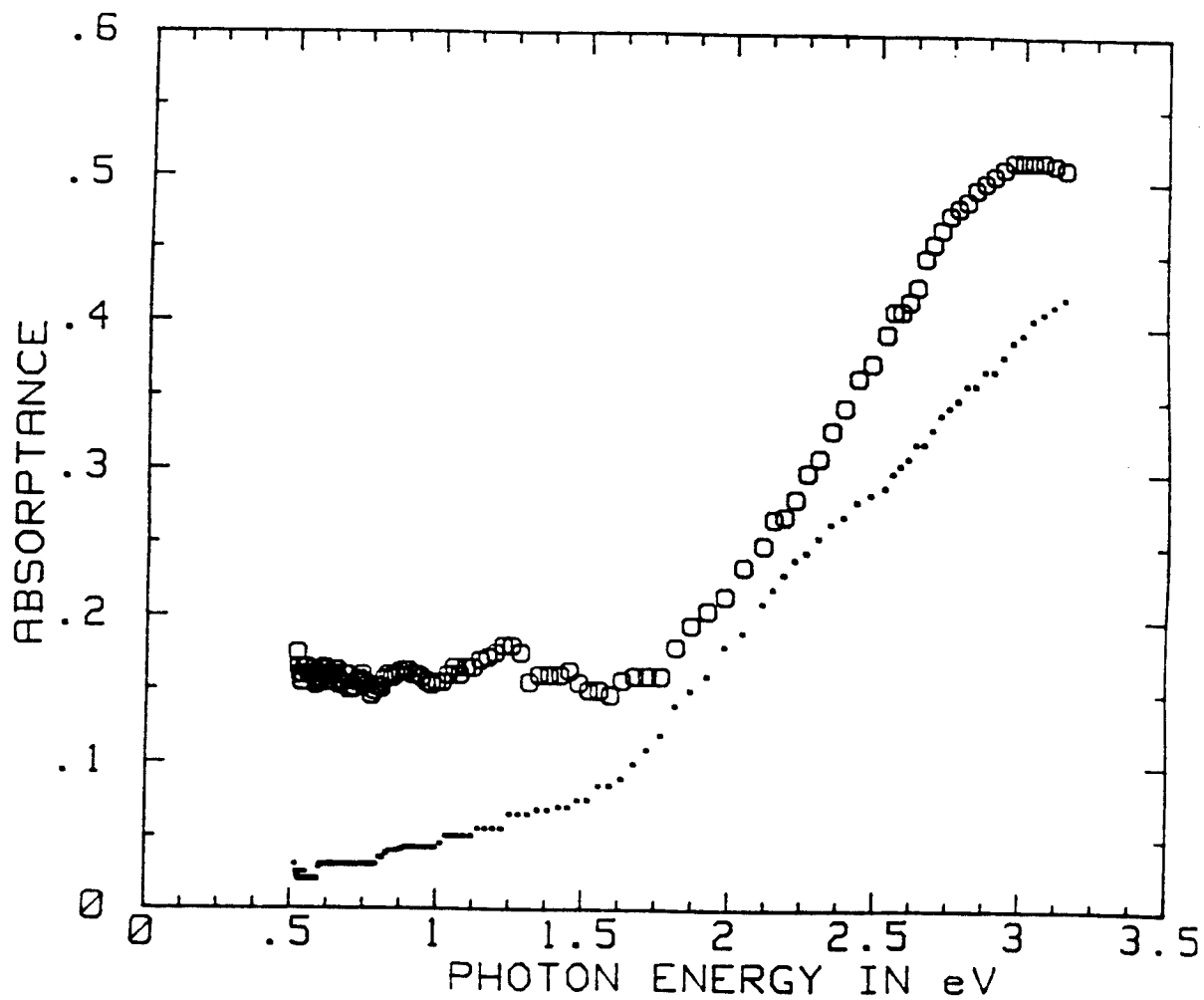


Fig. 6.2 Samples of Fig. 6.1 annealed at 380°C for 10 minutes. The 200Å film show broader peak at higher frequency.

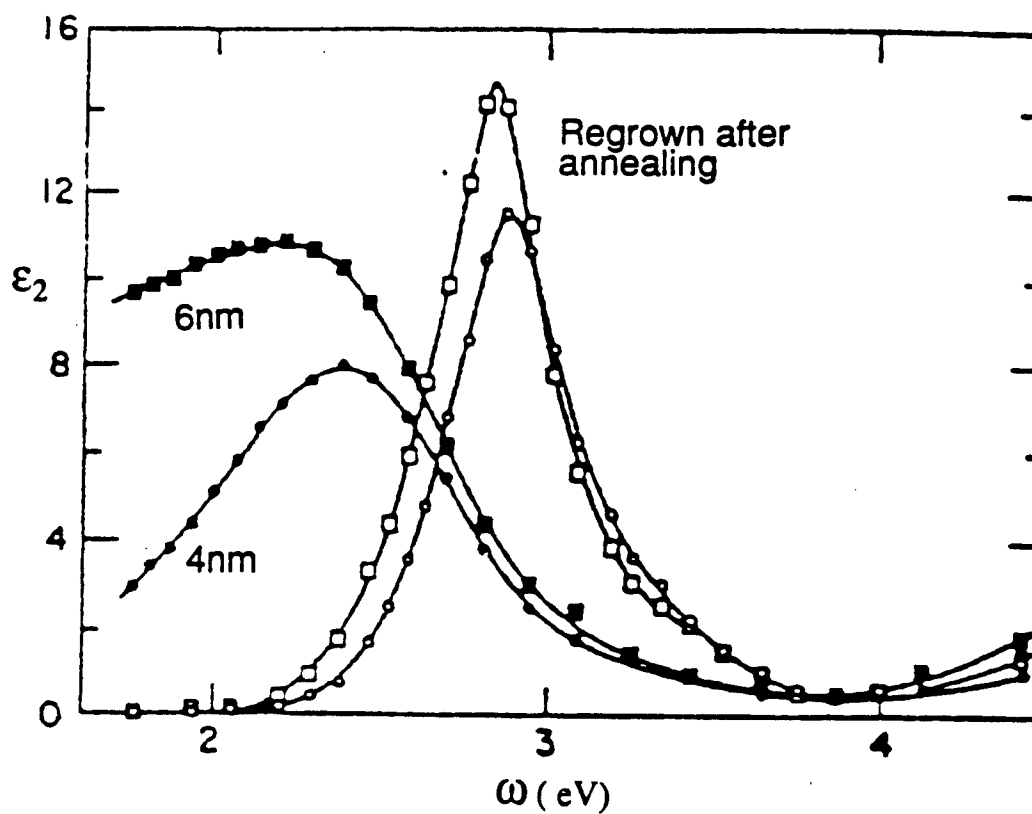


Fig. 6.3 ϵ_2 vs. frequency for two films with 4nm and 6nm mass thickness (●, ○—4nm; ■, □—6nm.) Open points are baked films.[from 17]

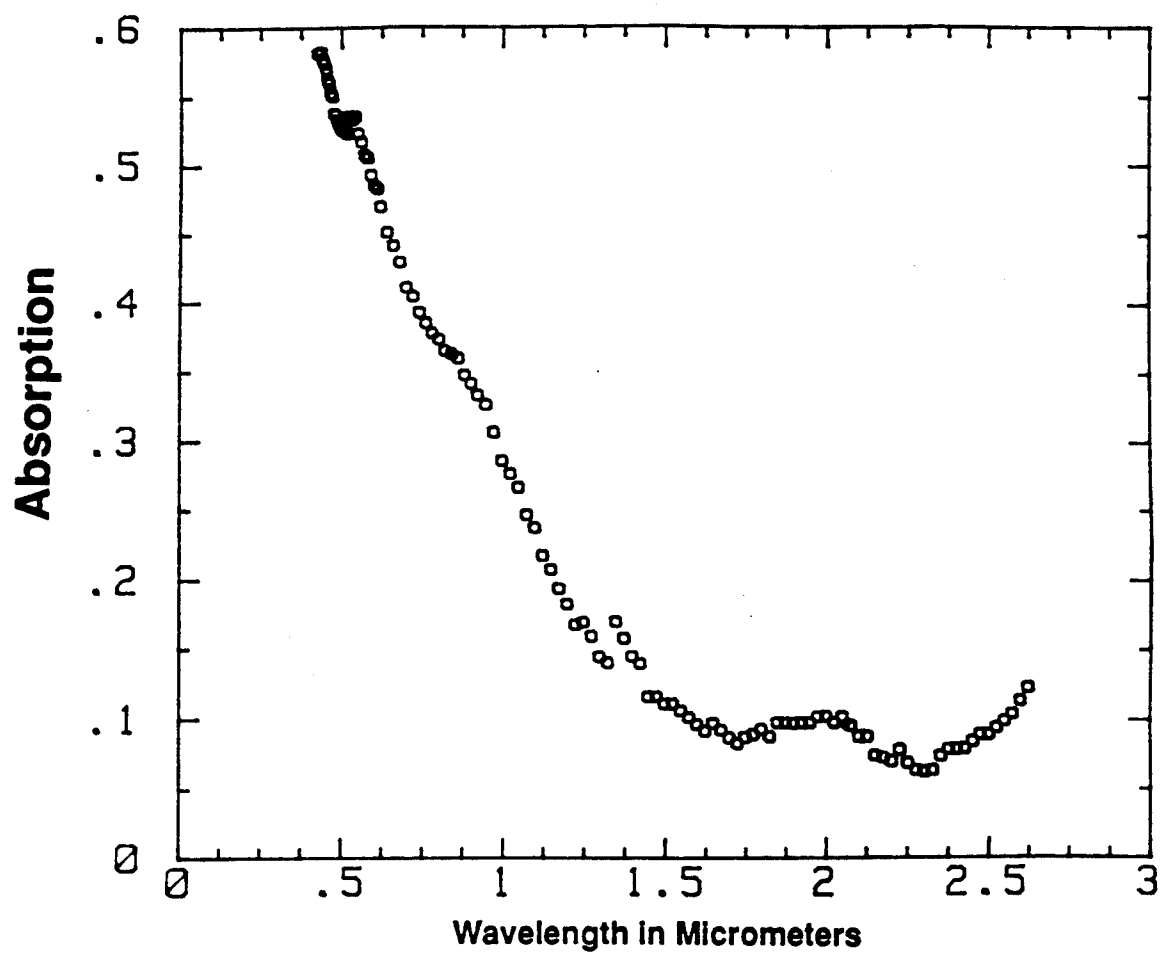


Fig. 6.4 Absorptance of a Ag-Si film tandem deposited at 600°C. Particle shapes are irregular and sizes range from a few hundred to two thousand Å's, with central radius $\approx 1000\text{Å}$.

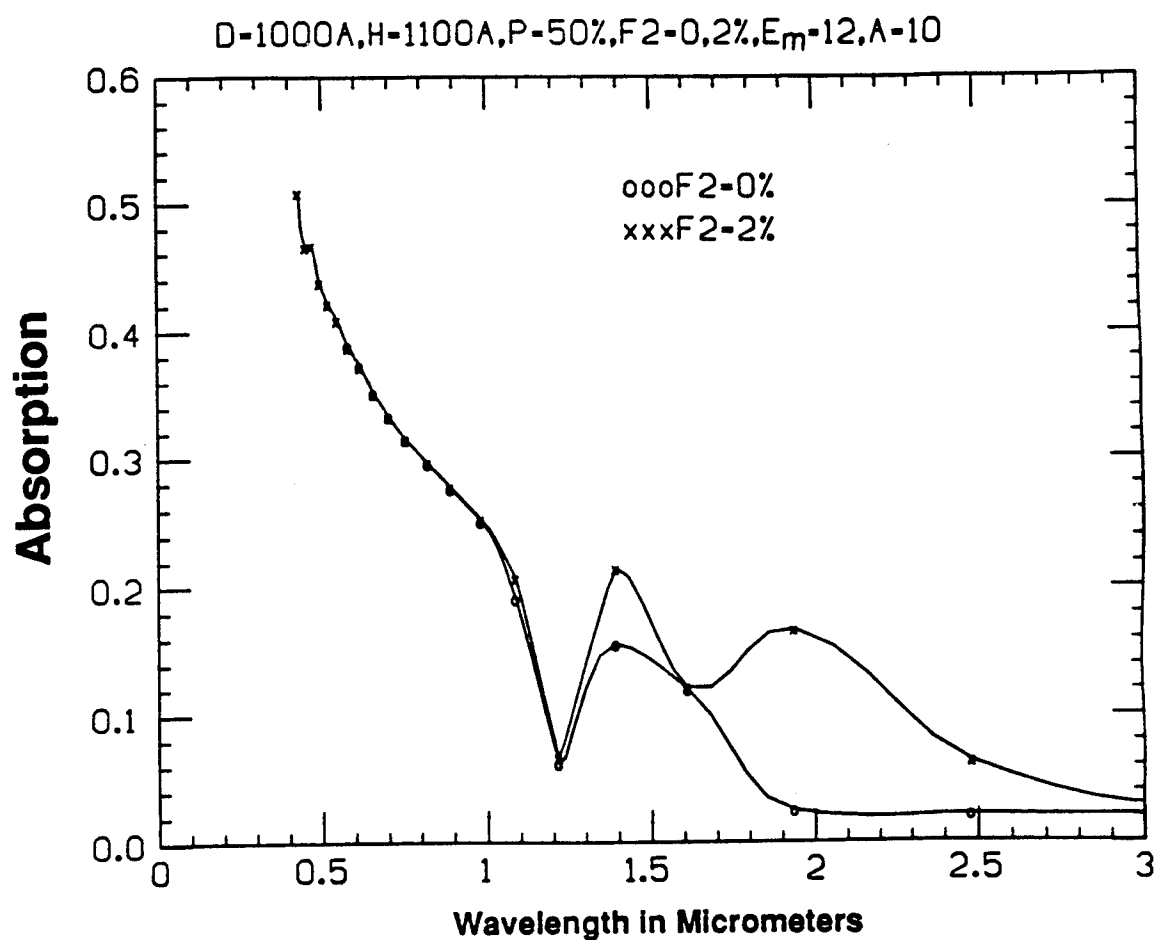


Fig. 6.5 Calculated absorption of small Ag particles with microstructural parameters as indicated. D, H, P, F2, ϵ_m and Λ are as defined in Fig. 4.2, Chapter IV. $\epsilon_m = \epsilon_m$ $\Lambda = \Lambda$

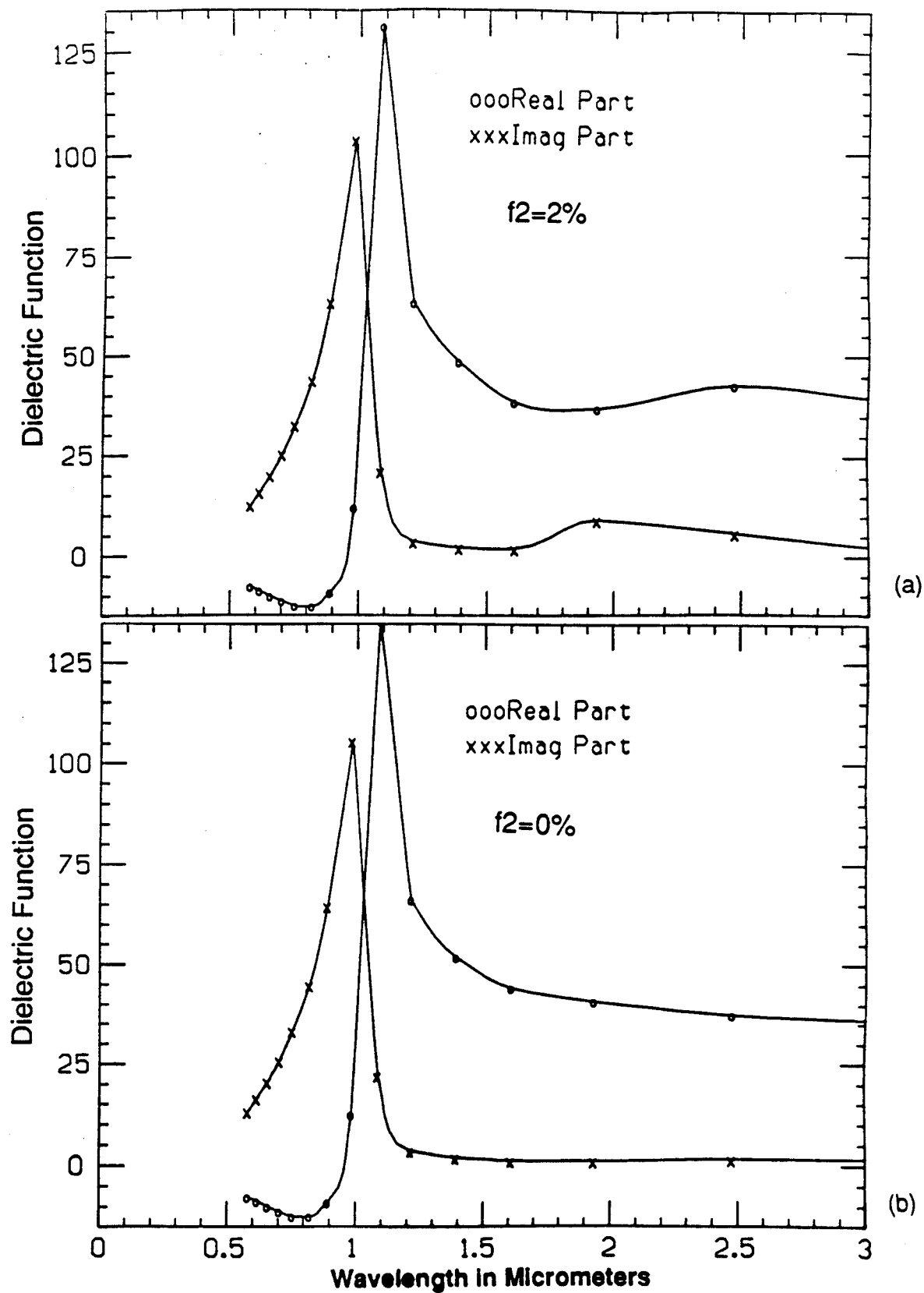


Fig. 6.6 Comparison of ϵ_1 and ϵ_2 for two small Ag particle systems.
(b) without and (a) with second microstructural units.

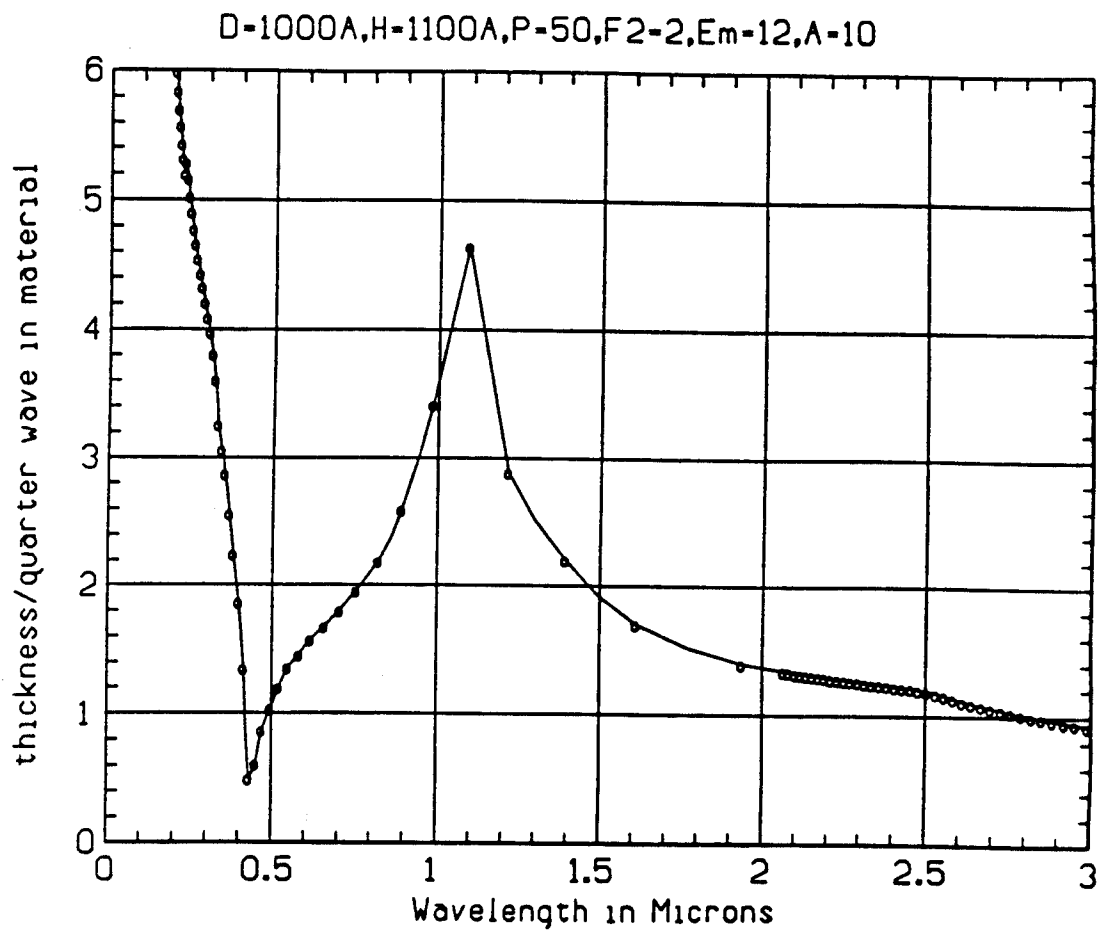


Fig. 6.7 Plot of thickness-quarter wavelength ratio vs. wavelength.
Constructive interference occurs as the ratio is an even integer.

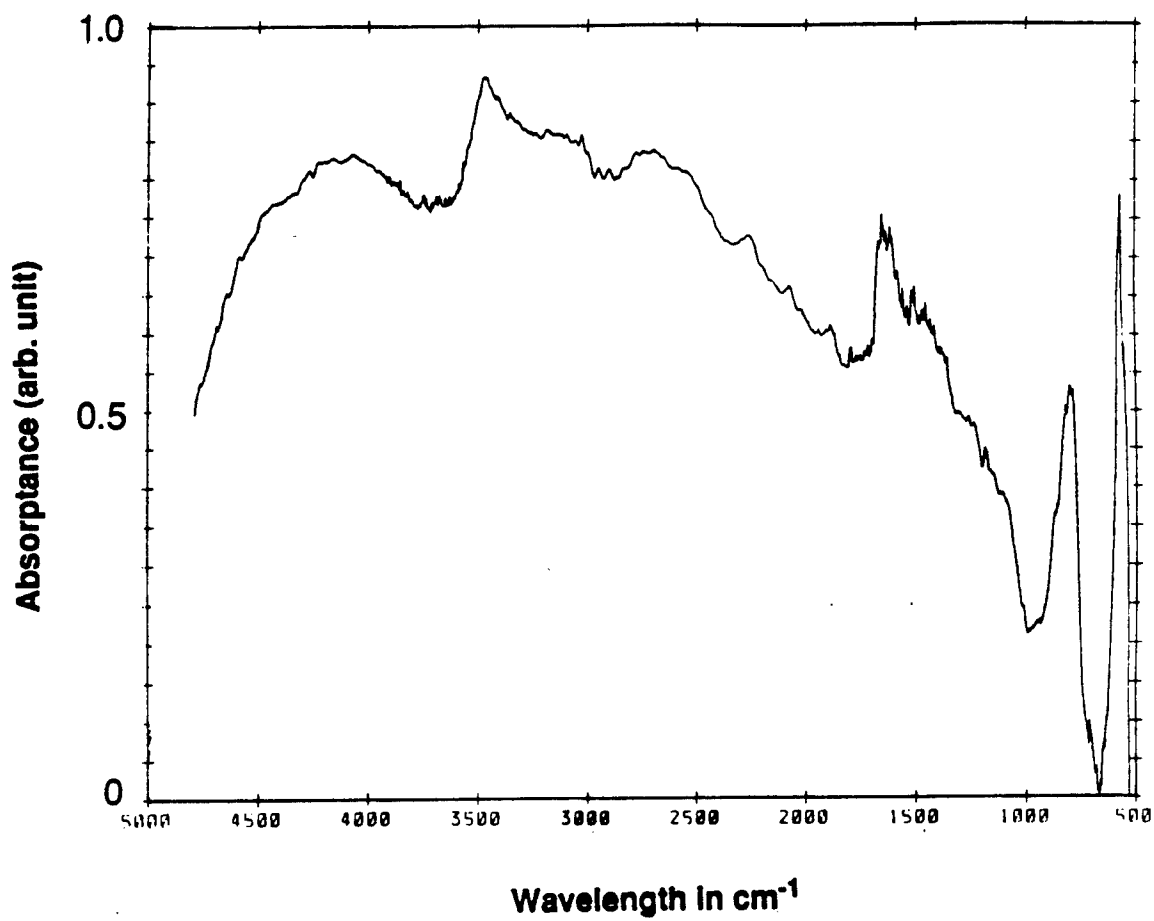


Fig. 6.8 Absorption of a tandem deposited Si-Ag film(1 μ m thick and deposition temperature is 700°C).

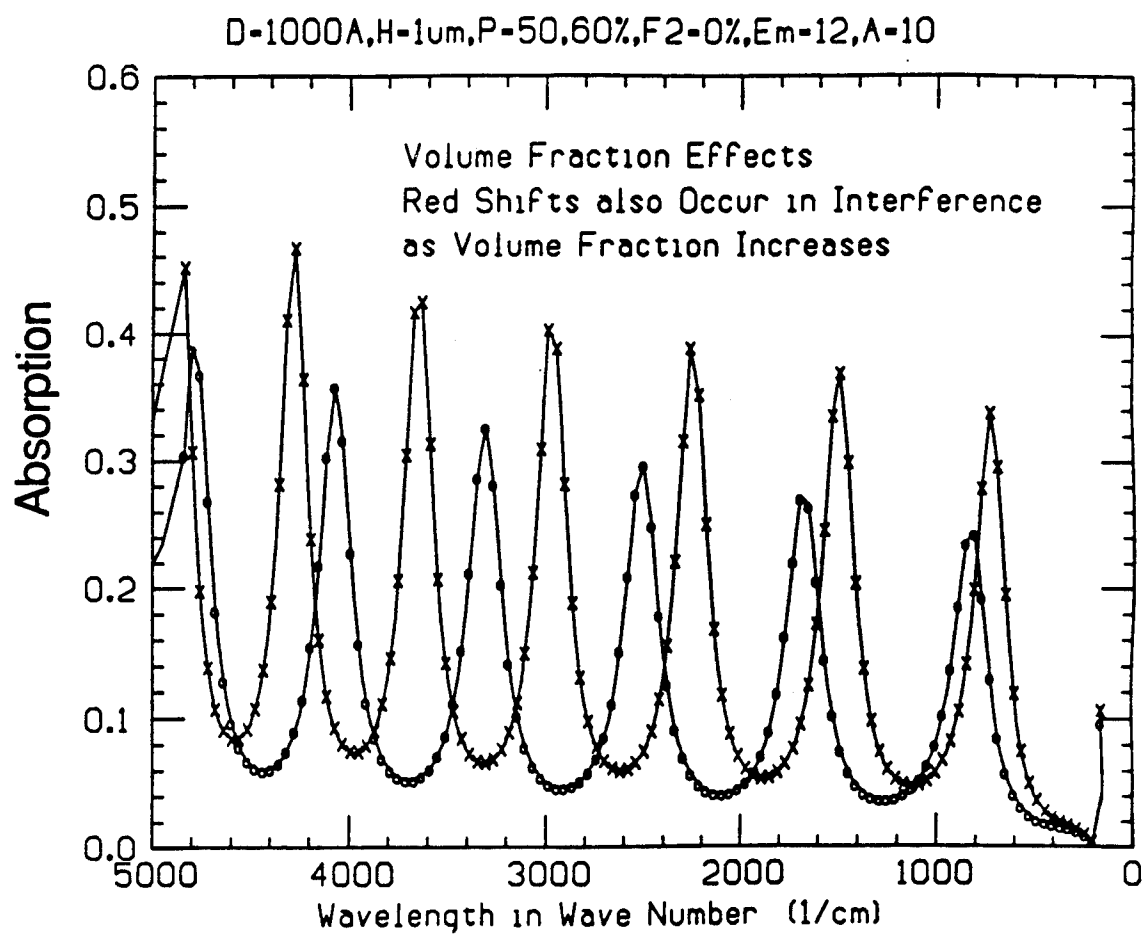


Fig. 6.9.1

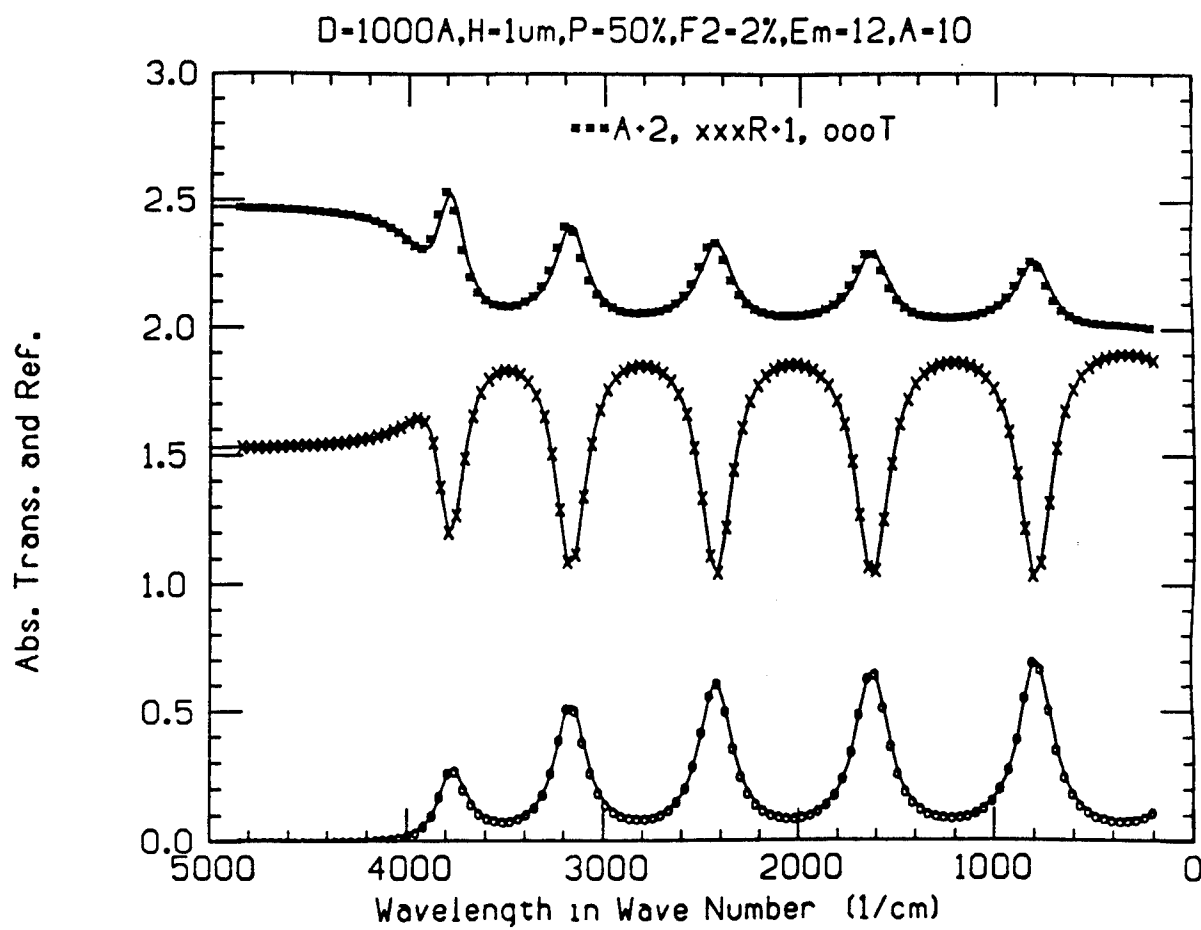


Fig. 6.9.2

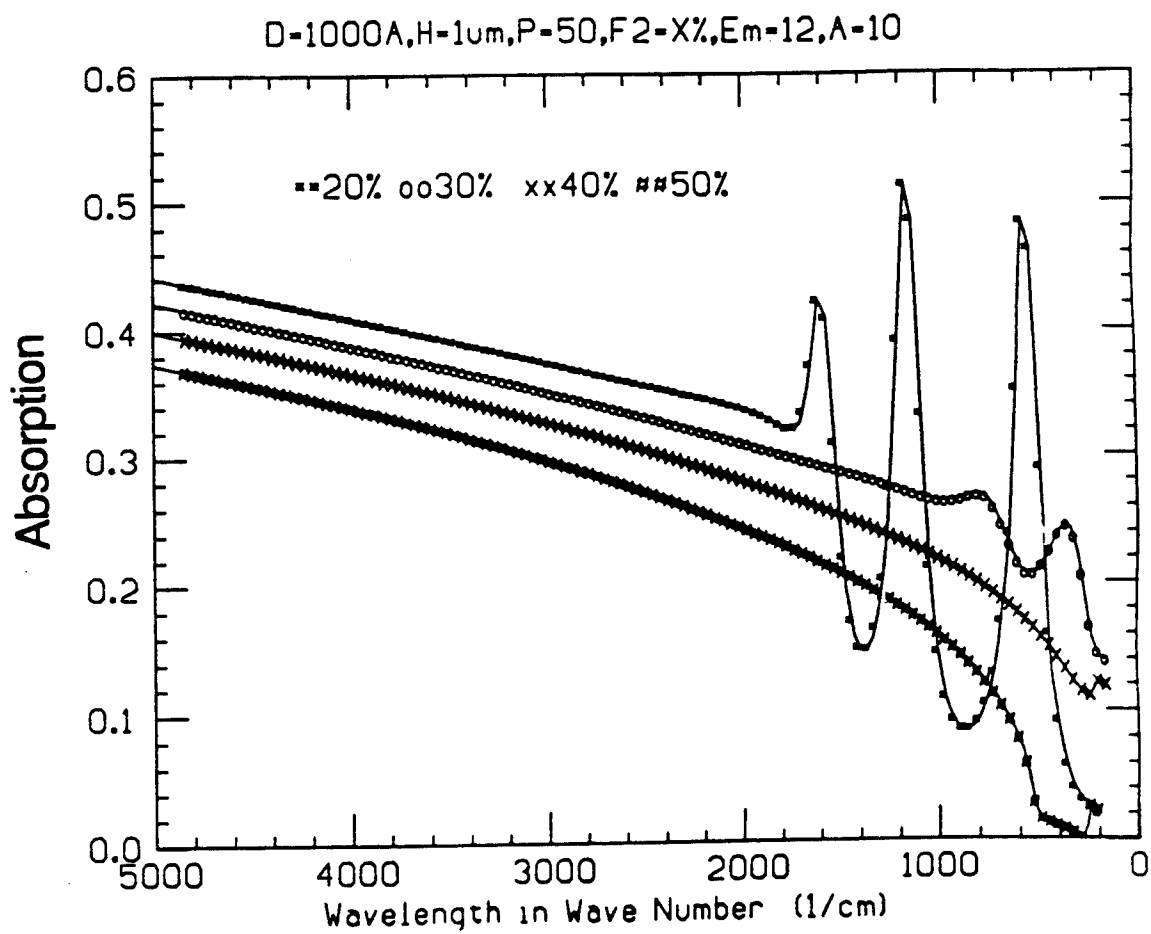


Fig. 6.9.3

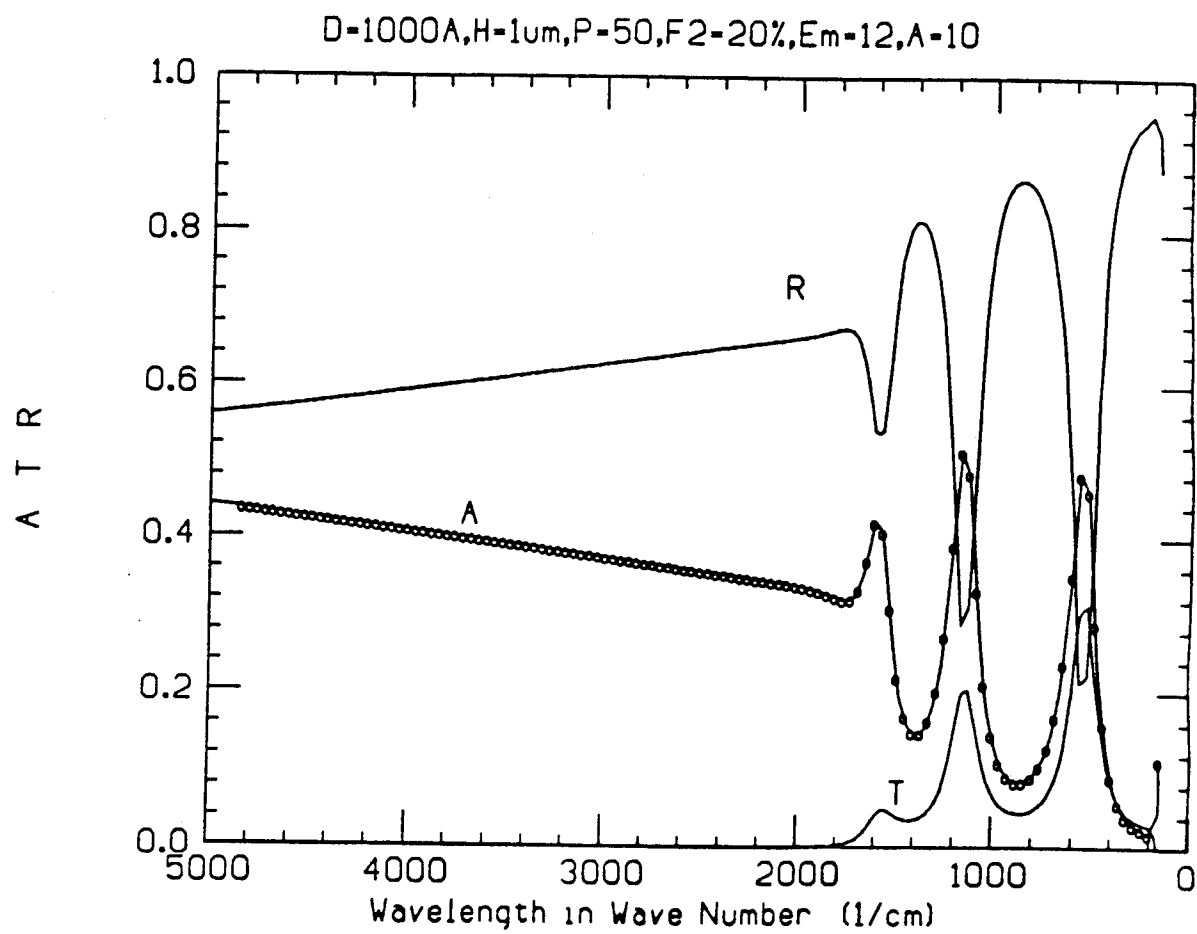


Fig. 6.9.4

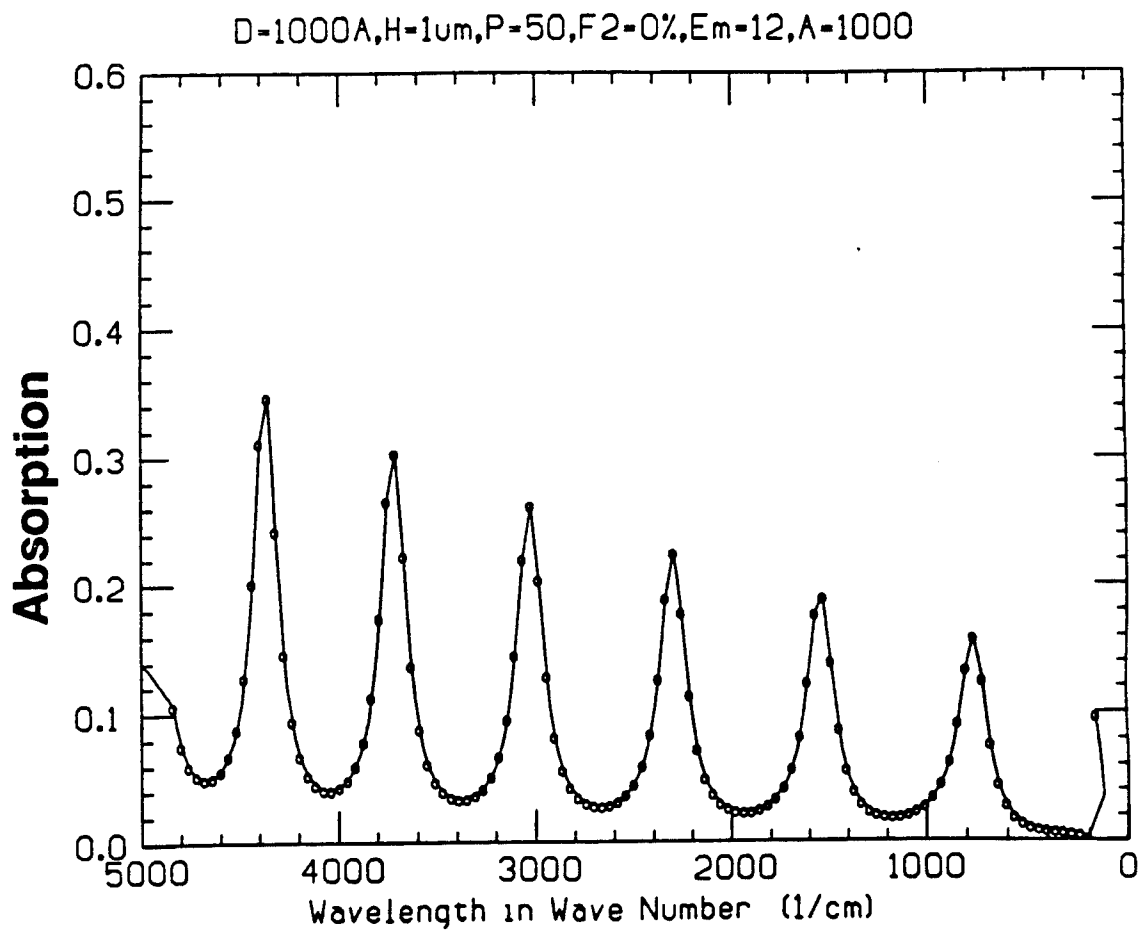


Fig. 6.9.5

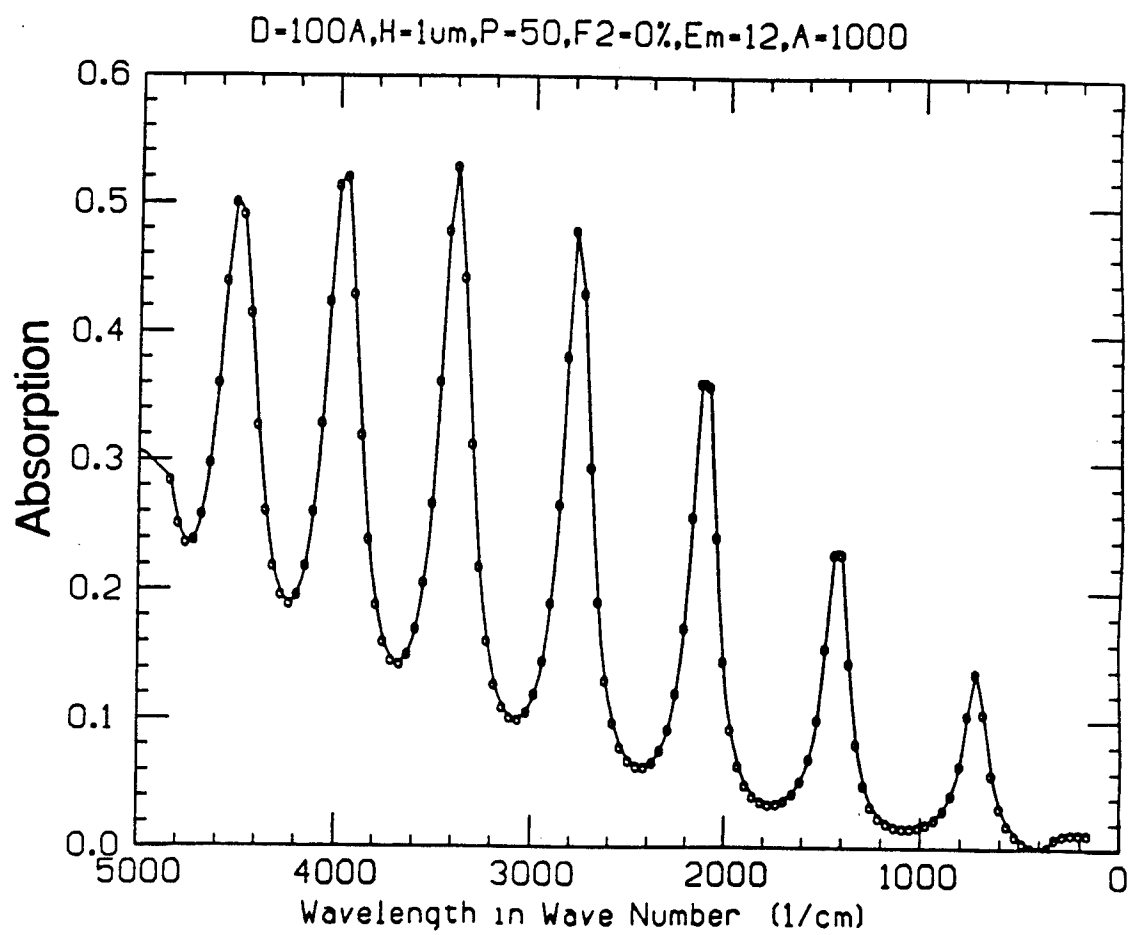


Fig. 6.9.6

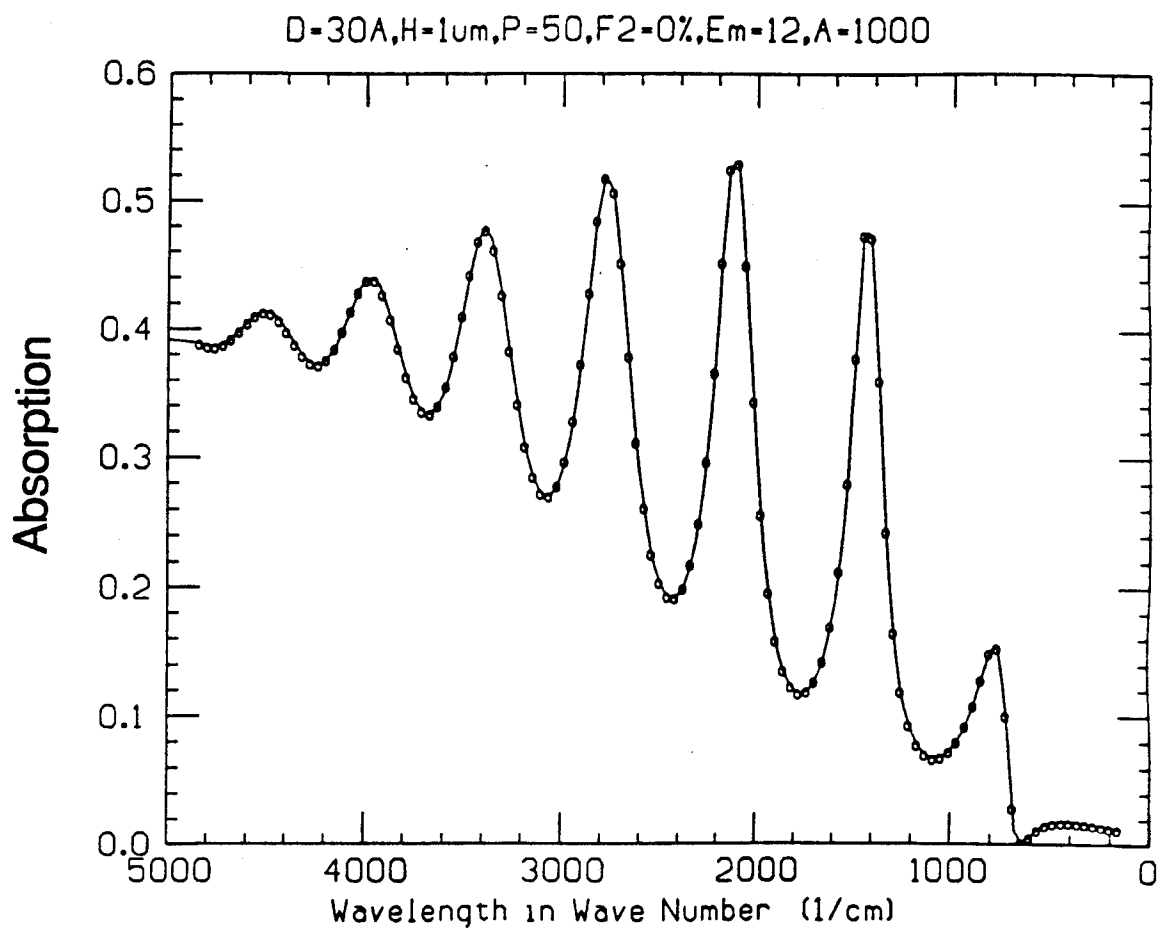


Fig. 6.9.7

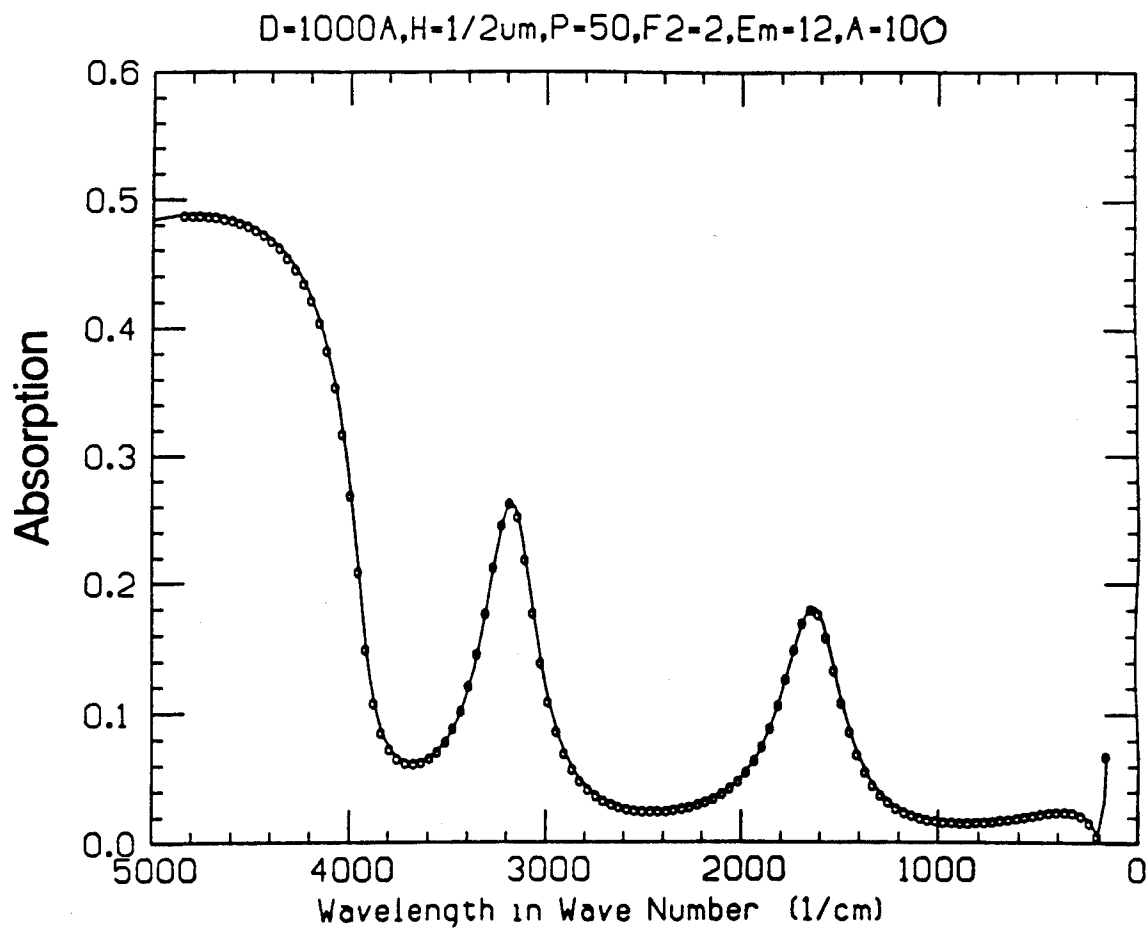


Fig. 6.9.8

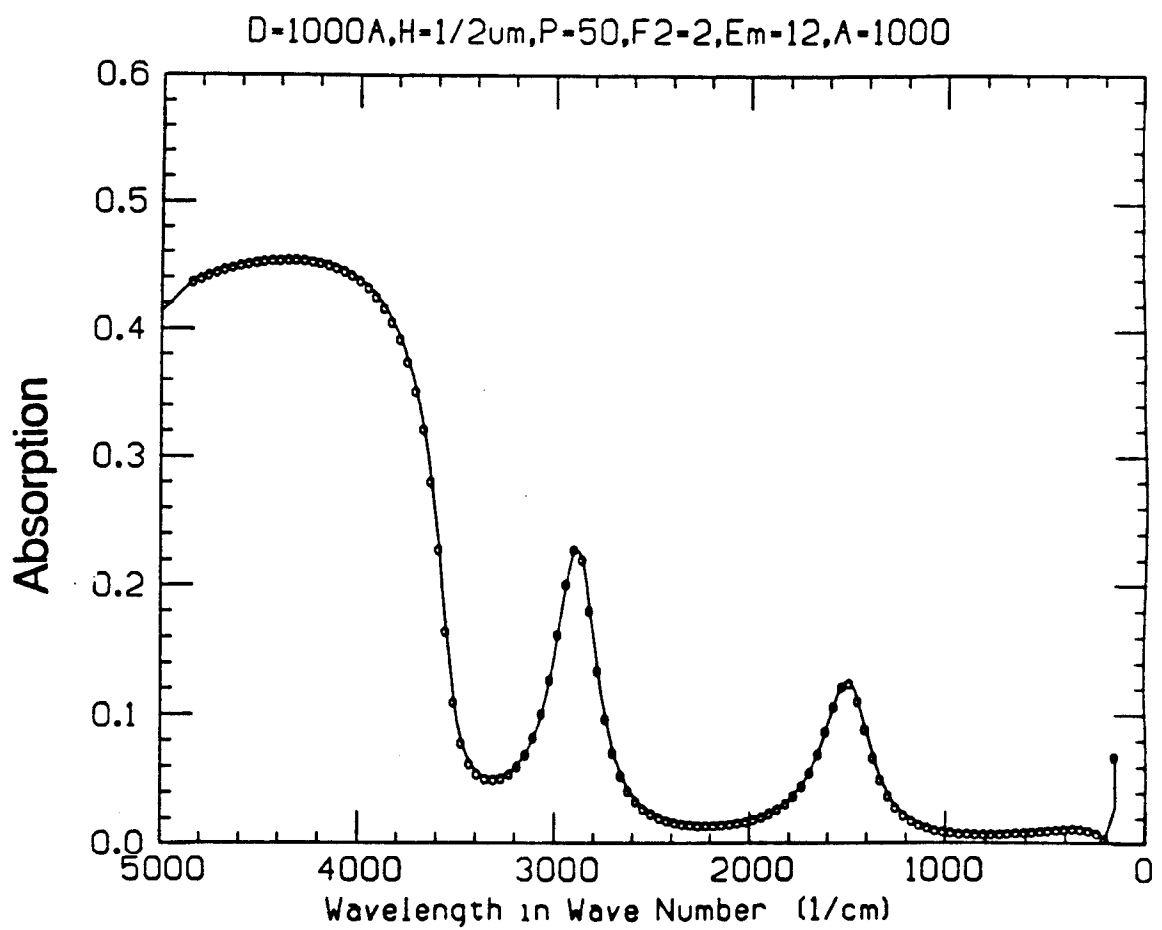


Fig. 6.9.9

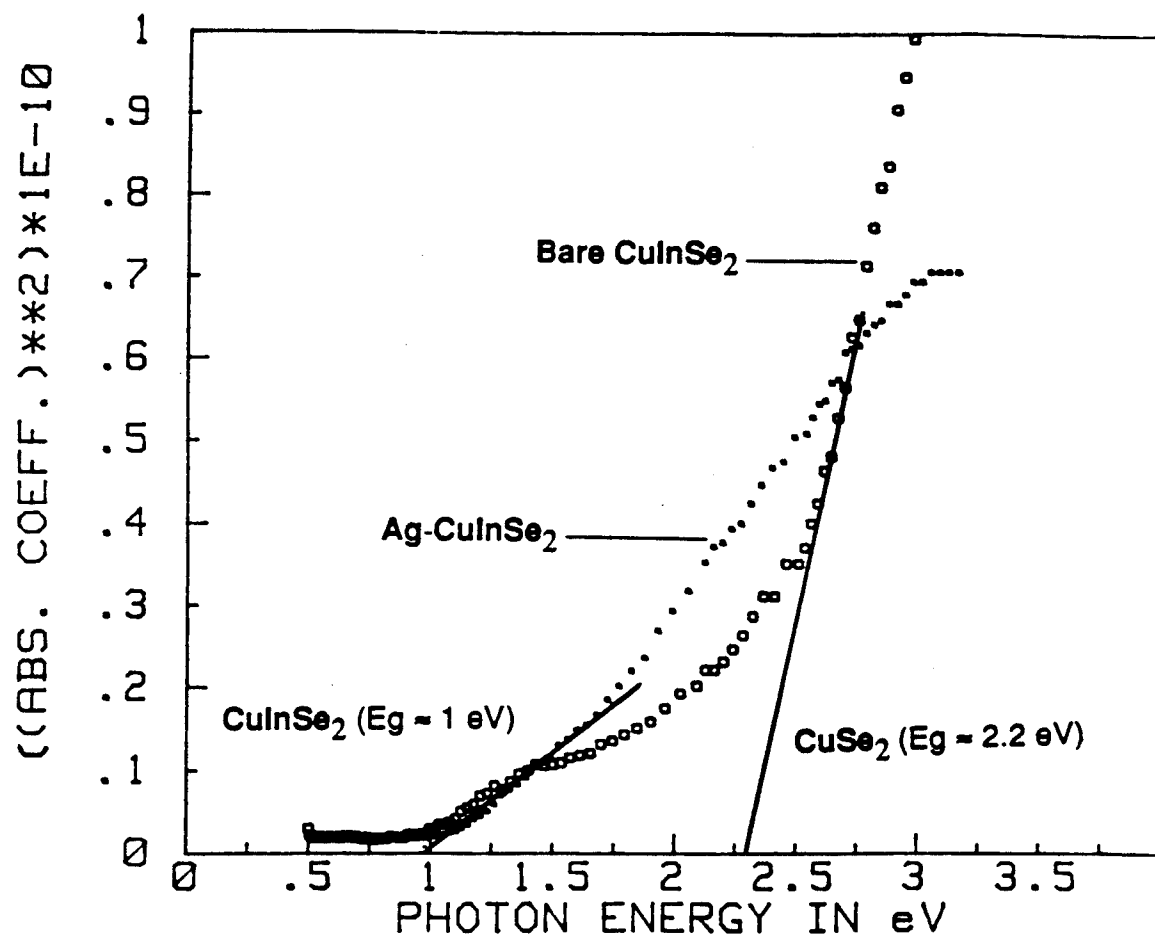


Fig. 6.10 Plot of α^2 v.s $h\nu$ for bare CuInSe₂ (o) and Ag-CuInSe₂ (*).

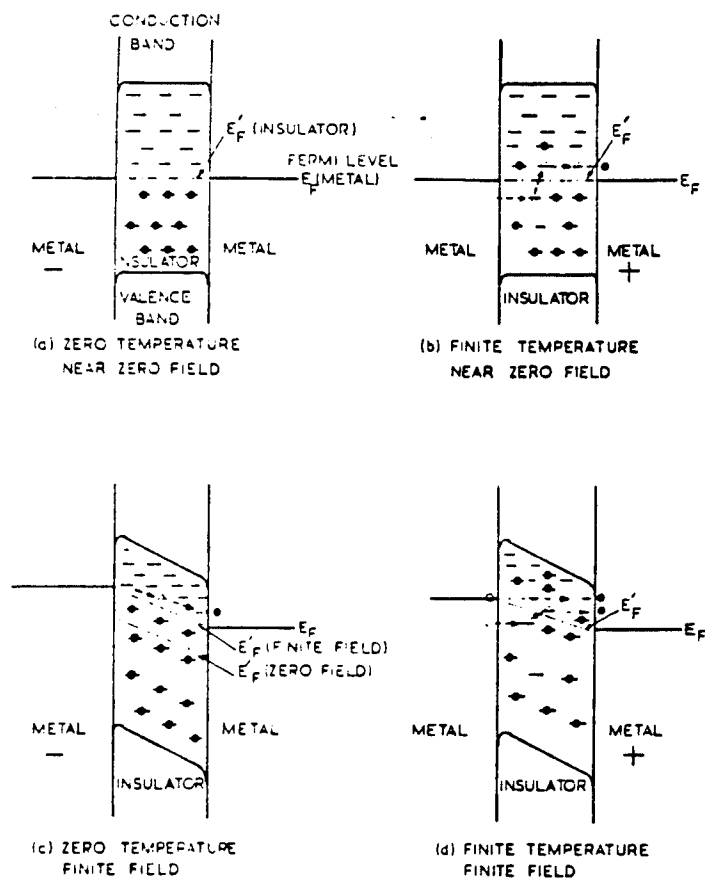


Fig. 6.11 Hopping and tunneling of electrons between particles.
[from 19]

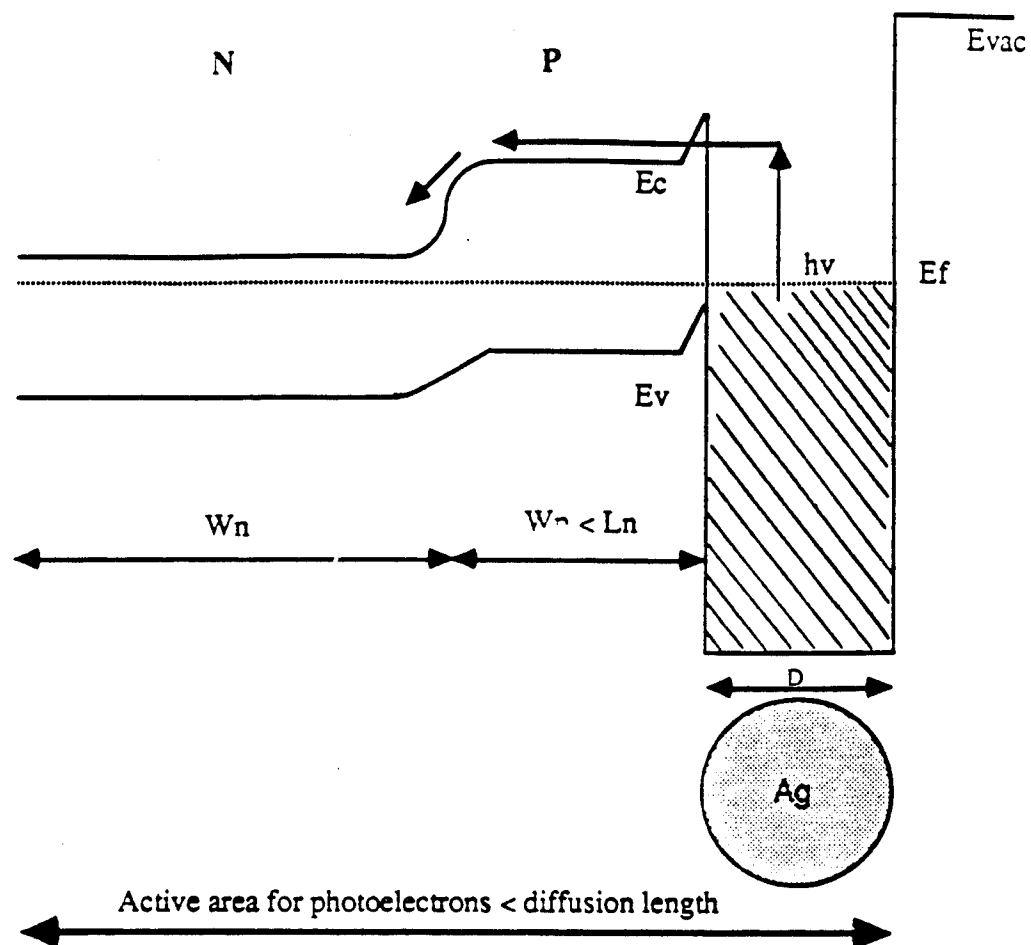


Fig. 6.12 Short-Base Diode with Coverage of Metal particles on the p-side.

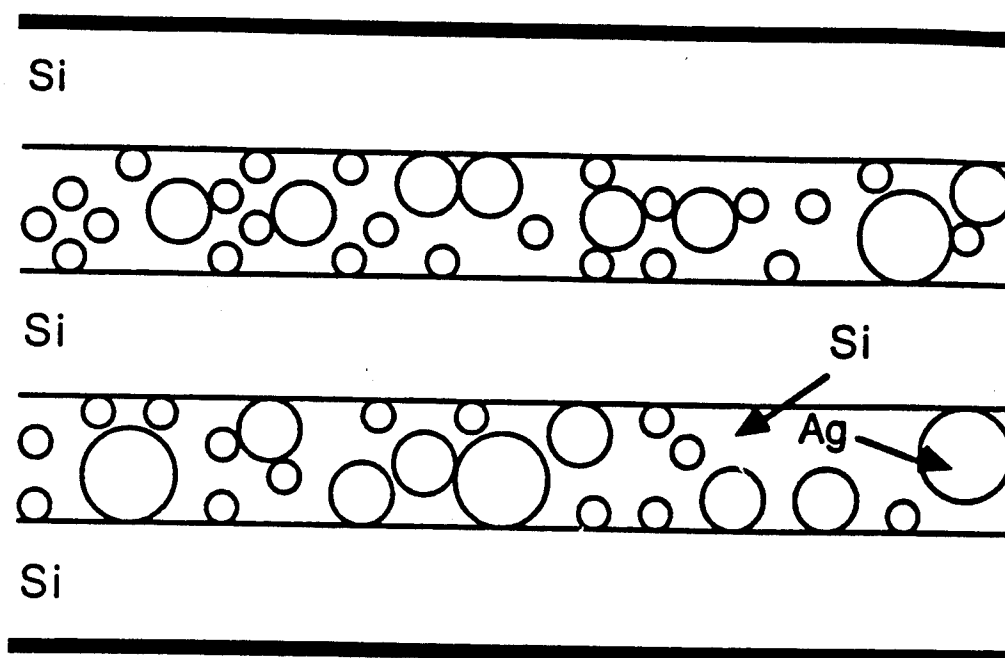


Fig. 6.1 The Ag particles work as electron sources while the Si layers as conduction channel; or the electrons may tunnel through from one particle to another.

MOS DEVICE CHARACTERISTICS

MOS STRUCTURE (NMOS)

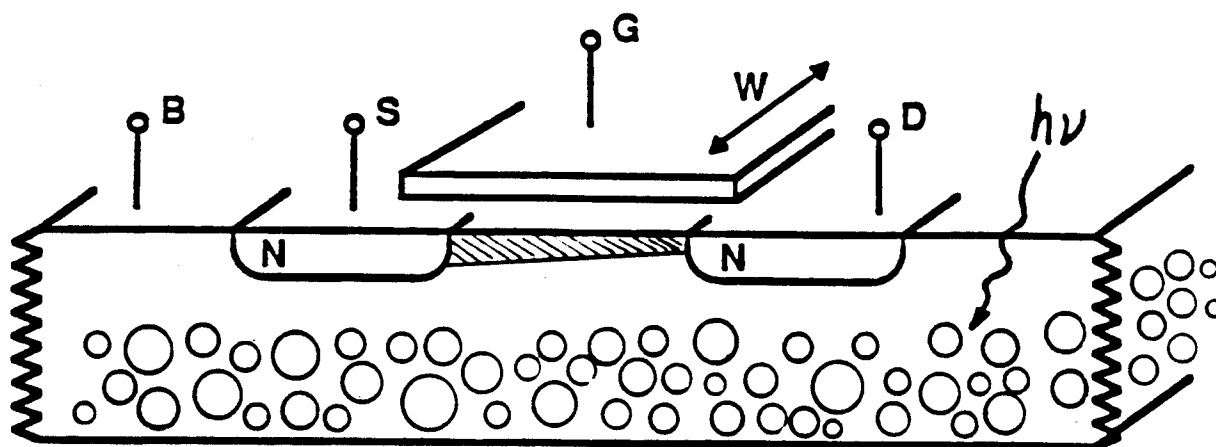
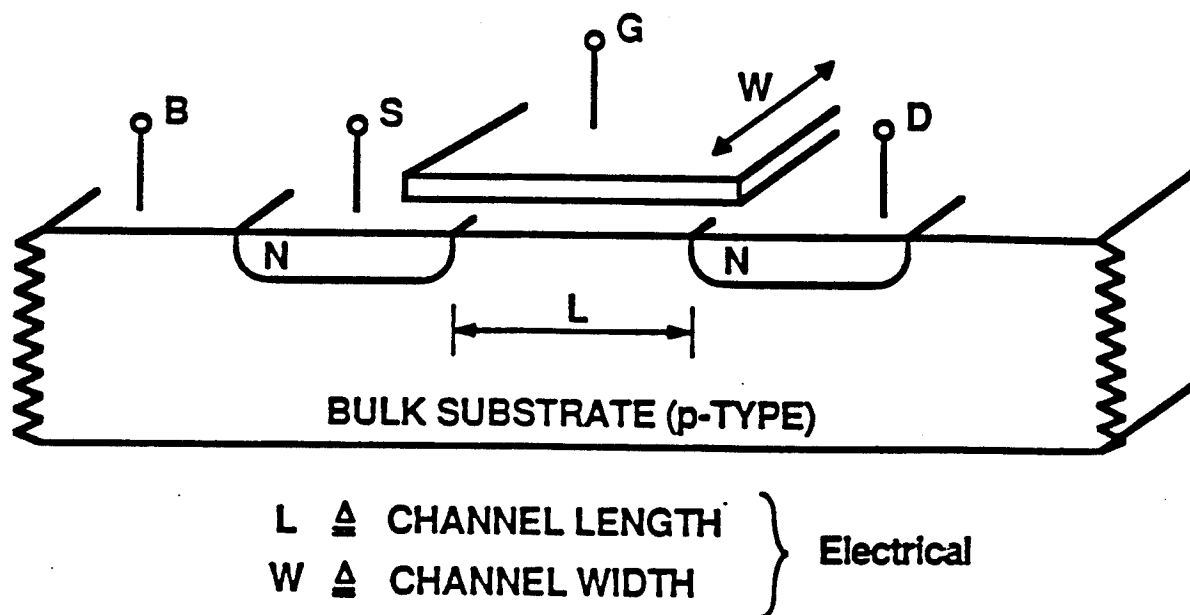


Fig. 6.14 A MOS device with small particles in the p-substrate.

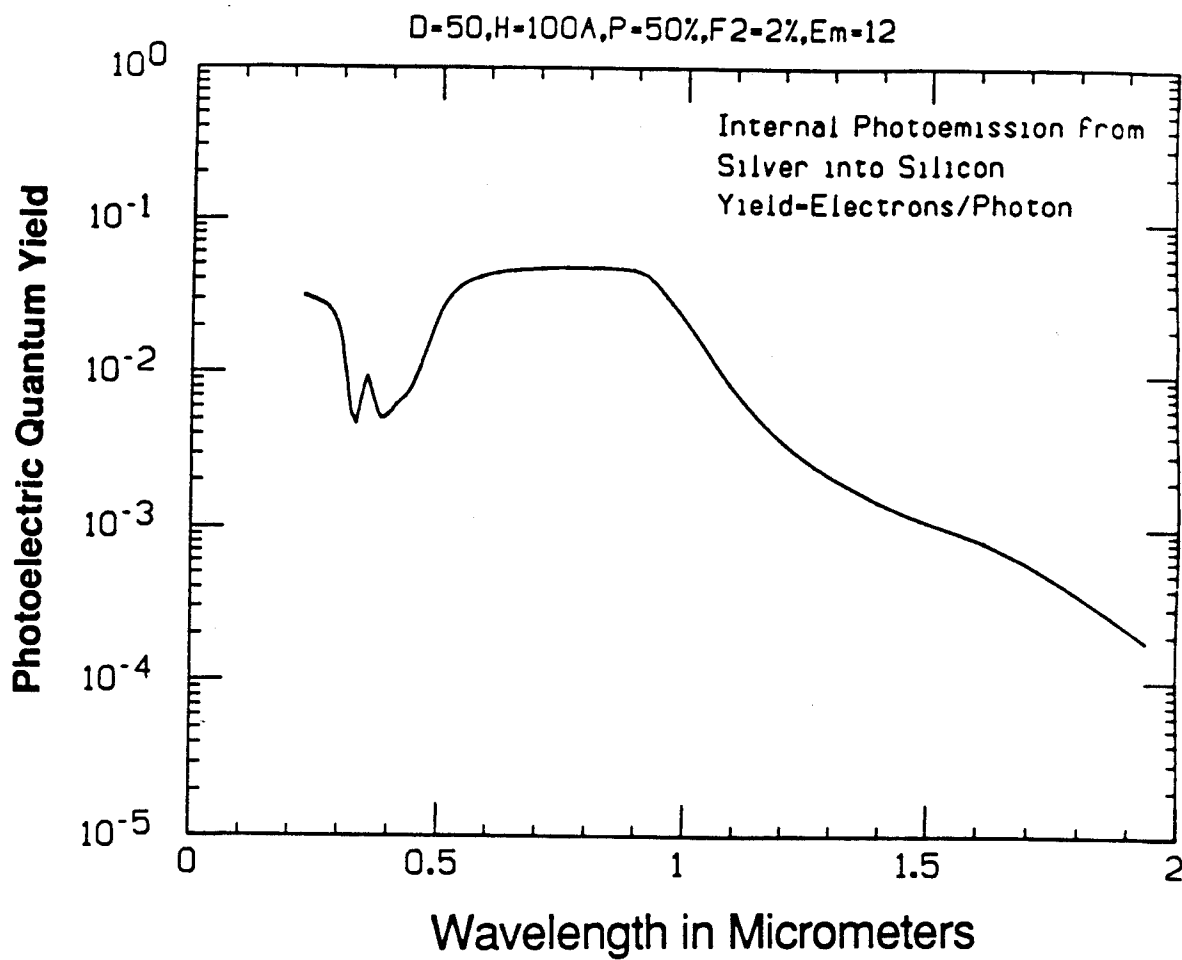


Fig. 6.15 Theoretical quantum yield of Ag particles in silicon matrix with a Schottky barrier height of 0.6eV. Microstructural parameters are as specified.

REFERENCES

Chapter 1

1. Scientific American, p. 97 May, 1986, October issue, 1986 and p. 102 Feb. 1987.
2. L. Chang and B. C. Giessen (ed.) "Synthetic Modulated Structure", Academic Press, 1984.
3. M. J. Kelley and C. Wesbuch (ed.), "The physics and fabrication of microstructures and microdevices", Springer-Verlag, 1986.
4. C. G. Schmahl and D. Rudolph (ed.), "X-ray Microscopy", Springer-Verlag, 1984.
5. N. W. Aschcroft and N. D. Mermin, "Solid State Physics", HRW, 1976.
6. A. H. Sommer, Photoemissive Materials, 1980.
7. A. H. Sommer, Gaede-Langmuir Award Lecture, "The element of luck in research - photocathodes 1930 to 1980", J. Vac. Sci. Technol. A1 (2), 119, (1983).
8. C. W. Bates, Jr. & N. V. Alexander, J. Opt. Soc. Am. A2, (11) 1848 (1985).
9. K. S. Neil and C. H. B. Mee, Phys. Stat. Sol., (a) 2, 43 (1970).
10. C. W. Bates, Jr., Phys. Rev. Lett., 47, 204 (1980).
11. S. J. Yang & C. W. Bates, Jr., Appl. Phys. Lett., 36, 675 (1980).
12. S. J. Yang, Ph.D Dissertation, Stanford University (1978).
13. K. U. von Raben, K. C. Lee, R. K. Chang and R. E. Benner, Jr., J. Appl. Phys., 55, 3907 (1984).
14. P. Sheng, Phy. Rev Lett., 45, 60 (1980).
15. C. F. Bohren and D. R. Huffman, "Absorption and Scattering of Light by Small Particles" (Wiley-Interscience 1983), Chapter 12.
16. G. Ebinghaus, W. Braun and A. Simon, Phys. Rev. Lett., 37 (26), 1770 (1976).

17. P. N. J. Dennis, "Photodetectiors, An introduction to current technology", Plenum Press, 1986.
18. H. N. Norton, "Sensor aand Analyzer Handbook", Prentice Hall, Inc., 1982.
19. G. R. Elion and H. A. Elion, Electro-optics Handbook, Marcel Dekker Inc., NY 1979.
20. M. Y. Schelv, SPIE, Vol. 348, 75 (1982).
21. A. G. Milnes and D. L. Faucht, "Heterojunctions and Metal-Semiconductor junctions", 1976.
22. H. Beneking, IEEE, Trans. Elec. Dev. ED-29, 1431 (1982).
23. W. Roth et al., Electron Letters, 47 (3), 204 (1981).

Chapter 2

1. J. C. Garland and D. B. Tanner (ed.), "Electrical Transport and Optical Properties of Inhomogeneous Media", AIP Conference Proceedings, No.40, 1978, AIP.
2. D. Stroud, Phys. Rev. B, 12, 3368 (1975).
3. D. Stroud and F. P. Pan, Phys. Rev. B, 17 (4), 1602 (1978).
4. P. Chylek and V. Scrivaastava, Phys. Rev. B, 27 (8), 5098 (1983).
5. N. V. Alexander and C. W. Bates, Jr., Solid State Comm., 51, 331 (1984).
6. W. P. Halperin, "Quantum Size Effects in Metal Particles", Review of Modern Physics, 58 (3), 533 (1986).
7. J. A. A. J. Perenboom, P. Wyder and F. Meier, "Electronic Properties of small Metallic Particles", Phys. Rep., 78 (2), 173 (1981).
8. A. E. Hughes and S. C. Jain, Adv. Phys., 28 (6), 717 (1979).
9. N. W. Aschcroft and N. D. Mermin, "Solid State Physics", HRW, 1976.

10. F. Wooten, Optical Properties of Solids, AP, 1972.
11. C. Kittel, Introduction to Solid State Physics, 6th edition, 1986.
12. P. B. Johnson & R. W. Christy, Phys. Rev. B, 6, (12), 4370 (1972) .
13. T. H. Hodgson, Proc. Phy. Soc. 68, 593 (1955).
14. R. G. Newton, Am. J. Phys., 44 (7), 639 (1976).
15. C. F. Bohren and D. R. Huffman, "Absorption and Scattering of Light by Small Particles", John Wiley and Sons, 1983.
16. M. Kerker, "The Scattering of Light", AP, 1969.
17. H. C. van de Hulst, "Light Scattering by Small Particles", Dover, 1981.
18. J. D. Jackson, Classical Electrodynamics", 2nd edition, 1975.
19. J. C. Maxwell-Garnett, Philos. Trans. Roy. Soc. London, 203, 385 (1904) and ibid 205, 237 (1906).
20. D. A. G. Bruggeman, Ann. Phys. (Leipzig) 24, 636 (1935).
21. R. J. Landeauer, J. App. Phys., 23, 779 (1952).
22. D. Stroud, Phys. Rev. B, 19, 1783 (1979).
23. P. Sheng, Phy. Rev Lett., 45, 60 (1980).
24. P. Sheng, "Effective Dielectric Function of Composite Media" in "Lecture Notes in Physics 154-Microscopic Properties of Disordered Media, Springerer-Velag 1982.(ed. J. Ehler et al.)
25. J. I. Gittleman and B. Ables, Phys. Rev. B 15 (6), 3273 (1977).
26. G. B. Smith, J. Physics D, 10, L 39 (1977).
27. S. L. Mcarthy, J. Vac. Sci. Technol., 13, 135 (1976).
28. K. D. Cummings, J. C. Garland and D. B. Tanner, Phys. Rev. B, 30 (8), 4170 (1984).
29. A. H. Sommer, Photoemissive Materials, 1980.

Chapter 3

1. A. Schmidt-Ott, et al. Phys. Rev. Lett., 45 (15), 1284 (1980).
2. A. Schmidt-Ott, et al. App. Phys. Lett., 32(11), 710 (1978).
3. A. Schmidt-Ott, et al. Surface Science, 106, 538 (11981).
4. H. Burtschert, A. Schmidt-Ott and Z. Siegmann, Z. Phys. B, 56, 197 (1984).
5. D. R. Penn & R. W. Rendell, Phys. Rev. Lett., 47(15), 11067 (1981).
6. D. R. Penn & R. W. Rendell, Phys. Rev. B, 26, 3047 (1982).
7. E. Burstein, et al., in "light Scattering in Solids", J. L. Birman, et al. (ed.), Plenum, (1979).
8. H. J. Levinson et. al., Phys. Rev. Lett., 43, 952 (1989).
9. C. W. Bates, Jr., Phys. Rev. Lett., 47, 204 (1981).
10. C. W. Bates, Jr., Appl. Phys. Lett., 45, 1508 (1984).
11. C. W. Bates, Jr., et. al. J. Opt. Soc. Amer., A, 2, 1848 (1985).
12. J. C. Maxwell Garnett, Phil. Trans. A, 203, 385 (1904).
13. C. N. Berglund and W. E. Spicer, Phys. Rev. 136 4A, 1030 (1964).
14. H. Kanter, Phys. Rev. B, 1(2), 522 (1970).
15. P. B. Johnson & R. W. Christy, Phys. Rev. B, 6, (12) 4370 (1972).
16. N. V. Smith, CRC Critical Review in Solid State Sciences, March, (1971).
17. N. H. Frank & L. A. Young, Phys. Rev., 38, 80 (1931).
18. W. A. Harrison, Solid State Theory, Dover, p266, (1980).
19. J. C. Hensel, et al., Phys. Rev. Lett., 54 (16), 1840 (1985).
20. Zlatko Tesanovic, Phys. Rev. Lett., 57 (21), 2760 (1986).

Chapter 4

1. L. R. Koller, J. Opt. Soc. Am., 19, 135 (1929).
2. A. H. Sommer, Photoemissive Materials, (1980).
3. C. W. Bates, Jr. & N. V. Alexander, J. Opt. Soc. Am. A2, (11) 1848 (1985).
4. C. W. Bates, Jr., Phys. Rev. Lett., 47, 204 (1980).
5. S. J. Yang & C. W. Bates, Jr., Appl. Phys. Lett. 36, 675 (1980).
6. S. J. Yang, Ph.D Dissertation, Stanford University (1978).
7. K. U. von Raben, K. C. Lee, R. K. Chang and R. E. Benner, Jr., J. Appl. Phys., 55, 3907 (1984).
8. P. Sheng, Phy. Rev Lett., 45, 60 (1980).
9. C. F. Bohren and D. R. Huffman, "Absorption and Scattering of Light by Small Particles" John Wiley and Sonns, 1983, Chapter 12.
10. G. Ebbinghaus, W. Braun and A. Simon, Phys. Rev. Lett. 37 (26), 1770 (1976).
11. C. W. Bates, Jr. Appl. Phy. Lett. 45, (10) 1058 (1984).
12. Q. D. Wu, Acta Physica Sinica, 28, (4) 553 (1979).
13. Q. D. Wu, Acta Physica Sinica 29, (5) 608 (1979).
14. H. Kanter, Phys. Rev. B1, (2), 522 (1970).
15. N. V. Smith, CRC Critical Review in Solid State Science, March (1971) and its references.
16. N. H. Frank & L. A. Young, Phy. Rev. 38, 80 (1931).
17. C. N. Berglund & W. E. Spicer, Phy. Rev. 136 (4A) A 1030-1064 (1964).
18. W. F. Krolikowski & W. E. Spicer, Phy. Rev. B, 1 (2), 478 (1970).
19. M. Cardona & Ley (ed.), Photoemission in Solids I, Spring Verlag (1978).

20. S. Asao, Proc. Phys. Math. Soc. Japan 22, 448 (1940).
21. O. S. Heavens, Optical Properties of Thin Solid Films, Dover (1965).
22. P. B. Johnson & R. W. Christy, Phys. Rev. B 6, (12) 4370 (1972).
23. T. H. Hodgson, Proc. Phys. Soc. 68, 593 (1955).
24. P. Chylek & V. Srivastava, Phys. Rev. B 27, 5089 (1983).
25. F. Wooten, Optical properties of Solids, A.P. (1972).
26. S. Yamaguchi, et al., Surface Science, 138, 449 (1984).
27. F. S. Crawford, Jr., *Waves*, McGraw Hill, (1968).
28. A. E. Hughes and S. C. Jain, Adv. Phys., 28 (6), 717 (1979).
29. W. Jones & N. H. March, Theoretical Solid State physics, Vol I & II, Dover (1986).
30. S. Ichimaru, Plasma Physics, Benjamin/Cumming, Inc. ^{Menlo Park, CA} (1986).
31. L. C. Chu and S. Y. Wang, J. opt. Soc. Amer. 2 (6), 950 (11985).
32. L. C. Chu and S. Y. Wang, Phys. Rev. B, 31 (2), 695 (11985).
33. A. Wokun and J. P. Gordan and P. F. Liao, Phys. Rev. Lett., 48 (14), 957 (1982).
34. See the review paper by A. E. Hughes and S. C. Jain, Adv. Phys., 28 (6), 717 (1979).
35. D. C. Skillman and C. R. Berry, J. Chem. Phys. 48, 3297 (1968).

Chapter 5

1. C. Kittel, Introduction to Solid State Physics, 6th edition, 1986.
2. B. Ray, II-VI Compounds, pergamon Press, 1969.
3. M. Arnold et al., Cryst. Res. and Technol., 18 (8), 1015 (1983).
4. K. Seaward, Ph.D dissertation, Stanford University, 1984.
5. R. Walmsley, Ph.D dissertation, Stanford University, 1982.
6. J. B. Mooney et al., App. Phys. Lett., 43(9), 851 (1983).

7. S. L. McCarthy, J. Vac. Sci. and Technol., 13 (1), 135 (1976).
8. J. W. Martin and R. D. Doherty, "Stability of Microstructure in Metallic Systems", Cambridge Solid State Science Series, Cambridge University Press, 1976.

Chapter 6

1. F. Grum and G. W. Luckey, App. Opt., 7 (11), 2289 (1968).
2. W. E. K. Middleton and C. L. Sanders, Illuminating Engineering, 40 (5), (1953).
3. A. Walsh, J. Opt. Soc. Am., 43 (1), (1953).
4. W. E. K. Middleton and C. L. Sanders, J. Opt. Soc. Am., 41 (6), (1951).
5. T. C. Paulick, "Inversion of normal incidence (R,T) measurements to obtain $n+ik$ for thin films", App. Opt., 25 (4), (1986) and references therein.
6. K. Palmer and M. Z. Williams, App. Opt., 24 (12), 1778 (1985).
7. I. A. Tekucheva, Izvestiya UVZ, Fizika, No. 1, p. 116 (1985).
8. F. Abeles, Progress in Optics, Vol. II, p.251 (1963).
9. S. G. Tomlin, J. Phys. D, ser. 2, Vol. 1, 1667 (1968).
10. L. Ward, J. Phys. D, 18, 291 (1985).
11. M. Chang and U. J. Gibbson, App. Opt., 24 (4), 504 (1985).
12. B. Bovard et al., App. Opt., 24 (12), 1803 (1985).
13. J. Mouchart et al., App. Opt., 24 (12), 1809 (1985).
14. R. Swanepoll, J. Opt. Soc. Am. A , 1339 (1985).
15. M. Born and E. Wolf, Principles of Optics, 6th Ed., Pergaman Press, 1980.
16. O. S. Heavens, Optical Properties of Thin Solid Films, Dover (1965).
17. S. L. McCarthy, J. Vac. Sci. and Technol., 13 (1), 135 (1976).

18. B Abeles, Ping Sheng, M. D. Coutts and Y. Arie, Adv. Phys. 24 (3), 407 (1975).
19. T. J. Coutts, "Electrical Conduction in Thin Metal Films", Elsevier Scientific, 1974.
20. Q. D. Wu and Xi-Qing Liu, J. Vac. Sci. Technol., A1(2), 71 (1983).
21. G. A. Niklasson and C. G. Grangvist, Phys. Rev. Lett., 56 (3), 256 (1986).
22. J. V. Mantese and W. A. Curtin, Phys. Rev. B, 33 (22) part I, 7897 (1986).
23. P. M. Hui and D. Stroud, Phys. Rev. B, 32 (12), 7728 (1985).
24. B. N. J. Persson and J. E. Demuth, Phys. Rev. B, 31 (4), 1856 (1985).
25. J. D. Benjamin, et al., J. Phys. C. 17, 559 (1984).
26. M. S. Raven, Phys. Rev. B, 29(11), 6218 (1984).
27. M. Nakamura, Phys. Rev. B, 29 (6), 3691 (1984).
28. J. D. Joannopoulos and G. Lucovsky, The Physics of Hydrogenated Amorphous Silicon, I, Springer-Verlag, 1984.
29. M. Sze, Physics of Semiconductor Devices, 2nd ed., 1981.
30. S. Iijima and T. Ichihashi, Phys. Rev. Lett., 56 (6), 616 (1986).
31. S. Iijima and T. Ichihashi, Japn. J. App. Phys., 24 (2), L125 (11985).
32. T. Yasuda et al., App. Phys. Lett., 49 (14), 903 (1986).